

JOURNAL OF SCIENCE & ENGINEERING

HITTITE



HJSE - Official Journal of Hitit University - Volume 4, Issue 1, 2017 - www.hjse.hitit.edu.tr

Volume 4, Issue 1, 2017

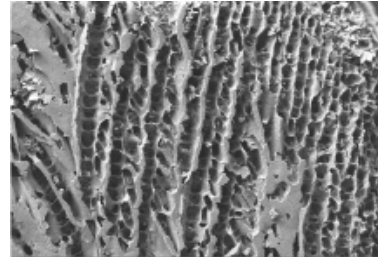
www.hjse.hitit.edu.tr

Lead Removal from Industrial Waste

01-05

Elif Bilgin, Murat Yüce, Kazım Köse, Kadir Erol, Dursun Ali Köse

In this study, the heavy metal removal performance of poly(2-hydroxyethyl methacrylate-N-methacryloyl-(L)-histidine methyl ester), poly(HEMA-MAH) cryogel, a known polymer, in HNO₃ was investigated. To determine the heavy metal removal performance of cryogel, wastewater was used as obtained from an inorganic material manufacturer.

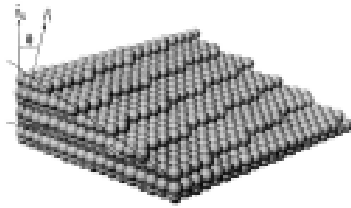


Thermal Grooving by Surface Diffusion: a Review of Classical Thermo-Kinetics Approach

07-16

Oncu Akyildiz, and Tarik Omer Ogurtani

In polycrystalline materials wherever a grain boundary intersects a free surface and whenever the topographic variation associated with the atomic motion is favored by total free energy dissipation, the material surface grooves.

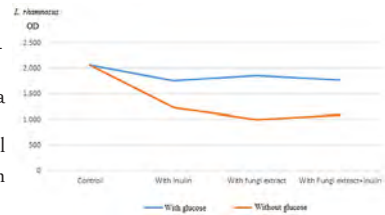


Effect of Inulin and Auricularia polytricha Extract on Proliferation of Lactobacillus rhamnosus

17-21

Gülçin Alp Avcı, Burçin Özçelik and Ceren Kesepara

Probiotic microorganisms have many health-beneficial effects on gastrointestinal system and their therapeutic usage is becoming increasingly common in human and veterinary medicine.

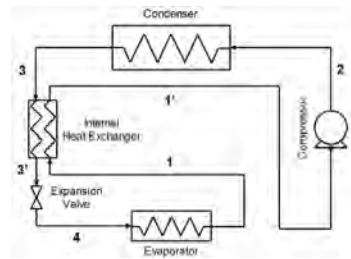


Theoretical Performance Analysis of an R1234yf Refrigeration Cycle Based on the Effectiveness of Internal Heat Exchanger

23-30

Mehmet Direk, Alper Keleşoğlu, Ahmet Akın

In this paper, the effects of internal heat exchanger (IHX) effectiveness on the performance parameters of the refrigeration cycle with R1234yf were theoretically investigated. For this purpose, a mathematical model was developed based on the energy balance of the cycle.

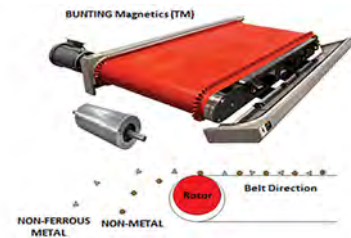


Design and Analysis of In-Drum Outer Rotor BLDC Motor for Eddy Current Separator

31-37

Ahmet Fenercioglu and Merve Sen Kurt

In this study, a novel In-Drum Brushless Direct Current (ID-BLDC) motor is proposed to Eddy Current Separator (ECS) which separates nonferrous metals from waste. The ECS's separation efficiency depends on magnetic drum speed.



Seasonal and Spatial Variation of Epilithic Algal Community in Batlama Stream (Giresun, Turkey)

39-44

Faruk Maraşlıoğlu, Elif Neyran Soylu, Sibel Altürk Karaca

Spatio-temporal changes in taxonomic composition and structure of epilithic algal community with some physicochemical features of the Batlama stream were assessed between June 2013 and May 2014 at the intertidal zone of the Batlama Stream, Giresun, Turkey.

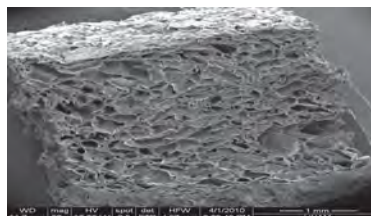


Evaluation of Chitosan /Organoclay Composite as Bone Tissue Engineering Scaffold

45-49

Aysel Koç Demir

In this study, a scaffold composed of chitosan (C) and organoclay (OC) was prepared by utilizing freeze-drying method. The composition of resulting composite scaffold was evaluated using FTIR and SEM.

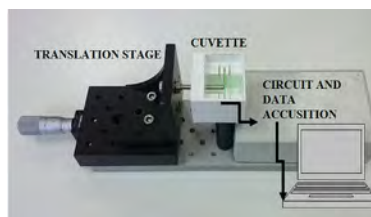


Quantized Conductance Measurement System for Liquids and Application to DNA Solution

51-55

Yavuz Öztürk, Büşra Yıldırım, Koray Şekerin and Alper Bayram

In this study, a system for undergraduate and graduate laboratories was designed in order to investigate quantized conductivity behavior of solutions. The quantized conductivity of the DNA solution was examined by using the designed system.

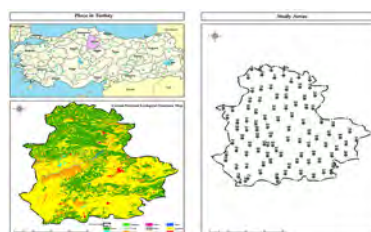


Contributions to the Knowledge of Mammals in Çorum Province, Turkey

57-63

Şafak Bulut, Burak Akbaba and Ahmet Karataş

A total of 42 mammal species were determined and new records reported for the first time in Çorum Province, Turkey. Field studies were carried between 2009-2010 and 2015-2016.

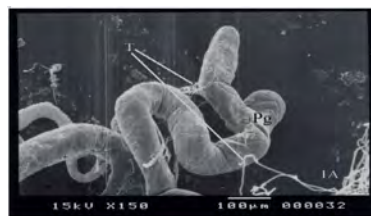


Investigation of Poison Gland of Sphex flavipennis Fabricius, 1793 (Hymenoptera: Sphecidae): Morphology and Ultrastructure

65-69

Menderes Suiçmez, Mustafa Duran and Kasım Özmen

The structure of poison gland of *Sphex flavipennis* was investigated by using scanning electron microscopy and transmission electron microscopy. Poison apparatus consists of poison gland, poison sac, Dufour's gland and poison needle.

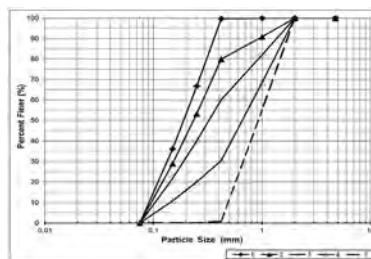


Permeability Characteristics of Sand Grouted with Glyoxal Blended Sodium Silicate

71-78

Eyubhan Avcı

The goal of this study was to investigate the permeability characteristics of glyoxal blended sodium silicate injected sand specimens with different relative densities and gradations. Initially, rheological characteristics of glyoxal blended sodium silicate grouts were determined.

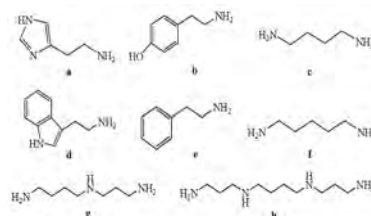


Optimization of the Schiff-Base Reaction of Acetylacetone with Biogenic Amines

79-83

Bediha Akmeşe and Adem Asan

In this work, optimum conditions for the derivatization reaction of biogenic amines (histamine, tyramine, putrescine, tryptamine, phenylethylamine, cadaverine, spermidine and spermine) with acetylacetone have been determined.



Owner

Prof. Dr. Reha Metin ALKAN
on behalf of Hitit University

Editor-in-chief

Prof. Dr. Ali Kılıçarslan

Associate Editors

Assoc. Prof. Dr. D. Ali Köse
Asst. Prof. Dr. Öncü Akyıldız

Production

Dr. Kazım Köse
Mustafa Güzel
Mustafa Reşit Haboğlu

Proofreading

Dr. Aytekin Uzunoglu

Editor's Office

Tel: +90 364 227 45 33 / 12 36

Fax: +90 364 227 45 35

Email: alikilicarslan@hitit.edu.tr

Subscription Service:

Tel: +90 364 227 45 33 / 12 82

Fax: +90 364 227 45 35

Email: hjse@hitit.edu.tr

EDITORIAL BOARD

- Prof. Dr. İftikhar AHMAD, University of Malakand, Chakdara, Pakistan
 Assoc. Prof. Dr. Abdurrahman ASAN, Hitit University, Turkey
 Prof. Dr. Yusuf AYVAZ, Suleyman Demirel University, Turkey
 Assoc. Prof. Dr. Kazım Savaş BAHÇECİ, Hitit University, Turkey
 Prof. Dr. Satılmış BASAN, Hitit University, Turkey
 Prof. Dr. Mike BECKETT, Bangor University, Bangor, United Kingdom
 Assoc. Prof. Dr. Naki ÇOLAK, Hitit University, Turkey
 Assoc. Prof. Dr. Elif DALYAN, Hitit University, Turkey
 Prof. Dr. Vedat DENİZ, Hitit University, Turkey
 Prof. Dr. Adil DENİZLİ, Hacettepe University, Turkey
 Prof. Dr. İbrahim DİNÇER, Uoit Ontario University, Ontario, Canada
 Prof. Dr. Ali ELKAMEL, University of Waterloo, Ontario, Canada
 Prof. Dr. Ali GENCER, Ankara University, Turkey
 Prof. Dr. Faruk GÖKMEŞE, Hitit University, Turkey
 Assoc. Prof. Dr. Hakan GÜNGÜNEŞ, Hitit University, Turkey
 Prof. Dr. Metin GÜRÜ, Gazi University, Turkey
 Prof. Dr. Murat HOŞÖZ, Kocaeli University, Turkey
 Assoc. Prof. Dr. Bülent KABAK, Hitit University, Turkey
 Prof. Dr. Sadık KAKAÇ, TOBB University, Turkey
 Prof. Dr. Ali KILIÇARSLAN, Hitit University, Turkey
 Assoc. Prof. Dr. Dursun Ali KÖSE, Hitit University, Turkey
 Assoc. Prof. Dr. İrfan KURTBAŞ, Hitit University, Turkey
 Dr. Wojciech NOGALA, Polish Academy of Sciences, Poland
 Prof. Dr. Tarık Ömer OĞURTANI, Middle East Technical University, Turkey
 Prof. Dr. Aydın ÖZLÜK, Hitit University, Turkey
 Prof. Dr. Mohamad S QATU, Central Michigan University, Michigan, United States
 Prof. Dr. Saffa RIFFAT, The University of Nottingham, United Kingdom
 Prof. Dr. Thanos SALIFOGLU, Aristotle University of Thessaloniki, Thessaloniki, Greece
 Prof. Dr. Seçil SATIR, Hitit University, Turkey
 Prof. Dr. Uğur Adnan SEVİL, Hitit University, Turkey
 Assoc. Prof. Dr. Fatma Muazzez ŞİMŞİR, Hitit University, Turkey
 Prof. Dr. İbrahim SÖNMEZ, Hitit University, Turkey
 Assoc. Prof. Dr. Yuehong SU, The University of Nottingham, United Kingdom
 Prof. Dr. Menderes SUİÇMEZ, Hitit University, Turkey
 Prof. Dr. Ender SUVACI, Anadolu University, Turkey
 Assoc. Prof. Dr. Ali TOPÇU, Hacettepe University, Turkey
 Assoc. Prof. Dr. Dilber Esra YILDIZ, Hitit University, Turkey

Journal Name	: HITTITE JOURNAL OF SCIENCE AND ENGINEERING
Year	: 2017
Managing Editor	: Prof. Dr. Ali KILIÇARSLAN
Managing Office	: Hitit University Faculty of Engineering
Managing Office Tel	: +90 364 227 45 33 / 12 36
Publication Language	: English
Publication Type	: Peer Reviewed, Open Access, International Journal
Delivery Format	: 2 times a year (semi-annually)
Print ISSN	: 2149-2123
Publisher	: Bir Medya
Publisher Address	: Yenyol Mah. Gazi 12. Sok. No:9/13 ÇORUM
Publisher Tel	: +90 364 225 66 64



This new issue of Hittite Journal of Science and Engineering (HJSE) contains twelve manuscripts within different aspects of the science and engineering. First, I would like to express my gratitude to all our authors and contributing reviewers of this issue. A good follower must have realized the increase in the number of articles in this issue. We are also planning to increase the number of issues that is going to be published during a year in the coming years.

*It is my pleasure to inform all our readers that the 21th National Congress on Thermal Science and Technology (21. Ulusal Isı Bilimi ve Tekniği Kongresi; ULIBTK'17) will be hosted by the Hitit University in our city of Çorum in between 13 – 16th of September. I am excited to announce our confirmed invited speakers: **Professor Sadık Kakaç** of TOBB University of Economics and Technology, Ankara/TURKEY; **Professor Leonard L. Vasiliev** from Minsk/BELARUS, the Chief researcher of the Luikov Heat and Mass Transfer Institute; **Professor Bengt Sunden** from Lund/SWEDEN, the Head of the Department of Energy Sciences of Lund University; **Professor Boris V. Kosoy** from Odessa, UKRAINE, the Director of the Institute of Refrigeration, Cryotechnology and Ecoenergetics of Odessa National Academy of Food Technologies; **Professor Bakhtier Farouk** from Philadelphia/USA, the J. Harland Billings Professor of Mechanical Engineering and Mechanics of Drexel University. We believe that the ULIBTK'17 will be an exciting and meaningful event, bringing together scientists from all over the world and providing new ideas for future studies. Selected papers from the congress will be published in a special issue of HJSE after peer review.*

I would like to thank to the President of Hitit University, Prof. Dr. Reha Metin Alkan, for his constant interest in HJSE and also to the Associate Editors of HJSE, namely Dr. Dursun Ali Kose and Dr. Oncu Akyildiz. Special thanks is due to our Production Team, Dr. Kazim Kose, Mustafa Guzel, Mustafa Resit Haboglu and to our Proofreader Dr. Aytekin Uzunoglu. I also would like to thank to the Editorial Board from national and international universities.

It's my pleasure to invite the researchers and scientists from all branches of science and engineering to join us by sending their best papers for publication in Hittite Journal of Science and Engineering.

Dr. Ali Kiliçarslan

Editor-in-Chief

Lead Removal from Industrial Waste

Elif Bilgin¹, Murat Yüce², Kazım Köse^{3,*}, Kadir Erol⁴, Dursun Ali Köse⁵

¹Hitit University, Institute of Science and Technology, Çorum, TURKEY

²Hitit University, Department of Chemistry, Çorum, TURKEY

³Hitit University, Scientific Technical Research and Application Center, Çorum, TURKEY

⁴Hitit University, Department of Property Protection and Safety, Çorum, TURKEY

ABSTRACT

In this study, the heavy metal removal performance of poly(2-hydroxyethyl methacrylate-N-methacryloyl-(L)-histidine methyl ester), poly(HEMA-MAH) cryogel, a known polymer, in HNO₃ was investigated. To determine the heavy metal removal performance of cryogel, wastewater was used as obtained from an inorganic material manufacturer. The characterization studies using scanning electron microscopy (SEM), Fourier transform infrared (FT-IR) spectroscopy, elemental analysis, water-swelling tests and surface area analysis were conducted. The effect of HNO₃ on the adsorption process, especially for metals, was found very effective even in trace amounts.

Article History:

Received: 2016/08/11

Accepted: 2016/10/04

Online: 2017/30/06

Correspondence to: Kazım Köse, Hitit University, Scientific Technical Research and Application Center, Çorum, TURKEY
Tel: +90 (364) 219 2850/2866
Fax: +90 (364) 219 2855
E-Mail: kazimkose@hitit.edu.tr

Keywords:

Cryogel; Heavy metal removal; Wastewater.

INTRODUCTION

The increasing number of factories with the heavy metal wastes, especially lead, such as a battery, dye, and fertilizer manufacturing, etc. [1], in consequence of the fast developments of agricultural and industrial fields, threaten the ecological environment and human health. The heavy metal ions cannot be degraded, and resulted in an accumulation in the living organism tissues [2]. The lead limits in drinking water allowed by the World Health Organization is 10 µg/L [3]. Moreover, even very little concentration of lead can cause severe consequences for living things including humans [4]. Because its high affinity to enzymes having thiol (-SH) and phosphate ions (PO₄³⁻), ligands and biomolecules inhibiting the haem biosynthesis, Pb²⁺ ions are very hazardous for the permeability of cell membranes in kidney, liver, and brain and likewise toxic for nervous and reproduction system, resulting in abortion, dead and neonatal birth, mental retardation [5, 6], etc. Additionally, it may form complexes with the oxo-groups of enzymes which are very active in porphyrin metabolism and haemoglobin synthesis [7]. Besides the potential neurological and carcinogenic effects of lead, it may cause cognitive and physical retardation in child development, especially in the interval of 0-7 age [8]. Lead has been classified as a carcinogenic

element by the US Environmental Protection Agency and International Agency for Research on Cancer [9].

To date, many of methods were reported on the removal of heavy metal from aqueous solutions such as flocculation, coagulation, electrochemical treatment, and solvent extraction etc. [10-12]. Most of these methods are insufficient and not cost-friendly for controlling heavy metal levels in wastewater, and also for effectivity and environmental care [7]. The affinity adsorption method is the most promising method for the heavy metal removal process [13]. The adsorption technique is simple, cost-friendly and non-toxic [14-17]. Thereupon, useful and easy-to-prepare adsorbents are needed to developed for the heavy metal removal [18] such as iron oxide [19, 20], activated carbon [21], kaolinite [22] and zeolite [23]. On the contrary, these materials have some drawbacks such as aggregation, low adsorption capacity and poor mechanical strength resulting in low yields [24].

In this study, we developed polymeric cryogels, poly(2-hydroxyethylmethacrylate-N-methacryloyl-(L)-histidine methyl ester), poly(HEMA-MAH), for the removal of lead ions from aqueous solution and wastewater obtained from an inorganic material

manufacturer. The aim of the synthesis of this polymeric material was to develop an alternative to conventional methods for heavy metal removal. The application of cryogels is very simple compared to other adsorbents, and thus it may be a good contribution to the literature for the removal of heavy metals.

MATERIALS and METHODS

2-Hydroxyethyl methacrylate (HEMA), ethylene glycol dimethacrylate (EGDMA), lead(II) nitrate, ammonium persulphate, (APS), sodium dodecyl sulphate (SDS), N,N,N',N'-tetramethyl ethylene diamine (TEMED) were purchased from Sigma (St. Louis, USA). N-methacryloyl-(l)-histidine (MAH) was synthesized in accordance with the literature [25]. All other chemicals were in analytical grade and ultra-pure water was used in all experiments.

Synthesis and characterization of poly(2-hydroxyethylmethacrylate-N-methacryloyl-(L)-histidinemethylester cryogels

For the synthesis of poly(HEMA-MAH) cryogels, MAH (200 mg) and HEMA (5 mL) were used as the functional monomer and solid support, respectively. HEMA and MAH were mixed with distilled water of 5 mL before adding to the dispersant phase comprising SDS (1 g), EGDMA (1.2 mL) and distilled water of 18.8 mL. The solution obtained was stirred in a magnetic stirrer for 5 minutes and remained in an ice-bath for 15 minutes before the addition of APS (30 mg) and TEMED (150 µL). The resulting gel was poured into the two glass plates and remained at -20°C for 24 hours for the cryogelation. A day later, the polymeric cryogel plate was taken, and cut in the shape of a circular disk and washed with distilled water to get rid of unwanted chemicals and foam.

The achievement on the structure of cryogels was tested via FT-IR (Thermo Scientific Nicolet 6700 FT-IR spectrometer, Waltham, USA) (Figure 1). The stretching (at

3390.05 and 1713.53 cm⁻¹) and amide (at 1650.32 and 1540.38 cm⁻¹) bands were the proof of the MAH incorporation (195 µmole/g polymer, via Elemental analysis (Elementar Vario PYRO cube, Hanau, Germany) into the structure. Because of cryogelic polymerization, there were big cavities formed as a result of water removal at the end of the polymerization. The cavities with rough surface (approximately 3.343 m²/g, via Quantachrome AutosorbVr iQ-Chemi, Florida, USA, which was comparable with the literature [26-28]) suitable for the adsorption of lead ions could be seen in SEM (Carl Zeiss AG—EVO® 50 Series, Germany) images given in Figure 2. The water uptake amount of cryogels was found (376% on average) using the difference between the weights of dry and water retained cryogel according to the formula given by Equation 1. This means that approximately 376 times cryogel mass diffuse into the cryogels with target molecules inside, resulting the long-time interaction, providing high yields in spite of low surface area.

$$\text{Water uptake \%} = \left[\frac{(W_{\text{swollen}} - W_{\text{dry}})}{W_{\text{dry}}} \right] \times 100 \quad (1)$$

Where W_{swollen} is the weight (g) of swollen after removal from the water bath and W_{dry} is the dry weight before entering the water bath.

The Adsorption-Desorption Experiments

The nitric acid solution (5%, v/v) was used as a solvent for the lead removal from aqueous solution. All experiments were performed via a rotator at the speed of 20 rpm for 15 minutes batch wise. The lead adsorption capacities of cryogels were estimated using the formula given by Equation 2.

$$q = \frac{(C_i - C_f) \times V}{m} \quad (2)$$

Where, q , C_i , C_f , V and m are adsorption capacity (mg/g), initial concentration (mg/L), final concentration (mg/L), the volume of the adsorption medium (mL) and amount of cryogel (g), respectively.

The atomic absorption spectrophotometry (Thermo

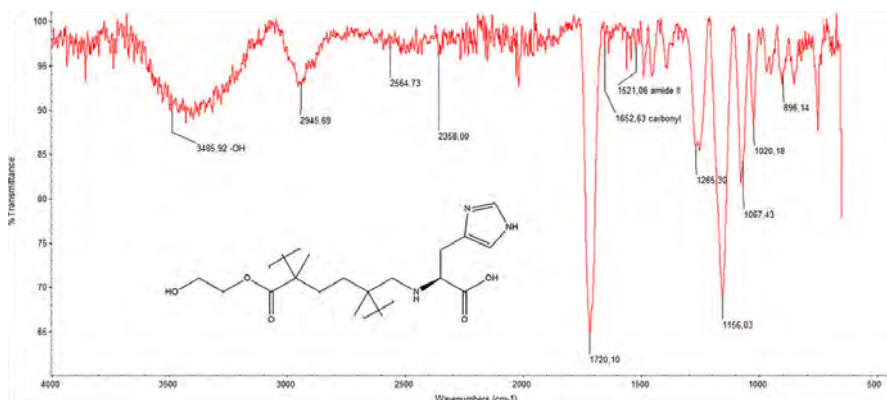


Figure 1. FT-IR spectra of poly(HEMA-MAH) cryogels.

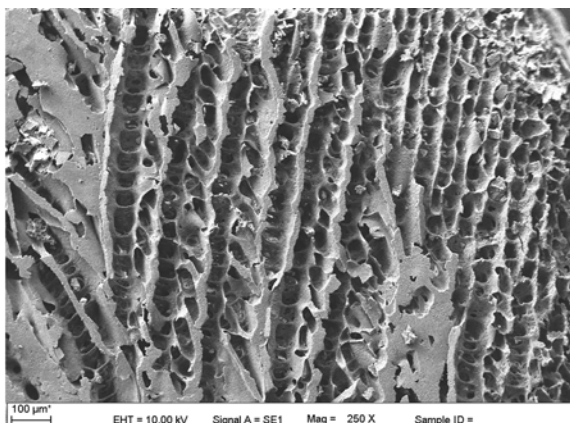
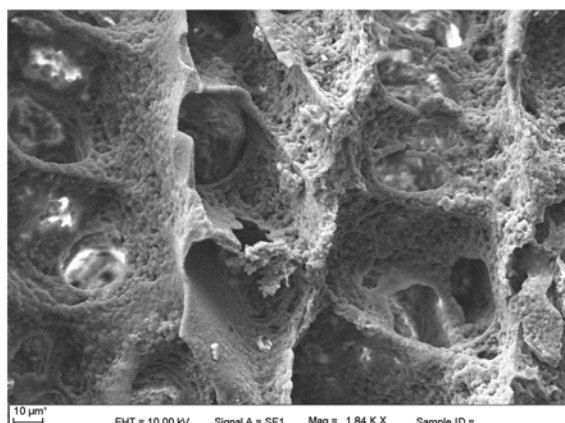


Figure 2. SEM images of poly(HEMA-MAH) cryogels.



Scientific / ICE 3500, UK) and inductively coupled plasma optical emission spectrophotometry (Thermo Scientific / ICAP 6500, UK) were used for the determination of lead amount adsorbed, and each experiment was repeated thrice for the statistical reliability.

RESULTS and DISCUSSION

To determine the lead amount adsorbed onto the cryogels, wastewater sample was obtained from an inorganic material manufacturer. The electrostatic interaction was dominant throughout all experiments.

The Adsorption-Desorption Experiments

Because of highly recommended electrostatic interaction between the ligand and target molecules was achieved during this study, the interaction between cryogels and lead was almost completed in 5 minutes. (Figure 3). The plateau observed after 5th minute was because all binding sites were engaged with the lead atoms in the solution and no more interaction can occur. On the contrary, the adsorption onto poly(HEMA-MAH) cryogels was increased with increasing concentration with no plateau observed up to 1000 ppm due to the fact that the number of ligands attached to the structure was high and also the target lead ion was quite small as compared to a polymeric structure resulting high number of interactions with each functional group on the polymeric cryogel (Figure 3).

The poly(HEMA-MAH) cryogels had uptake lead of approximately 747 μmole in a fast and cost-friendly single step process for the removal of Pb^{2+} ions.

The Pb^{2+} adsorption capacity of poly(HEMA-MAH) cryogel was determined from a sample of wastewater from a local fabric manufacturer. To run the experiment, sample and HNO_3 ratio was specified in the ratio of 1:1. The lead adsorption capacity of cryogel was determined as approximately 34% of all wastewater which is quite high.

The lead-adsorption behaviour of cryogel was ascertained by the isotherm estimation. For that purpose, the Langmuir and Freundlich adsorption isotherm's constants were calculated primarily. According to the graphs given in Figure 4 (time and concentration versus adsorbed lead amount), the single layer interaction was preponderant on the homogeneous surface (Table 1). The adsorption isotherm constants can be found in Table 1. The Redlich-Peterson adsorption isotherm model was also investigated which gave quite an effective result, especially for heavy metal adsorption interactions. In Table 1, β (0.36) value was in good agreement with the Langmuir adsorption model. In this adsorption system, the dominating model is the pseudo-second-order kinetic model due to the higher correlation coefficient value (1.00) meaning that the process was run as chemically controlled.

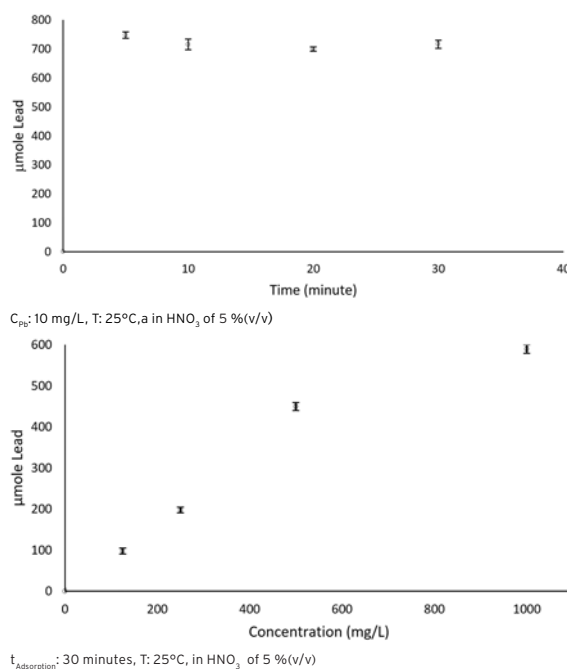


Figure 3. Lead adsorption onto poly(HEMA-MAH) cryogel.

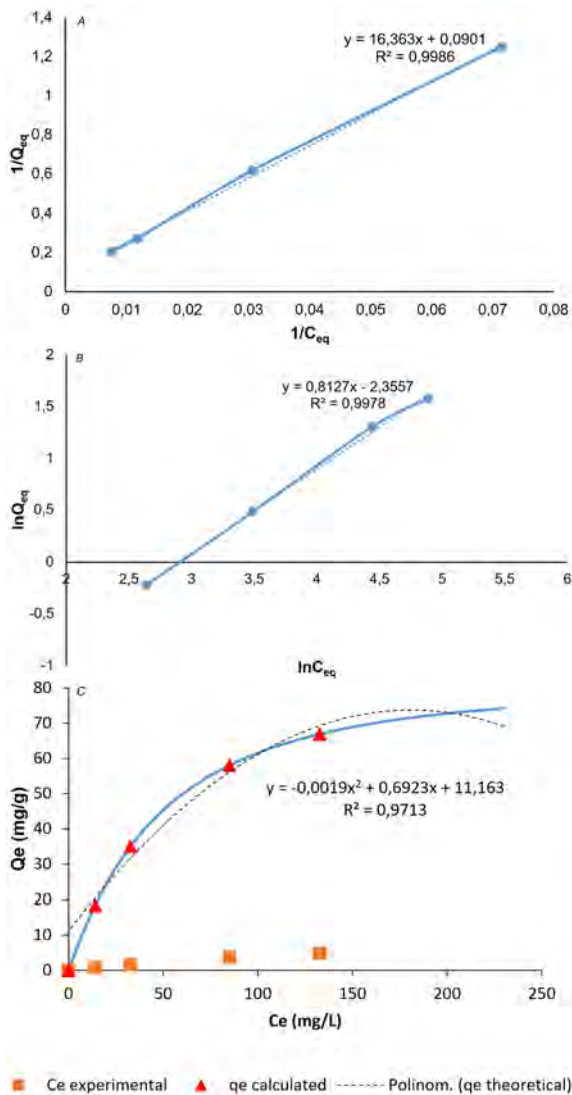


Figure 4. A) Langmuir, B) Freundlich and C) Redlich- Peterson Adsorption Isotherms.

Table 1. Adsorption isotherm and kinetic parameters for the aluminium adsorption process.

Langmuir Isotherm				Freundlich Isotherm			Redlich-Peterson Isotherm			
Q_{exp}	Q_{max}	b	R^2	n	K_f	R^2	K	a	b	R^2
6,12	11,98	0,005	0,9986	0,812	0,118	0,9978	0,18	0,69	0,36	0,9713
				Pseudo-First-Order			Pseudo-Second-Order			
Q_{exp} (mg/g)	q_{eq} (mg/g)	k_1 (1/min.)	R^2	q_{eq} (mg/g)	k_2 (g/mg.min.)	R^2				
1,96	3,58	0,0044	0,81	1,90	0,3792	1,00				

CONCLUSION

The importance of lead removal is getting more and more increased because of increasing number of diseases, especially anaemia, encephalopathy, and colic disease. We are exposed to heavy metals, especially lead, every day from air, water, soil and food products. In this study, poly(HEMA-MAH) cryogel was synthesized to provide a polymeric material for the removal of lead from wastewater. It was observed that chemical dynamics were dominated during adsorption occurring in one layer homogenously. The wastewater sample obtained from the manufacturer was the important target medium to see the lead adsorption performance of the cryogel to see whether this polymeric material will run or not. A cost-effective, short-timed and simple method was applied in this study. As a concluding remark, it can be said that the poly(HEMA-MAH) cryogel is promising alternative for efficient heavy metal, especially Pb^{2+} removal, contrary to conventional techniques.

REFERENCES

- Lalhruitluanga H, Jayaram K, Prasad MNV, and Kumar KK, Lead(II) adsorption from aqueous solutions by raw and activated charcoals of Melocanna baccifera Roxburgh (bamboo)-A comparative study. Journal of Hazardous Materials 175 (2010) 311-318.
- Ochieng H, de Ruyter van Steveninck E, and Wanda F, Mouthpart deformities in Chironomidae (Diptera) as indicators of heavy metal pollution in northern Lake Victoria, Uganda. African Journal of Aquatic Science 33 (2008) 135-142.
- WHO, WHO Guidelines for Drinking-Water Quality, fourth ed., WHO Press, Geneva. (2011).

4. Mazaheri H, Ghaedi M, Hajati S, Dashtian K, and Purkait MK, Simultaneous removal of methylene blue and Pb²⁺ ions using ruthenium nanoparticle-loaded activated carbon: response surface methodology. *RSC Advances* 5 (2015) 83427–83435.
5. Vuković GD, Marinković AD, Škapin SD, Ristić MĐ, Aleksić R, Perić-Grujić AA, and Uskoković PS, Removal of lead from water by amino modified multi-walled carbon nanotubes. *Chemical Engineering Journal* 173 (2011) 855–865.
6. Salem A and Akbari Sene R, Removal of lead from solution by combination of natural zeolite-kaolin-bentonite as a new low-cost adsorbent. *Chemical Engineering Journal* 174 (2011) 619–628.
7. Pawar RR, Bajaj HC, and Lee S–M, Activated bentonite as a low-cost adsorbent for the removal of Cu (II) and Pb (II) from aqueous solutions: Batch and column studies. *Journal of Industrial and Engineering Chemistry* 34 (2016) 213–223.
8. Martins BL, Cruz CCV, Luna AS, and Henriques CA, Sorption and desorption of Pb²⁺ ions by dead *Sargassum* sp. biomass. *Biochemical Engineering Journal* 27 (2006) 310–314.
9. Tchounwou PB, Yedjou CG, Patlolla AK, and Sutton DJ, Heavy metal toxicity and the environment, in *Molecular, clinical and environmental toxicology*. 2012, Springer. p. 133–164.
10. Jamshidi M, Ghaedi M, Dashtian K, Hajati S, and Bazrafshan A, Ultrasound-assisted removal of Al³⁺ ions and Alizarin red S by activated carbon engrafted with Ag nanoparticles: central composite design and genetic algorithm optimization. *RSC Advances* 5 (2015) 59522–59532.
11. Jamshidi M, Ghaedi M, Dashtian K, Ghaedi AM, Hajati S, Goudarzi A, and Alipanahpour E, Highly efficient simultaneous ultrasonic assisted adsorption of brilliant green and eosin B onto ZnS nanoparticles loaded activated carbon: Artificial neural network modeling and central composite design optimization. *Spectrochimica Acta Part A: Molecular and Biomolecular Spectroscopy* 153 (2016) 257–267.
12. Roosta M, Ghaedi M, Daneshfar A, and Sahraei R, Experimental design based response surface methodology optimization of ultrasonic assisted adsorption of safranin O by tin sulfide nanoparticle loaded on activated carbon. *Spectrochimica Acta Part A: Molecular and Biomolecular Spectroscopy* 122 (2014) 223–231.
13. Say R, Birlik E, Denizli A, and Ersöz A, Removal of heavy metal ions by dithiocarbamate-anchored polymer/organosmectite composites. *Applied Clay Science* 31 (2006) 298–305.
14. NasiriAzadF, GhaediM, DashtianK, MontazerzohoriM, Hajati S, and Alipanahpour E, Preparation and characterization of MWCNTs functionalized by N-(3-nitrobenzylidene)-N[prime or minute]-trimethoxysilylpropyl-ethane-1,2-diamine for the removal of aluminum(iii) ions via complexation with eriochrome cyanine R: spectrophotometric detection and optimization. *RSC Advances* 5 (2015) 61060–61069.
15. Lalmunsiana, Lee SM, and Tiwari D, Manganese oxide immobilized activated carbons in the remediation of aqueous wastes contaminated with copper(II) and lead(II). *Chemical Engineering Journal* 225 (2013) 128–137.
16. Gupta SS and Bhattacharyya KG, Kinetics of adsorption of metal ions on inorganic materials: a review. *Advances in Colloid and Interface Science* 162 (2011) 39–58.
17. González MA, Pavlovic I, and Barriga C, Cu(II), Pb(II) and Cd(II) sorption on different layered double hydroxides. A kinetic and thermodynamic study and competing factors. *Chemical Engineering Journal* 269 (2015) 221–228.
18. Liu Z and Zhang F–S, Removal of lead from water using biochars prepared from hydrothermal liquefaction of biomass. *Journal of Hazardous Materials* 167 (2009) 933–939.
19. Massalimov IA, Il'yasova RR, Musavirova LR, Samsonov MR, and Mustafin AG, Use of micrometer hematite particles and nanodispersed goethite as sorbent for heavy metals. *Russian Journal of Applied Chemistry* 87 (2015) 1456–1463.
20. Kumari M, Pittman Jr CU, and Mohan D, Heavy metals [chromium (VI) and lead (II)] removal from water using mesoporous magnetite (Fe₃O₄) nanospheres. *Journal of Colloid and Interface Science* 442 (2015) 120–132.
21. Erto A, Giraldo L, Lancia A, and Moreno-Piraján JC, A comparison between a low-cost sorbent and an activated carbon for the adsorption of heavy metals from water. *Water, Air, and Soil Pollution* 224 (2013).
22. Sen Gupta S and Bhattacharyya KG, Adsorption of heavy metals on kaolinite and montmorillonite: a review. *Physical Chemistry Chemical Physics* 14 (2012) 6698–6723.
23. Nguyen TC, Loganathan P, Nguyen TV, Vigneswaran S, Kandasamy J, and Naidu R, Simultaneous adsorption of Cd, Cr, Cu, Pb, and Zn by an iron-coated Australian zeolite in batch and fixed-bed column studies. *Chemical Engineering Journal* 270 (2015) 393–404.
24. Yang W, Tang Q, Wei J, Ran Y, Chai L, and Wang H, Enhanced removal of Cd (II) and Pb (II) by composites of mesoporous carbon stabilized alumina. *Applied Surface Science* 369 (2016) 215–223.
25. Say R, Garipcan B, Emir S, Patır S, and Denizli A, Preparation of poly (hydroxyethyl methacrylate-co-methacrylamidohistidine) beads and its design as a affinity adsorbent for Cu (II) removal from aqueous solutions. *Colloids and Surfaces A: Physicochemical and Engineering Aspects* 196 (2002) 199–207.
26. Kose K and Uzun L, PolyGuanine methacrylate cryogels for ribonucleic acid purification.
27. Köse K, Erol K, Özgür E, Uzun L, and Denizli A, PolyAdenine cryogels for fast and effective RNA purification. *Colloids and Surfaces B: Biointerfaces* 146 (2016) 678–686.
28. Erol K, Köse K, Uzun L, Say R, and Denizli A, Polyethyleneimine assisted-two-step polymerization to develop surface imprinted cryogels for lysozyme purification. *Colloids and Surfaces B: Biointerfaces* 146 (2016) 567–576.

Thermal Grooving by Surface Diffusion: a Review of Classical Thermo-Kinetics Approach

Oncu Akyildiz¹, and Tarik Omer Ogurtani²

¹Department of Metallurgical and Materials Engineering, Hitit University, 19030, Corum, TURKEY.

²Department of Metallurgical and Materials Engineering, Middle East Technical University, 06531, Ankara, TURKEY.

ABSTRACT

In polycrystalline materials wherever a grain boundary intersects a free surface and whenever the topographic variation associated with the atomic motion is favored by total free energy dissipation, the material surface grooves. In this review, we focused on the grain boundary grooving by surface diffusion which is an active mechanism at moderate temperatures and for grooves small in size. Starting with a description of the classical thermo-kinetics treatment of the process, we briefly reviewed Mullins' very first modeling effort with a small slope assumption at the groove root and further considerations regarding finite slopes, different grain geometries, and anisotropic surface free energies. We concluded by giving examples of experimental observations in accord with theoretical calculations.

Keywords: Thermal grooving; Grain boundary groove; Surface diffusion

Article History:

Received: 2016/10/17

Accepted: 2016/12/02

Online: 2017/06/30

Correspondence to: O Akyildiz,
Department of Metallurgical and Materials
Engineering, Hitit University, 19030, Corum,
TURKEY

Tel: +90 364 227 4533/1282;

Fax: +90 364 227 4535

E-Mail: oncuakyildiz@hitit.edu.tr

INTRODUCTION

Polycrystalline materials are composed of tiny perfect crystalline regions (grains) in between internal interfaces called grain boundaries. Grain boundaries and the external interfaces (i.e. free surfaces which separate the material from the environment) determine the morphology of the material at a major extent.

A material may change its morphology through interface motion if a driving force exists. An important special case, which is the focus of this review, is the grain boundary grooving. Wherever a grain boundary intersects a free surface and whenever the topographic variation associated with the atomic motion is favored by total free energy dissipation, the surface grooves. Grooving can occur via several mass transport mechanisms, such as surface diffusion, bulk diffusion, and evaporation and condensation. Surface diffusion dominates for temperatures far below the melting temperature, and for grooves less than 10 micron in size [1]. If the surface evolution is driven solely by the total excess free energies associated with the interfaces the resulting force for motion is conventionally called a capillary force,

and the new formation is termed as a *thermal groove*. In addition to a capillary force, a force for interface motion is produced whenever motion of the interface allows an applied force to perform work: such a force is an applied force [2].

A major portion of the literature on morphological evolution solid surfaces and interfaces mainly rely on classical thermodynamics. The idea is to minimize the free energy of the system by suitable mechanism of mass transport. Considering systems at equilibrium a driving force is determined from the total free energy variation, and a linear kinetic law is used to relate the driving force to the flux. Using this flux, surface shape is updated according to mass conservation.

Mullins [3] successfully cast this approach to the problem of thermal grooving in 1957 by imposing suitable boundary conditions and provide an analytic solution which provides groove profile as a function of time and position under some assumptions. After that time several improvements has been done by several researchers who follow the classical approach. In this review

article we will briefly discuss these concepts and conclude by giving examples of experimental observations compared with theoretical calculations.

It should also be mentioned that this review reflects authors' personal perspective on this specific (yet still broad enough) part of the broader topic of thermodynamics and kinetics of solid surfaces and interfaces.

Classical thermo – kinetics theory

Kinetics of morphological changes by surface diffusion

It is useful to outline the surface diffusion driven motion of an arbitrary surface before proceeding further into the detailed literature review. The atomic flux (vector field; the bar signs over symbols are to denote vector quantities) on such a solid surface given in figure 1 may be defined at a per length basis by:

$$\bar{J}_\sigma = \frac{\text{\# of atoms}}{(\text{length})(\text{time})} \quad (1)$$

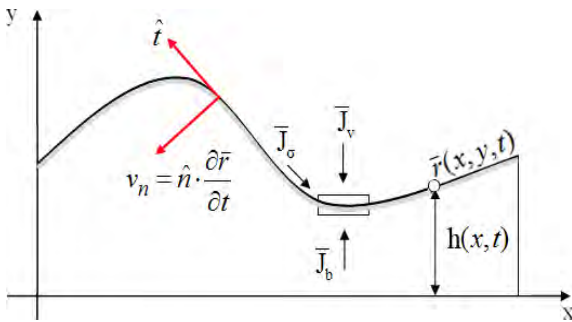


Figure 1. An arbitrary surface in the x-y plane. \hat{t} is the unit tangent and \hat{n} is the unit normal vector, the subscripts σ, b, v on the fluxes denote the surface, bulk, and void phases respectively. When evaporation condensation mechanism is active, J_b and J_v entering (leaving) the surface element should also be considered. At a given time any point on the surface may be represented by position vector $\bar{r}(x, y)$.

When a surface element gains atoms, it moves with a velocity v_n (scalar field) in the direction normal to the surface. Defining Ω as the volume per atom in the solid the ratio v_n/Ω gives the atoms gained per unit area per unit time. This quantity is related to the flux divergence through conservation of mass:

$$\frac{v_n}{\Omega} + \nabla \cdot \bar{J}_\sigma = 0 \quad (\text{the continuity equation}) \quad (2a)$$

$$v_n = -\Omega \nabla \cdot \bar{J}_\sigma \quad (2b)$$

Once the diffusion flux is obtained surface can be evolved using the velocity calculated by this equation. The atomic flux on the surface can be related to the driving force for diffusion through atomic mobility M by using a linear kinetic law [4, 5]:

$$\bar{J}_\sigma = M\bar{F} \quad (3)$$

This connection is a typical consequence of linear irreversible thermodynamics as underlined by Sun and Suo [4, 5] and adopted by Herring [6] and Mullins [3].

The literature of diffusion controlled surface morphological changes is fulfilled by the following concept: the driving force in Eq. (3) may be interpreted as a gradient energy which is everywhere continuous even at the singularities; otherwise the flux might go to infinity. The assumed surface diffusion potential is a scalar field that reflects a change in energy that results from the motion of species; therefore, it includes energy-storage mechanisms and any constraints on motion [2]. Therefore all efforts start with a definition of the term surface chemical potential, μ_σ whose gradients drive the overall processes.

Following Herring, the driving force in Eq. (3) is a vector on the interface that is derived from gradient of a scalar field which has units of energy per atom. If atoms diffuse from an interfacial element with high potential to another with low potential, then the driving force is the negative gradient of the surface diffusion potential μ_σ :

$$\bar{F} = -\nabla \mu_\sigma \quad (4)$$

Substituting Eqs. (4→3→2) and assuming a position independent atomic mobility one can relate the normal velocity of the free surface to the Laplacian of the surface diffusion potential:

$$v_n = \Omega M \nabla^2 \mu_\sigma \quad (5)$$

Another common representation of Eq. (5) may be obtained by the following form of the Nernst – Einstein equation which ties the mobility and surface self-diffusivity, D_σ :

$$M = \frac{h_\sigma D_\sigma}{\Omega kT} \quad (6)$$

Here h_σ is the thickness of the surface layer, k is the Boltzmann constant and T is the absolute temperature. Substitution Eq. (6→5) yields:

$$v_n = \frac{D_\sigma h_\sigma}{kT} \nabla^2 \mu_\sigma \quad (7)$$

Energetics of morphological changes by surface diffusion

If there is no exchange of energy between the solid and its surroundings then the change in free energy for a given change in shape represents the driving force for that shape change (Eq. 4). So, the next step is to obtain a proper definition for the total free energy that could be used in connection with Eq. (7). The very first study in this field came from Herring in 1951 which strictly rely on the equilibrium thermodynamics and the Gibbs description of interfaces and surfaces [7, 8]. He extends the classical Gibbs-Thomson equation for an orientation dependent surface tension γ_s , as in a crystal.

Herring's equation of curvature dependent chemical potential

The Gibbs-Thomson equation reflects typical consequence of the dependence of equilibrium vapor pressure of a liquid drop on its radius of curvature; i.e. it relates the curvature of a surface to the chemical potential of the surface atoms when surface tension γ_s is independent of orientation. Herring's theory, in a similar way, assumes that the free energy of the system is the surface energy summed over all surfaces and grain boundaries, and the amount of free energy decrease is associated with per unit volume of matter moving per unit distance on the surface and as a result describes a driving force at every point on the solid surface.

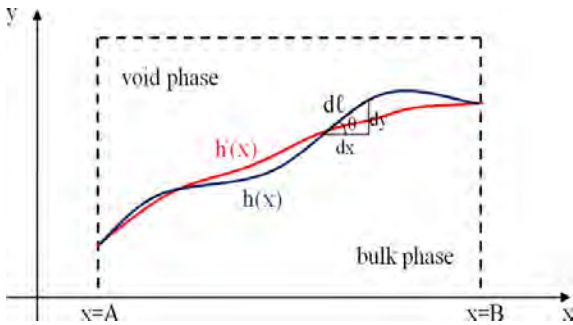


Figure 2: The curve $h(x)$ between $x=A$ and B represents a portion of the cross section of a surface between bulk and void phases. $h(x)$ is the surface perturbed by an infinitesimal amount $\delta h(x)$.

Mullins [9] gives a derivation of Herring's equation using calculus of variations in two dimensions by considering a monocomponent system, under no applied pressure. In such a system surface tension γ_s is equal to the specific surface free energy, f_σ . Then the value of the surface free energy, F associated with the curve in figure 2 from A to B , per unit depth, is given by the following line integral:

$$F_\sigma = \int_A^B \gamma_s d\ell = \int_A^B \gamma_s(h_x) \sqrt{1+h_x^2} dx = \int_A^B G(h_x) dx \quad (8)$$

Here h_x represents differentiation with respect to x ;

simply it is the slope of the curve at any point and used as an argument for γ , since it determines the orientation of the surface element. Then if an infinitesimal rearrangement of material forms the new surface: $h'(x)=h(x)+\delta h(x)$. The corresponding variation in F_σ is obtained by calculus of variations as:

$$\delta F_\sigma = \int_A^B \frac{dG}{dh_x} \delta h_x dx = \int_A^B \frac{dG}{dh_x} \frac{d(\delta h)}{dx} dx = - \int_A^B \frac{d}{dx} \left(\frac{dG}{dh_x} \right) \delta h dx \quad (9)$$

Here for simplicity $\delta h(A)=\delta h(B)=0$ and $\int_A^B \delta h(x) dx = 0$. Assuming the chemical potential $\mu'_\sigma = \mu_\sigma + \mu_0$ to be uniquely determined at all elements of the surface apart from the constant μ_σ , δF must also be given by the following expression:

$$\delta F_\sigma = \frac{1}{\Omega} \int_A^B (\mu_\sigma + \mu_0) \delta h dx = \frac{1}{\Omega} \int_A^B \mu_0 \delta h dx \quad (10)$$

Here, μ_σ is defined as the chemical potential at standard state which can arbitrarily be assigned to the value zero in the reservoir, Ω is the atomic volume and $\delta h dx / \Omega$ gives the number of atoms added to the interval dx . Subtracting Eq. (9)→(10):

$$0 = \int_A^B \left\{ \frac{d}{dx} \left(\frac{dG}{dh_x} \right) + \frac{\mu_0}{\Omega} \right\} \delta h dx \quad (11)$$

Since δh is arbitrary:

$$\mu_0 = -\Omega \frac{d}{dx} \left(\frac{dG}{dh_x} \right) = -\Omega \frac{d}{dx} \left(\frac{d}{dh_x} \left(\gamma_s(h_x) \sqrt{1+h_x^2} \right) \right) \quad (12)$$

Using following equalities in performing differentiations:

$$\theta = \arctan(h_x) \quad \frac{d\gamma_s}{dh_x} = \frac{1}{1+h_x^2} \frac{d\gamma_s}{d\theta} \quad \frac{d}{dx} = h_{xx} \frac{d}{dh_x}$$

Eq. (12) yields:

$$\mu_0 = -\Omega \left(\gamma_s + \frac{d^2\gamma_s}{d\theta^2} \right) \frac{h_{xx}}{(1+h_x^2)^{3/2}} = \Omega \left(\gamma_s + \frac{d^2\gamma_s}{d\theta^2} \right) \kappa \quad (13)$$

Here, $\kappa = -h_{xx} (1+h_x^2)^{-3/2}$ is the curvature at a point on the surface and taken to be positive when the surface is concave towards the bulk. For isotropic γ , as in liquids, Eq. (13) directly reduces to Gibbs-Thomson equation. Substituting Eq. (13) into (7), one may specify a governing differential equation for capillarity induced evolution of surfaces and interfaces.

Mullins' theory of thermal grooving

Thermal grooving at grain boundaries is a process of capillary – driven evolution of surface topography in the region where a grain boundary emerges to intersect a free surface of a polycrystalline material. Mullins [3] derived a general PDE for the rate of change of the profile of a surface for profile changes occurring by surface diffusion mechanism under the following assumptions:

- (1) The system is closed and contains a metal poly-crystal in quasi-equilibrium with its vapor.
- (2) Interface properties are independent of crystallographic orientation.
- (3) All matter transport occurs by surface self-diffusion.
- (4) Macroscopic concepts such as surface free energy and curvature are valid.
- (5) There is negligible flow of matter out of the grain boundary; instead, the role of the boundary is to maintain the correct equilibrium angle.
- (6) Absolute value of the profile slope is everywhere small compared to unity; the small slope assumption (SSA).

Under these assumptions he follows the very same procedure described above (Eq. 13→7) and obtains following equation:

$$v_n = \frac{D_\sigma \gamma_s \dot{U}^2 v}{kT} \nabla^2 \kappa \quad (21)$$

Here, Mullins adopted $v = \frac{h_\sigma}{\Omega}$ as the number of per unit area, instead of using h_σ itself. Owing to isotropy he collects all physical constants into one ($B = D_\sigma \gamma_s \Omega^2 v / kT$) and rewrites Eq. (21) explicitly in terms of $h(x,t)$:

$$\frac{\partial h}{\partial t} = -B \frac{\partial}{\partial x} \left((1 + h_x^2)^{-1/2} \frac{\partial}{\partial x} \left(h_{xx} (1 + h_x^2)^{-3/2} \right) \right) \quad (22)$$

This nonlinear PDE is in fourth order in space and hard to solve analytically. Mullins linearized this equation referring to the assumption (6) given above: slope of the surface is everywhere small compared to unity.

$$\frac{\partial h}{\partial t} = -B h_{xxxx} \quad (23)$$

He considers a symmetrically disposed stationary grain boundary at $x=0$ that is perpendicular to the free surface as in Figure 3. Then he formulates the following initial and boundary conditions:

$$h(x, 0) = 0 \quad (24a)$$

$$h_x(0, t) = \tan \theta = m \ll 1 \quad (24b)$$

$$J_{gb}(0, t) = h_{xxx}(0, t) = 0 \quad (24c)$$

$$h(\pm\infty, t) = h_x(\pm\infty, t) = 0 \quad (25d)$$

Eq. (1.4.4a) is an initial condition for the problem and assumes an initially flat surface. Eqs. (1.4.4b, c) are the boundary conditions for the triple junction; the first one fixes the dihedral angle ($\phi = \pi - 2\theta$) at the groove root through mechanical equilibrium ($\sin\theta = \gamma_{gb} / 2\gamma_s = \lambda$; where λ may be called as the wetting parameter) and the second sets the flux of atoms out of the boundary to zero. And 1.4.4d assures that flat surface remote from the triple junction at all time.

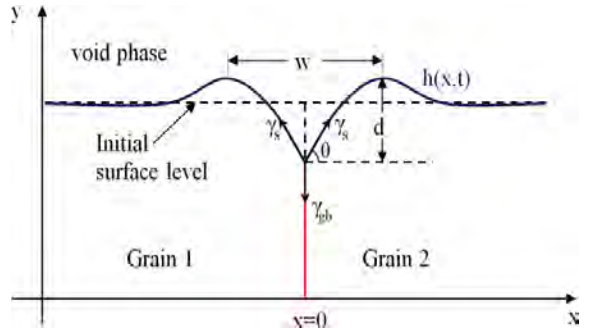


Figure 3. Sketch of the curve $h(x,t)$; the surface profile function. d is the groove depth measured from the maxima and w is the separation between the two maxima, namely the groove width. γ_{gb} and γ_s are the grain boundary and surface tensions respectively. $\phi = \pi - 2\theta$ is the equilibrium dihedral angle, force balance requires $2\gamma_s \sin\theta = \gamma_{gb}$ at the groove root.

Mullins [57] obtains an analytic solution of Eq. (23) subjected initial and boundary conditions defined in Eqs. (24) as:

$$y(u, t) = m(Bt)^{1/4} Z(u) \quad \text{with}$$

$$u = \frac{x}{(Bt)^{1/4}} \quad \text{and} \quad Z(u) = \sum_{n=0}^{\infty} a_n u^n \quad (25a)$$

$$a_0 = \frac{-1}{\sqrt{2}\Gamma(5/4)}; \quad a_1 = 1; \quad a_2 = \frac{-1}{2\sqrt{2}\Gamma(3/4)}; \quad a_3 = 0; \quad (25b)$$

$$a_{n+4} = a_n \frac{n-1}{4(n+1)(n+2)(n+3)(n+4)}$$

Here, Γ is the gamma function. It is inferred from Eq. (25) that the groove shape is dependent upon the material constant $m = \tan\theta$; but is independent of time and the physical parameters comprising B . Mullins [3] stated that the groove instantly attains a constant shape whose linear dimensions grow in proportional to $t^{1/4}$, and deduce two technically important equations:

$$d = 0.973m(Bt)^{1/4} \quad (26a)$$

$$w=4.6(Bt)^{1/4} \quad (26b)$$

The first kinetic equation stands for the steady shape grooves' depth, d and second for its width, w (see Fig. 3). These two equations give possibility to determine surface diffusion constants experimentally

After Mullins' publication [3] in 1957 considerable amount of work had been dedicated by several investigators to obtain a solution that accounts finite slopes at the groove root; some of them will be cited here. Robertson [10] transforms the nonlinear PDE to an ordinary differential equation of $Z(u)$ by inserting Eq. (25a) to Eq. (22) and numerically integrates it to obtain solutions for finite slopes ranging from 0 to 4. He found groove depths lower than estimated by Eq. (26a) for finite slopes. Zhang & Schneibel [11] use method of lines approach to solve Eq. (22); Khenner et al. [12] categorize the problem as a two dimensional initial boundary value problem of type Hamilton-Jacobi and proposed a numerical solution by using a level set method. Both articles address and discuss several numerical methods to solve the nonlinear PDE. The conclusion shared is that the groove profile stays self similar; the width and height of the groove grow with time t as $t^{1/4}$ as predicted by Mullins' small slope solution.

Several cases regarding to geometry had also been studied in the literature. Mullins theory assumes an isolated groove and it can be inferred from his solution that every film subjected to a long enough annealing time will rupture. Hackney & Ojard [13] consider an array of equally spaced parallel grain boundaries with the same symmetric contact angle (Fig. 4a) under SSA. They employ following boundary conditions:

$$h_x(R, t) = h_x(-R, t) = \tan \theta = m \ll 1 \quad (27a)$$

$$J_{gb}(R, t) = h_{xxx}(R, t) = 0 \quad (27b)$$

$$h_x(0, t) = 0 \quad (27c)$$

The third one is the symmetry condition at the center of the grain, whilst the others are self explanatory for a groove root placed to a distance R . They gave an analytic solution for Eq. (23) that accounts finite grain size $2R$. Later Zhang and Schneibel [11] and Khenner [14] studied the very same system by solving Eq. (22) numerically. Both authors observe termination of grooving at long times after formation of identical circular arcs that connect adjacent grain boundaries; a result anticipated long time ago by Srolovitz and Safran [15] merely from energetic calculations. They show that a groove may go to a finite depth even after an infinite time to anneal and estimate the conditions under which film rupture happens (groove divides the bicrystal into two pieces;

and therefore give rise to island formation on a substrate) as a function of film aspect ratio ($2R/w_0$; see Fig. 22) and dihedral angle.

Huang et al. [16] consider a different set of boundary conditions for the end points that are free to move in lateral direction to account finite plate like grains that have semicircular ends (constituting a closed loop, Fig. 4b). Through large number of finite element analyses they have deduced an empirical formula that relates minimum dihedral angle (below which no splitting occurs) to the film aspect ratio.

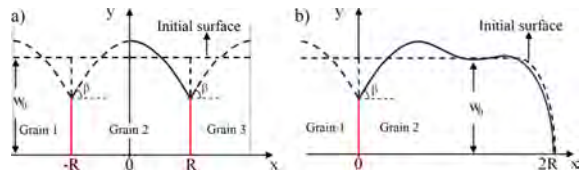


Figure 4. Schematic representation of a) continuous array of grains, b) plate like grains that have semicircular ends. Symmetry prevails due to assumed isotropic surface properties and solution for the solid lines is enough for interpretation.

Ogurtani and Akyildiz [17] utilize three different; reflecting, interactive (Fig. 4a) and free moving (Fig. 4b) boundary conditions and perform thermal grooving simulations on tilted and normal grain boundaries. Yet, their way of treating the triple junction singularity was completely different from those cited here and based on a mathematical model which flows only from fundamental postulates of irreversible thermodynamics. They showed existence of a transient regime and incorporated this regime into their penetration depth formula by stating that the rate of this transient evolution process obeys the first order reaction kinetics. They stated that this regime is totally ignored by researchers employing Mullins' boundary condition at groove root (constant slope).

Surface energy anisotropy

Maybe the most serious simplification made in the Mullins model is the assumption of the full isotropy of the surface energy. Obviously, this assumption justifies the use of the continuum approach, with the macroscopic curvature as the only driving force for surface diffusion. However, the importance of the surface free energy anisotropy in determining the dihedral angle of the groove and the groove shape was recognized soon after Mullins' work. Grain boundary grooves can develop facets due to anisotropic surface energy. The presence of facets on surfaces of grooves poses intricate modeling issues.

The value of surface energy per unit area of a given crystallographic surface orientation is determined by the fine scale structure of that surface. For a high symmetry

orientation in a crystal the surface is atomically flat. For other orientations close to this surface, the structure usually consists of flat terraces with well-defined local surface energies, separated by atomic scale ledges or steps as illustrated schematically in Figure 5. The steps alter the macroscopic surface energy by an amount corresponding to their energy of formation in the configuration relevant to the structure. Below a characteristic roughening transition temperature T_R , “a nominally flat surface of a crystal that is misoriented by a small angle from a high symmetry direction consists of a train of straight parallel steps” [18]. At finite temperature, such “vicinal” surfaces can be stable and can appear on rounded edges on the equilibrium crystal shape.

With increasing temperature, the rounded regions grow at the expense of facets and at T_R (usually below the melting temperature) the surface becomes smoothly rounded as illustrated schematically in Figure 6. Below T_R , “in the Wulff construction of the surface specific Gibbs free energy, the cusp in the γ -plot or the non-analytic term in the surface tension exists as a result of the finite free energy cost per unit length in the formation of a step”. Therefore “the disappearance of facets is connected to disappearance of cusps in the γ -plot, and implies that the step free energy vanishes and free proliferation of steps is expected for $T > T_R$ ” [19].

Mykura [20] stated that, in the case of a coherent twin

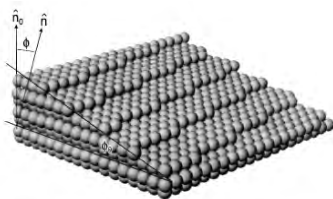


Figure 5. Structure of an fcc $(3\bar{2}16)$ surface vicinal to the fcc (001) surface. Figure illustrates zero-temperature steps and kinks that occur on high index (or ‘vicinal’) surfaces [19].

boundary, the surface anisotropy may even cause the formation of a ridge instead of a groove. Bonzel and Mullins [21] considered the evolution of a pre-perturbed surface topography of the vicinal surface, which is essentially anisotropic. It was found that in the small slope approximation, the flux of the surface atoms is again proportional to the gradient of the surface curvature defined in the proper frame of reference, but should be substituted by a complex expression which depends on the energy of an isolated step, the energy of interaction between steps and the direction of perturbation.

The grain boundary grooving at the singular surfaces were extensively studied by Rabkin et al. [22], Klinger and Rabkin [23], Rabkin and Klinger [24] by explicitly introducing faceted and rough regions, each with different isotropic

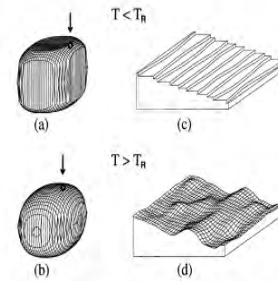


Figure 6. Schematic illustration of equilibrium crystal shapes at finite temperatures, T for a simple cubic model with the nearest neighbor interaction. Equilibrium crystal shapes a) at $T < T_R$: stable (001) facets and b) at $T > T_R$: continuously rounded, have no facet. The regions marked by arrows in a) and b), are vicinal to the low index (001) surface. The difference in mesoscopic structures below and above the roughening temperature is given in c) and d) [19].

surface energies. Zhang et al. [25] derive models describing groove growth while the dihedral angle changes. According to these authors the change in the dihedral angle is caused by the change in the surface energy due to surface contaminations. They express the dihedral angle as a function of time, and after a series of simulations they conclude that changes in the dihedral angle affect the growth exponent for the groove depth much more than the groove width. Growth exponents for depth values as high as 0.4 are possible in this model, whereas Mullins’ model predicts an exponent of 0.25 for both the width and depth of the groove. Later Akyildiz et al. [26], analyzed the experimental thermal grooving data reported by these authors, and compared them with their simulation results based on a mesoscopic nonequilibrium thermodynamics treatment. This investigation showed that the observed changes in the dihedral angles are strictly connected to the transient behavior of the simulated global system, and manifest themselves at the early stage of the thermal grooving phenomenon, which is completely overlooked by Mullins’ based approach.

Zhang et al. [27] study the effect of anisotropic surface free energy on thermal grain boundary grooving using modeling, simulation and experiments on tungsten. Based on Herring’s model they show that, for tungsten, when the anisotropy is mild, the groove profiles are self-similar in the evolution but are often not in proportion to those developed under isotropic material properties. The grooving kinetics again obeys power law with the exponent 0.25. When the anisotropy is critical surface faceting occurs. And, when it is severe the facets coarsen in the evolution. They exhibit the groove profiles in evolution under different degrees of anisotropy.

Wong and coworkers [28-32] study orientation dependent surface stiffness instead of the surface free energy explicitly in their treatments. They regularize the surface stiffness by replacing the Dirac delta function by sharply peaked functions while former use an analytic form for the

surface free energy which then leads to an analytic surface stiffness and find that faceted grooves still grow with time t with an exponent of 0.25. They stated that, anisotropic groove can be smooth if the groove surface does not cross a facet orientation, moreover the groove has the same shape as the corresponding isotropic groove, but the growth rate is reduced by a factor that depends on the degree of anisotropy. Recently, Ogurtani [33] has reached exactly the same conclusion for the four fold symmetry by applying special analysis on the surface Gibbs free energy function adapted from Ramasubramaniam and Shenoy [34]. The analytic theory developed in conjunction with the extensive computer simulation experiments irrecoverably proved that the smooth grain boundary groove profiles can be represented by the modified Mullins' function [3] with great precision for the symmetrically disposed bicrystal, where the Mullins' rate parameter B is modified by an anisotropy constant Ψ as, $B \Rightarrow B \times (1 - \Psi)$ and the isotropic complementary dihedral angle in the slope parameter is replaced by its counterpart in anisotropic case.

Ramasubramaniam and Shenoy [34] made a very serious and successful attempt to obtain a weak solution of the evolution kinetics of faceted grain boundary grooves. They produced proper connections for the TJ displacement velocity that resulted realistic groove root profiles for the symmetrically disposed grain boundary and intersecting surface configurations that are initially flat and infinite in extent. Inspiring from this article, Ogurtani [33] made a unique and transparent treatment of the grain boundary triple junction singularity by the weak solution of the extremum problem imposed by the mathematically more sound Dirichlet boundary conditions to reveal the fine topographic details of the groove root-profiles caused by the non-analyticity of the surface stiffness. In a previous work, Ogurtani [35] elaborates Hermite orthonormal functions manifold by showing that at the asymptotic limit the discrete monolayer representation of the interfaces and surfaces in more realistic Verschaffelt [36] and Guggenheim [37] model may be converged smoothly into the Gibbs abstract model by keeping the intensive variables (specific surface densities) of the interfaces and surfaces invariant and taking the layer thicknesses equal to zero at the limit and extensive variables (contents) infinite. That asymptotic approach, at the expense of the fine features of the grain boundary groove root profiles (rough and faceted regions), was successful not only in eliminating the discontinuity in the particle flux density at the grain boundary triple junction (which results Dirac delta function singularity in the gradient) but also produced most wanted continuity in the derivative of the particle flux density as speculated by Ramasubramaniam and Shenoy [34] to surmount the analytical difficulties. Ogurtani et al. [38] extend this approach to simulate tilted grain boundary grooves in thin metallic films showing four and six fold ani-

sotropy. Later Ogurtani [39] studied the very same problem by employing the modified cycloid-curtate function (MCC) as a basis (generator) for the Dirac delta distribution function on the Wulff construction. This new representation gives more flexibility on the shape of the surface profiles even its temperature dependence by considering not only the intensity but also the topography of the surface Gibbs free energy anisotropy. The utilization of the MCC function also furnished a way for the smooth passage from the soft to sharp faceting morphology by fine tuning the Wulff roughness parameter (anisotropy constant) while keeping topography index invariant.

Experimentally observed thermal grooves

Since its introduction in 1957, Mullins' theory is used extensively in determination of the surface diffusion coefficients (D_s). Once the active mass transport mechanism is confirmed (for evaporation condensation, surface and volume diffusion groove growth obeys $t^{1/2}$, $t^{1/4}$ and $t^{1/3}$ time laws respectively), the ratio of the groove depth (or width) measurements taken at different times yield the B parameter of Eq. (26). As stated before, B is a collection of physical constants: $B = D_s \gamma_s \Omega^2 v / kT$; providing surface energy γ_s is known, constant temperature experimentation gives the surface diffusivity. Grain boundary grooves are also monitored to measure the dihedral angles and therefore to obtain ratio of surface to grain boundary energies.

Classically, measurements were carried out by electron microscopy or by optical profilometry techniques such as vertical scanning interferometry, phase shifting interferometry, etc. After their invention in the early 1980s, scanning probe microscopies (SPMs) open up new possibilities for studying the surface topography of thermal GB grooves. These instruments combine the possibility to scan relatively large surface areas with atomic resolution in the vertical direction (atomic force microscopy, AFM) and in the case of scanning tunneling microscopy (STM) lateral atomic resolution can be achieved. This makes SPMs ideally suited for the quantitative characterization of surface topography.

Mullins and Shewmon [1] studied grooving kinetics of tilt boundaries in copper by interferometric analysis to show the advantages of the theory in determining D_s . They showed that the dominant process is surface diffusion, and found D_s values in agreement with the ones determined by tracer diffusion studies. A good agreement was also found by Sharma and Spitz [40] for thermal grooves on thin films of silver from a transmission electron microscopy (TEM) study. Tsoga and Nikolopoulos [41] studied grain boundary grooving on polished surfaces of polycrystalline alumina after annealing, in air, under vacuum, and in argon atmospheres in the temperature range 1273 to 1736 K. The

groove angles, measured by optical interferometry, showed no significant change with experimental conditions. It was determined that surface diffusion was the dominant mechanism for the mass transport and the calculated D_s values in agreement with the literature. Tritscher and Broadbridge [42] gave a review of experiments (for diverse materials) where surface diffusion was found to be the dominant mass transfer mechanism.

Several researchers performed AFM studies of thermal grooving. Schöllhammer et al. [43] found excellent agreement between measured and predicted groove shapes for symmetrical tilt grain boundaries in copper. Shin et al. [44] and Lee and Case [45] analyze surfaces of 99.9% alumina samples and report highly asymmetric GB grooves. Rabkin et al. [22] attributed the asymmetry they found for GB grooves in NiAl surfaces to the presence of a vicinal surface on one side of a groove and modified Mullins' [3] linearized equation for thermal GB grooving to take the negligible mass transport on the vicinal surface into account. Qualitative agreement between experimentally observed and calculated groove profiles was found. Rabkin et al. [46] studied the morphologies of GB grooves formed after annealing of molybdenum bicrystals at the temperature close to the melting point with the aid of scanning force microscopy (SFM). Three typical groove morphologies were observed: (i) Mullins-like, albeit asymmetrical grooves with the sharp root; (ii) grooves with the blunted root, and (iii) grooves with the blunted root with the secondary sub-groove with the sharp root in the region of a primary groove. Sachenko et al. [47-49] and Zhang et al. [25, 27] studied GB grooving on the surfaces of polycrystalline tungsten sheets. They found that unfaceted grooves were in qualitative agreement with the predictions of Mullins' theory of grooving by surface diffusion mass transport. They also observed asymmetric grooves between faceted and unfaceted grains showing unusual growth kinetics. Citing these works on tungsten and that of Munoz et al. [50] on alumina, Ogurtani et al. [38] designed special computer simulations and produced surface morphologies at the stationary state which are in excellent agreement with groove profiles measured by AFM and calculated D_s values which are in agreement with the literature.

CONCLUSION

Mullins' theory was a milestone in understanding of thermal grooving problem and provides an analytic solution which gives groove profile as a function of time and position using classical approach. After that time several improvements has been done by several researchers who follow the classical approach. In this review article we briefly discuss these concepts and conclude by giving examples of experimental observations compared with theoretical calculations.

It should be mentioned here that the classical approach indeed violates formation of non-equilibrium grooves and unable to describe transient states during grooving. A curious reader may refer to excellent papers by Suo [5], Ramasubramaniam and Shenoy [34], Ogurtani [35], Ogurtani and Oren [51] for a variational formulation of the problem and Ogurtani [52] for a complete irreversible thermo-kinetics treatment of solid surfaces and interfaces with triple junction singularities which is not intended to be included to this review.

REFERENCES

- Mullins WW, Shewmon PG. The kinetics of grain boundary grooving in copper. *Acta Metallurgica*, 7, 3 (1959) 163-170. doi: 10.1016/0001-6160(59)90069-0.
- Balluffi RW, Allen SM, Carter WC. *Kinetics of Materials*. John Wiley & Sons, Inc., Hoboken, NJ, USA, 2005. doi: 10.1002/0471749311.
- Mullins WW. Theory of thermal grooving. *Journal of Applied Physics*, 28, 3 (1957) 333. doi: 10.1063/1.1722742.
- Sun B, Suo Z, Yang W. A finite element method for simulating interface motion-I. Migration of phase and grain boundaries. *Acta Materialia*, 45, 5 (1997) 1907-1915. doi: 10.1016/S1359-6454(96)00323-0.
- Suo Z. Motions of microscopic surfaces in materials. *Advances in Applied Mechanics*, 33 (1997) 193-294. doi: 10.1016/S0065-2156(08)70387-9.
- Herring C. *The physics of powder metallurgy*. (Kinston WE) (p. 143). McGraw-Hill, New York, USA, 1951.
- Gibbs W. *The Collected Works of J. Willard Gibbs, Vol. I Thermodynamics*. Yale University Press, New Haven, USA, 1948.
- Defay R, Prigogine I. *Surface tension and adsorption*. (A. Bellemans). John Wiley & Sons., New York, USA, 1966.
- Mullins WW. Solid surface morphologies governed by capillarity. In *Metal Surfaces: Structure, Energetics and Kinetics* (p. 17), ASM, Cleveland, OH, USA, 1963.
- Robertson WM. Grain-boundary grooving by surface diffusion for finite surface slopes. *Journal of Applied Physics*, 42, 1 (1971) 463. doi: 10.1063/1.1659625.
- Zhang W, Schneibel JH. Numerical simulation of grain-boundary grooving by surface diffusion. *Computational Materials Science*, 3, 3 (1995) 347-358. doi: 10.1016/0927-0256(94)00073-L.
- Khenner M, Averbuch A, Israeli M, Nathan M, Glickman EE. Level set modeling of transient electromigration grooving. *Computational Materials Science*, 20,2 (2001) 235-250. doi: 10.1016/S0927-0256(00)00179-8.
- Hackney SA, Ojard G. Grain boundary grooving at finite grain size. *Scripta Metallurgica*, 22,11 (1988) 1731-1735. doi: 10.1016/S0036-9748(88)80274-6.
- Khenner M. Numerical simulation of grain-boundary grooving by level set method. *Journal of Computational Physics*, 170, 2 (2001) 764-784. doi: 10.1006/jcph.2001.6760.
- Srolovitz DJ, Safran SA. Capillary instabilities in thin films. I. Energetics. *Journal of Applied Physics*, 60, 1 (1986) 247. doi: 10.1063/1.337689.
- Huang P, Li Z, Sun J. Finite element analysis for surface

- diffusion-controlled shape instabilities of plate-like grains. *Computational Materials Science*, 20,1 (2001) 66–76. doi: 10.1016/S0927-0256(00)00126-9.
17. Ogurtani TO, Akyildiz O. Grain boundary grooving and cathode voiding in bamboo-like metallic interconnects by surface drift diffusion under the capillary and electromigration forces. *Journal of Applied Physics*, 97, 9 (2005) 093520. doi: 10.1063/1.1883305.
 18. Shenoy VB, Freund LB. A continuum description of the energetics and evolution of stepped surfaces in strained nanostructures. *Journal of the Mechanics and Physics of Solids*, 50, 9 (2002) 1817–1841. doi: 10.1016/S0022-5096(02)00015-7.
 19. Jeong H, Williams, ED. Steps on surfaces: experiment and theory. *Surface Science Reports*, 34, 6–8 (1999) 171–294. doi: 10.1016/S0167-5729(98)00010-7.
 20. Mykura H. The variation of the surface tension of nickel with crystallographic orientation. *Acta Metallurgica*, 9, 6 (1961) 570–576. doi: 10.1016/0001-6160(61)90160-2.
 21. Bonzel HP, Mullins WW. Smoothing of perturbed vicinal surfaces. *Surface Science*, 350,1–3 (1996) 285–300. doi: 10.1016/0039-6028(95)01111-0.
 22. Rabkin E, Klinger L, Semenov VN. Grain boundary grooving at the singular surfaces. *Acta Materialia*, 48, 7 (2000) 1533–1540. doi: 10.1016/S1359-6454(99)00432-2.
 23. Klinger LM, Rabkin E. The effect of stress on grain boundary interdiffusion in a semi-infinite bicrystal. *Acta Materialia*, 55, 14 (2007) 4689–4698. doi: 10.1016/j.actamat.2007.04.039.
 24. Rabkin E, Klinger L. The fascination of grain boundary grooves. *Advanced Engineering Materials*, 3, 5 (2001) 277–282. doi: 10.1002/1527-2648(200105)3:5<3.0.CO;2-G.
 25. Zhang W, Sachenko PP, Schneibel JH. Kinetics of thermal grain boundary grooving for changing dihedral angles. *Journal of Materials Research*, 17, 6 (2002) 1495–1501. doi: 10.1557/JMR.2002.0222.
 26. Akyildiz O, Oren EE, Ogurtani TO. Mesoscopic nonequilibrium thermodynamics treatment of the grain boundary thermal grooving induced by the anisotropic surface drift diffusion, *J. Mater. Sci.*, 46, 18 (2011) 6054–6064.
 27. Zhang W, Sachenko PP, Gladwell I. Thermal grain boundary grooving with anisotropic surface free energies. *Acta Materialia*, 52, 1 (2004) 107–116. doi: 10.1016/j.actamat.2003.08.033.
 28. Xin T, Wong H. A γ -function model of facets. *Surface Science*, 487, 1–3 (2001) L529–L533. doi: 10.1016/S0039-6028(01)01158-X.
 27. Xin T, Wong H. Grain-boundary grooving by surface diffusion with strong surface energy anisotropy. *Acta Materialia*, 51, 8 (2003) 2305–2317. doi: 10.1016/S1359-6454(03)00039-9.
 30. Xin T, Wong H. A spike-function model of facets. *Materials Science and Engineering A*, 364, 1–2 (2004) 287–295. doi: 10.1016/j.msea.2003.08.042.
 31. Min D, Wong H. Grain-boundary grooving by surface diffusion with asymmetric and strongly anisotropic surface energies. *Journal of Applied Physics*, 99, 2 (2006a) 023515. doi: 10.1063/1.2159082.
 32. Du P, Wong H. A delta-function model for axially symmetric crystals. *Scripta Materialia*, 55,12 (2006) 1171–1174. doi: 10.1016/j.scriptamat.2006.07.042.
 33. Ogurtani, T. O. Dirichlet extremum problem associated with the asymmetric grain-boundary thermal grooving under the Dirac γ -type anisotropic surface stiffness in bicrystal thin solid films. *Journal of Applied Physics*, 102, 6 (2007) 063517. doi: 10.1063/1.2781574.
 34. Ramasubramaniam A, Shenoy VB. On the evolution of faceted grain-boundary grooves by surface diffusion. *Acta Materialia*, 53 (2005) 2943–2956. doi: 10.1016/j.actamat.2005.03.013.
 35. Ogurtani TO. Variational formulation of irreversible thermodynamics of surfaces and interfaces with grain-boundary triple-junction singularities under the capillary and electromigration forces in anisotropic two-dimensional space. *Physical Review B*, 73, 23 (2006a) 1–17. doi: 10.1103/PhysRevB.73.235408.
 36. Verschaffelt JE. The thermomechanics of the superficial layer. I. Generalities; pure substances. *Bulletins de l'Academie Royale des Sciences, des Lettres et des Beaux Arts de Belgique*, 22 (1936) 373.
 37. Guggenheim EA. *Thermodynamics* (3 ed., p. 46). North-Holland, Amsterdam, Holland, 1959.
 38. Ogurtani TO, Akyildiz O, Oren EE. Morphological evolution of tilted grain-boundary thermal grooving by surface diffusion in bicrystal thin solid films having strong anisotropic surface Gibbs free energies. *Journal of Applied Physics*, 104, 1 (2008) 013518. doi: 10.1063/1.2952520.
 39. Ogurtani TO. Thermal grain-boundary grooving in bicrystal thin solid films having strong anisotropic surface Gibbs free energy represented by the modified cycloid-curtate function. *Journal of Crystal Growth*, 311, 6 (2009a) 1584–1593. doi: 10.1016/j.jcrysgro.2009.01.084.
 40. Sharma SK, Spitz J. Thermal grooving in thin silver films. *Journal of Materials Science*, 16, 2 (1981) 535–536. doi: 10.1007/BF00738649.
 41. Tsoga A, Nikolopoulos P. Groove angles and surface mass transport in polycrystalline alumina. *Journal of the American Ceramic Society*, 77, 4 (1994) 954–960. doi: 10.1111/j.1151-2916.1994.tb07252.x
 42. Tritscher P, Broadbridge P. Grain boundary grooving by surface diffusion: an analytic nonlinear model for a symmetric groove. *Proceedings of the Royal Society: Mathematical and Physical Sciences (1990–1995)*, 450, 1940 (1995) 569–587. doi: 10.1098/rspa.1995.0101.
 43. Schöllhammer J, Chang L, Rabkin E, Baretzky B, Gust W, Mittemeijer E. Measurement of the profile and the dihedral angle of grain boundary grooves by atomic force microscopy. *Zeitschrift für Metallkunde*, 90 (1999) 687–690.
 44. Shin W, Seo W, Koumoto K. Grain-boundary grooves and surface diffusion in polycrystalline alumina measured by atomic force microscope. *Journal of the European Ceramic Society*, 18, 6 (1998) 595–600. doi: 10.1016/S0955-2219(97)00207-0.
 45. Lee KY, Case ED. A comparison of theoretical and experimental profiles for thermally-induced grain-boundary grooving. *The European Physical Journal Applied Physics*, 8, 3 (1999) 197–214. doi: 10.1051/epjap:1999247.
 46. Rabkin E, Gabelev A, Klinger L, Semenov VN, Bozhko SI. Grain boundary grooving in molybdenum bicrystals. *Journal of Materials Science*, 41, 16 (2006) 5151–5160. doi: 10.1007/s10853-006-0438-4.
 47. Sachenko PP, Schneibel JH, Zhang W. Effect of faceting on the thermal grain-boundary grooving of tungsten.

- Philosophical Magazine A, 82, 4 (2002) 815–829. doi: 10.1080/01418610208243204.
48. Sachenko PP, Schneibel JH, Zhang W. Observations of secondary oscillations in thermal grain boundary grooves. *Scripta Materialia*, 50, 9 (2004) 1253–1257. doi: 10.1016/j.scriptamat.2004.01.030.
49. Sachenko PP, Schneibel JH, Swadener JG, Zhang W. Experimental and simulated grain boundary groove profiles in tungsten. *Philosophical Magazine Letters*, 80, 9 (2000) 627–631. doi: 10.1080/09500830050134345.
50. Munoz NE, Gilliss SR, Carter CB. The monitoring of grain–boundary grooves in alumina. *Philosophical Magazine Letters*, 84, 1 (2003) 21–26. doi: 10.1080/09500830310001614487.
51. Ogurtani TO, Oren EE. Irreversible thermodynamics of triple junctions during the intergranular void motion under the electromigration forces. *International Journal of Solids and Structures*, 42, 13 (2005) 3918–3952. doi: 10.1016/j.ijsolstr.2004.11.013.
52. Ogurtani TO. Mesoscopic nonequilibrium thermodynamics of solid surfaces and interfaces with triple junction singularities under the capillary and electromigration forces in anisotropic three–dimensional space. *The Journal of chemical physics*, 124, 14 (2006b) 144706. doi: 10.1063/1.2185625.

Effect of Inulin and *Auricularia polytricha* Extract on Proliferation of *Lactobacillus rhamnosus*

Gülçin Alp Avcı¹, Burçin Özçelik² and Ceren Kesepera²

¹ Hitit University, Department of Molecular Biology and Genetics, Çorum, TURKEY

² Hitit University, Department of Biology, Çorum TURKEY

ABSTRACT

Probiotic microorganisms have many health-beneficial effects on gastrointestinal system and their therapeutic usage is becoming increasingly common in human and veterinary medicine. Many different species and strains of bacteria, yeast and even fungi have been extensively used as potential probiotics. Among the probiotic strains, *Lactobacillus rhamnosus* is one of the most commonly used strain for probiotic treatment and health promoting functions of this strain are well documented. To enhance therapeutic effects of probiotics, prebiotics have been extensively used. Prebiotics stimulate the proliferation of probiotics and this may have positive effects on the maintenance of the balance between pathogenic and nonpathogenic bacteria. In this study, we aimed to evaluate the effect of inulin and *Auricularia polytricha* aqueous extract on the proliferation of *L. rhamnosus*. For this purpose, *L. rhamnosus* was inoculated in three different MRS broth supplemented with inulin 5%, *A. polytricha* extract 5% and with the mixture of inulin 5% plus *A. polytricha* extract 5%. Our results indicated that *L. rhamnosus* was able to use inulin and fungus extract as a carbon source. Moreover, combined use of inulin and *A. polytricha* improved prebiotic efficacy.

Article History:

Received: 2016/11/01

Accepted: 2016/12/28

Online: 2017/06/30

Correspondence to: Burcin Ozcelik,
Hitit University, Faculty of Science and Arts,
Department of Biology, Çorum, TURKEY
Tel: +90 (364) 227-7000-1715
Fax: +90 (364) 227-7005
E-Mail: burcinozcelik@hitit.edu.tr

Keywords:

Lactobacillus rhamnosus; Probiotic; Prebiotic; Inulin; *Auricularia polytricha*.

INTRODUCTION

According to World Health Organization (WHO), the scientific definition of probiotics is “viable microorganisms that, when administered in adequate amount (10⁶ to 10⁷ cfu/g) to the human host confer health benefits” [1, 2]. Most important health-beneficial effect of probiotics is the regulation of the intestinal microbiota. The effect of a probiotic microorganism on the microecology of the intestine is not only modulation of intestinal microbiota, but also protection against infectious microorganisms. There has been encouraging scientific evidences that probiotic microorganisms may help to treat irritable bowel syndrome, fungal and bacterial infections, diarrhea, especially following treatment with certain antibiotics, to prevent colds and flu, cardiovascular diseases and several types of cancer, to reduce of serum cholesterol levels and to modulate systemic immunity in animals and humans [3-6]. Because of these health-beneficial effects, therapeutic usage of probiotics is becoming increasingly common in human and veterinary medicine.

Nowadays, many different species and strains of bacteria, yeast and even fungi have been extensively used as potential probiotics. Typically strains of lactic acid bacteria, including lactobacilli, have been considered as the predominant microbial probiotic group having therapeutic benefits. Among the probiotic strains of lactic acid bacteria, *Lactobacillus rhamnosus* is one of the most commonly used strain for probiotic treatment and health promoting functions of this strain are well documented. *L. rhamnosus* is a facultatively heterofermentative rod-shaped bacterium and is frequently found in gastrointestinal tract of healthy individuals [7-10].

Prebiotics stimulate the proliferation of probiotics and this may have positive effects on the maintenance of the balance between pathogenic and nonpathogenic bacteria. Inulin, lactulose, fructo and galactooligosaccharides are widely used prebiotics. Among these, inulin is shown to exert a protective effect on lactic acid bacteria by stimulating their survival and

activity. And also, mushrooms with the rich β -glucan and oligo- β -glucan ingredients may be the potential sources for prebiotics. *Aucularia polytrichia* is known for its nutritional ingredients and it has many beneficial effects on human health. Its benefits include increasing blood circulation, lowering cholesterol and blood sugar, natural anti-viral properties, and thought to prevent dryness due to its moistening properties [11-13]. But properly use of prebiotics is important for stimulation of the probiotic proliferation. Therefore, in the present study, the effects of inulin and *A. polytricha* extract on the proliferation of *L. rhamnosus* which is a probiotic bacteria were evaluated.

MATERIALS AND METHODS

Bacterial strains and culture media

For the preparation of active cultures, *L. rhamnosus* strains were grown in Man Rogosa Sharpe (MRS) broth (Oxoid) for 18-20 h at 37 ± 1 °C. *Escherichia coli* (ATCC 25922), *Staphylococcus aureus* (ATCC 25923), *Enterococcus faecalis* (ATCC 29212), *Pseudomonas aeruginosa* (ATCC 27853), *Candida albicans* (ATCC 10231) were used as test microorganisms. Test microorganisms were obtained from culture collection at Hitit University, Faculty of Science and Arts, Department of Molecular Biology and Genetic, Microbiology Research Laboratory. *Lactobacillus rhamnosus* strain was obtained from Gazi University, Faculty of Dentistry, Division of Medical Microbiology. The bacterial strains were stored at -80 °C in Nutrient broth containing 10% glycerol as cryoprotective agent.

Antimicrobial activity of *L. rhamnosus*

The antifungal and antibacterial activities of *L. rhamnosus* were evaluated by well diffusion method on Mueller-Hinton Agar (MHA). Briefly, MHA plates were inoculated with bacterial strains (100 μ l) that were activated two times and optically standardized (OD₆₀₀=0.6 \bar{A}). Then wells were composed 6mm diameter on MHA and wells were filled with 10 or 15 μ l of *L. rhamnosus* suspension in MRS broth and incubated

at 37°C for 16-18 hours. After the incubation period, all petri dishes were investigated by zone inhibition for their antimicrobial activity.

Preparation of fungi extract

A commercially cultivated strain of *Auricularia polytricha* was purchased from Agroma Food (Turkey). To prepare the extract of *A. polytricha*, distilled water was used and 20 g sample weighted for extraction. Extraction was made with soxhlet machine during 8-12 hours. After extraction, solvent was concentrated in rotary vacuum evaporator machine (Stuart Rotary Evaporator, RE300P). The extract was then membrane filtered (0.45- μ m pore size) to avoid contamination in works. Extracts were protected from light and kept in +4°C until executing the experiments.

Evaluation of prebiotic effect of inulin and *A. polytricha* extract

Inulin, *A. polytricha* aqueous extract and a mixture of inulin and the extract were used as prebiotic to improve the proliferation of *L. rhamnosus*. For this purpose, *L. rhamnosus* was activated two times in MRS broth and incubated 16-24 hours at 37°C. The bacterial suspension was adjusted to an optical density at 600 nm (OD₆₀₀) of 0.6 to standardize the cell density of the samples. Activated and optically standardized microorganisms were inoculated (2% v/v) in 5 ml of MRS and culture medium containing different types of prebiotics. Table 1 shows the composition of these mediums. Prebiotics were added to MRS broth instead of glucose. Fermentations were carried out at 37°C independently, in duplicate, without any agitation. At the end of the incubation time, bacterial cell concentration in modified MRS was determined spectrophotometrically at 600 nm.

Counts of viable bacteria

Cell counts were made by plating in duplicate after fermentation. Samples (1.0 mL) were added to 4.0 mL of MRS broth and serial dilutions were made. After from

Table 1. Composition of MRS broth and medium containing prebiotics.

Components (g/L)	MRS broth	MRS + inulin	MRS+ Fungus extract	MRS+ inulin+ Fungus extract
Pepton (g/L)	10	10	10	10
Yeast extract (g/L)	5	5	5	5
Meat extract (g/L)	10	10	10	10
Glucose (g/L)	20	-	-	-
Potassium phosphate dibasic (g/L)	2	2	2	2
Sodium acetate.3H ₂ O (g/L)	5	5	5	5
Triamonium citrate (g/L)	2	2	2	2
Manganese sulfate. H ₂ O (g/L)	0.05	0.05	0.05	0.05
Magnesium sulfate.7H ₂ O (g/L)	0.1	0.1	0.1	0.1
Tween80 (mL/L)	1	1	1	1
Inulin	-	5%	-	5%
<i>A. polytricha</i>	-	-	5%	5%

dilutions, *L. rhamnosus* was inoculated on MRS Agar, with pH adjusted to 6.8, and incubated at 37 °C for 16-18 h.. Then, colony forming units (CFU) were enumerated in plates containing colonies, and cell concentration was expressed as CFU/ml.

Statistical analysis

The all experiments were done in duplicate. The results were expressed as means \pm standard deviations (SD). Statistical analysis was performed on the data by SPSS 20.0 bivariate Correlation Analysis (SPSS Inc., Chicago) with statistical significance determined at 0.05.

RESULTS AND DISCUSSION

Antimicrobial activity of *L. rhamnosus*

Previous studies provided evidence that *Lactobacillus* species had inhibitory effect on pathogenic microorganisms [14]. In this study, *L. rhamnosus* was examined for antimicrobial activity against pathogenic microorganisms *Escherichia coli*, *Staphylococcus aureus*, *Pseudomonas aeruginosa*, *Enterococcus faecalis* and *Candida albicans*. In our study, no antimicrobial effect of *L. rhamnosus* was detected on tested pathogens. Davoodabadi et al. [15] tested *Lactobacillus* strains with human origin for their antimicrobial activity against diarrheagenic *Escherichia coli*. A total of 20 *Lactobacillus* isolates were identified from stool samples. *Lactobacillus fermentum* was the most frequently isolated strain, followed by *L. plantarum* and *L. rhamnosus*. The findings showed that *Lactobacillus* strains with human origin had a mild inhibitory activity against the diarrheagenic *E. coli*. It was mentioned that the mechanism of antimicrobial activity of *Lactobacillus* strains appeared to be due to the production of organic acids or hydrogen peroxide. In another study, antimicrobial activity and antibiotic susceptibility were tested for 23 *Lactobacillus* and three *Bifidobacterium* strains. Agar-well diffusion method was used to test the antagonistic effect against *Staphylococcus aureus*, *E. coli*, *Bacillus cereus* and *C. albicans* of acid and neutralized lyophilized concentrated supernatants. Inhibition of two pathogens with neutralized *L. bulgaricus*, *L. helveticus*, *L. plantarum*, *L. fermentum* was detected. Some strains maintained activity after pH neutralization, indicating presence of active substances [16].

Evaluation of prebiotic properties of inulin and *A. polytricha* aqueous extract

Prebiotics such as oligosaccharides and inulin promote the development of probiotic microorganisms. Nowadays, some macrofungus are presumed to be prebiotic like inulin and various studies are being carried out [17]. In our study, we compare *Lactobacillus rhamnosus* growth in MRS broth and MRS supplemented with inulin and

Auricularia polytricha aqueous extract. Growth activity of *L. rhamnosus* in MRS broth and in medium containing prebiotics resulted in different growth profile. Figure 1 shows the data for growth rate of *L. rhamnosus* in the medium with and without glucose. It was observed that the development of *L. rhamnosus* in glucose-containing MRS medium was fairly good (OD600nm = 1.972A), while the removal of glucose resulted in a somewhat weaker development. The addition of inulin as prebiotic instead of glucose led to the continue development of *L. rhamnosus* (OD600nm=1.058 A). The prebiotic effect of *A. polytricha*, which is a macrofungus, was found to be weaker when compared to inulin (OD600nm=1.032 A). When the concurrent effect of inulin and fungus is examined, inulin was found that the effect was slightly higher than the fungus alone (OD600nm=1.046 A). However, no statistical difference was observed ($p>0.05$). Kaplan et al. [18] studied the effect of inulin on the growth profile of sixteen *Lactobacillus* strains. It was established that twelve of these strains were able to ferment inulin. In another study, a significant increase in lactobacilli levels in colon rats was observed when the culture medium was supplemented with inulin [19]. This is the first study, to our knowledge, to test the prebiotic effect of *A. polytricha* aqueous extract. Synytsya et al. tested the prebiotic effect of aqueous and alkali extracts of two cultivated mushrooms that belong to same class with *A. polytricha*. The difference between the values of maximum growth rate and maximum biomass concentration measured for the medium without and with the extract was compared for the extracts of *Pleurotus ostreatus* and *Pleurotus eryngii*. In most cases the extracts from *P. ostreatus* and *P. eryngii* support probiotic bacteria growth rate and biomass *Lactobacillus* strains. Extracts from *P. eryngii* proved better growth source than those from *P. ostreatus*. *Lactobacillus* strain Lac A grew with the same rate as control as with water extract of *P. eryngii*, but alkaline extract increased this rate twice [20].

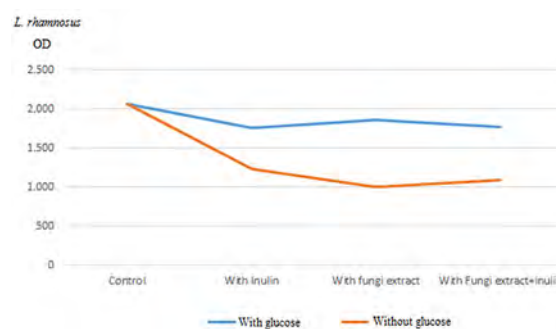


Figure 1. Proliferation of *L. rhamnosus* with effect of inulin and *A. polytricha* extract

Counts of viable cells

Viability of *L. rhamnosus* was calculated as colony-forming units. As shown in Figure 2, *L. rhamnosus* viability determined 1.87×10^4 cfu/ml in control medium, 2.08×10^4 cfu/ml with inulin, 1.92×10^4 cfu/ml with *A. polytricha* and 2.22×10^4 with inulin plus *A. polytricha*. These results point out a generalized stimulation of the proliferation of *L. rhamnosus* induced by prebiotics. The influence of inulin on probiotic survival is consistent with the observations of several authors, who observed a clear beneficial action of this prebiotic on the viability of *L. rhamnosus* [21, 22]. Oliveira et al. [23] observed significant difference for viable counts of *L. rhamnosus*, which was strongly influenced by the inulin. The mean probiotic viable counts were 4.1% higher than in the control in the presence inulin. Although there is some information on the effect of *A. polytricha* on the intestinal flora in the literature, there is no definite study relation with the prebiotic effect of its.

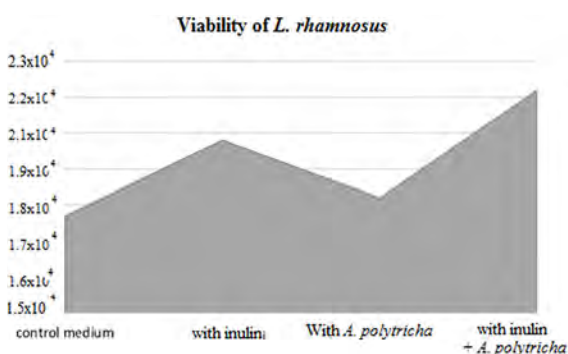


Figure 2. Viability of *L. rhamnosus*

CONCLUSION

Probiotics are effective in the prevention and treatment of numerous diseases such as irritable bowel syndrome, cancer, urinary infections. *Lactobacillus rhamnosus* is one of the most used probiotic. To enhance their proliferation and therapeutic effects, substrate like inulin are widely used as a prebiotics. The prebiotic effects of inulin and several mushrooms have been confirmed in some clinical researches. In this research, we evaluated the effect of inulin and *Auricularia polytricha* extract on the growth profile of *L. rhamnosus*. Our results indicated that *L. rhamnosus* could use inulin and *A. polytricha* extract as a carbon source. Further studies on health benefit in animal models will be also conducted.

ACKNOWLEDGMENTS

We would like to thank Dr. Gülçin Akça at Gazi University, Faculty of Dentistry, Division of Medical Microbiology, Ankara, Turkey for *Lactobacillus rhamnosus* strain.

REFERENCES

1. Ashraf R, Shah NP. Selective and differential enumerations of *Lactobacillus delbrueckii* subsp. *bulgaricus*, *Streptococcus thermophilus*, *Lactobacillus acidophilus*, *Lactobacillus casei* and *Bifidobacterium* spp. in yoghurt. *International Journal of Food Microbiology* 149 (2011) 194-208.
2. Soukoulisa C, Behboudi-Jobbehndara S, Yonekuraa L, Parmenterb C, Fiska ID. Stability of *Lactobacillus rhamnosus* GG in prebiotic edible films. *Food Chemistry* 159 (2014) 302-308.
3. Zubillaga M, Ricardo W, Eric P, Cinthia G, Ricardo C, José B. Effect of probiotics and functional foods and their use in different diseases. *Nutrition Research* 21 (2001) 569-579.
4. Quigley EM. Gut microbiota and the role of probiotics in therapy. *Current Opinion Pharmacology*. 11 (2011) 593-603.
5. Geier MS, Butler RN, Howarth GS. Probiotics, prebiotics and synbiotics: a role in chemoprevention for colorectal cancer. *Cancer Biology Therapy* 5 (2006) 1265- 1269.
6. Hickson M, D'Souza AL, Muthu N, Rogers TR, Want S, Rajkumar C. Use of probiotic *Lactobacillus* preparation to prevent diarrhoea associated with antibiotics: Randomized double blind placebo controlled trial. *BMJ* 33 (2007) 80-83.
7. Collado M, Meriluoto J, Salminen S. Role of commercial probiotic strains against human pathogen adhesion to intestinal mucus. *Letters Applied Microbiology* 45 (2007) 454-460.
8. Lavasani S, Dzhambazov B, Nouri M, Fak F, Buske S, Molin G. A novel probiotic mixture exerts a therapeutic effect on experimental autoimmune encephalomyelitis mediated by IL-10 producing regulatory T cells. *PLoS One* 5 (2010) 1-11.
9. DeGroote MA, Frank DN, Dowell E, Glode MP, Pace NR. *Lactobacillus rhamnosus* GG bacteremia associated with probiotic use in a child with short gut syndrome. *Pediatric Infectious Disease Journal* 24 (2005) 278-280.
10. Näse L, Hatakka K, Savilahti E, Saxelin M, Pönkä A, Poussa T, Korpela R, Meurman JH. Effect of long-term consumption of a probiotic bacterium, *Lactobacillus rhamnosus* GG, in milk on dental caries and caries risk in children. *Caries Research* 35 (2001) 412-420.
11. Dunne C, O'Mahoney L, Murphy L. In vitro selection criteria for probiotic bacteria of human origin: correlation with in vivo findings. *American Journal Clinical Nutrition* 73 (2001) 386-392.
12. Tannock G. Methodologies for quantification of faecal bacteria: application to prebiotic effects. *British Journal of Nutrition* 87 (2002) 199-201.
13. Kues U, Liu Y. Fruiting body production in basidiomycetes. *Application Microbiology and Biotechnology* 54 (2000) 141-152.
14. Tuohy KM, Rouzaud GCM, Bruck WM, Gibson GR. Modulation of the human gut microflora towards improved health using prebiotics-assessment of efficacy. *Current Pharmaceutical Design* 11 (2005) 75-90.
15. Davoodabadi A, Dallal MMS, Lashani E, Ebrahimi MT. Antimicrobial activity of *Lactobacillus* spp. isolated from fecal flora of healthy breast-fed infants against diarrheagenic *Escherichia coli*. *Jundishapur Journal of Microbiology* 8 (2015) 1-6.
16. Georgieva R, Yochevab L, Tserovskab L, Zhelezovab G, Stefanovaa N, Atanasovaa A, Dangulevaa A, Ivanovaa G,

- Karapetkova N, Romyana N, Karaivanovaa E. Antimicrobial activity and antibiotic susceptibility of *Lactobacillus* and *Bifidobacterium* spp. intended for use as starter and probiotic cultures. *Biotechnology and Biotechnological Equipment* 29 (2015) 84–91.
17. Videla S. Deranged luminal pH homeostasis in experimental colitis can be restored by a prebiotic. *Gastroenterology* 116 (1999).
 18. Kaplan H, Hutkins RW. Fermentation of fructooligosaccharides by lactic acid bacteria and bifidobacteria. *Applied and Environmental Microbiology* 66 (2000) 2682-2684.
 19. Kolida S, Tuohy K, Gibson GR. Prebiotic effects of inulin and oligofructose. *British Journal of Nutrition* 87 (2002) 193-197.
 20. Synytsya A, Mickova K, Synytsya A, Jablonsky I, Spevacek J, Erban V, Kovarikova E, Copikova J. Glucans from fruit bodies of cultivated mushrooms *Pleurotus ostreatus* and *Pleurotus eryngii*: Structure and potential prebiotic activity. *Carbohydrate Polymers* 76 (2009) 548-556.
 21. Oliveira RPS, Perego P, Converti A, Oliveira MN. Growth and acidification performance of probiotics in pure culture and co-culture with *Streptococcus thermophilus*: The effect of inulin. *Food Science Technology* 42 (2009) 1015– 1021.
 22. Paseephol T, Sherkat F. Probiotic stability of yoghurts containing Jerusalem artichoke inulins during refrigerated storage. *Journal of Functional Foods* 1 (2009) 311–318.
 23. Oliveira RPS, Casazza AA, Aliakbarian B, Perego P, Converti A, Oliveira MN. Influence of fructooligosaccharides on the fermentation profile and viable counts in a symbiotic low fat milk. *Brazilian Journal of Microbiology* 44 (2013) 431–434.

Theoretical Performance Analysis of an R1234yf Refrigeration Cycle Based on the Effectiveness of Internal Heat Exchanger

Mehmet Direk, Alper Keleşoğlu, Ahmet Akın

Department of Energy Systems Engineering, University of Yalova, Yalova, TURKEY

ABSTRACT

In this paper, the effects of internal heat exchanger (IHx) effectiveness on the performance parameters of the refrigeration cycle with R1234yf were theoretically investigated. For this purpose, a mathematical model was developed based on the energy balance of the cycle. The analysis were performed between -20°C and 0°C evaporation and 40°C and 50°C condensation temperatures based on the effectiveness value of IHx. The cooling capacity, coefficient of performance (COP), subcooling, superheat and compressor discharge temperature of the refrigeration cycle was examined. Finally, the performance results of the cycle with R1234yf were compared with the baseline cycle that utilizes with R134a. As a result, it was determined that the critical effectiveness to supply the same COP with R1234yf was determined 50% in comparison the baseline cycle.

Keywords:

R1234yf; R134a; Internal heat exchanger; Effectiveness.

INTRODUCTION

According to European Commission (EC) Regulation No 517/2014, Directive No 40/2006 was rearranged so that usage of refrigerants that have GWP value higher than 150 is prohibited in mobile air conditioning systems by 2022 [1, 2]. Thus, finding a new alternative refrigerant to R134a (GWP=1430) has become a necessity and recent studies mainly have been focusing on this topic [3]. Refrigerants such as R152a, R1234yf, R1234ze and R744 (CO_2) were suggested in the literature as environment friendly refrigerants [4, 5, 6, 7]. As an alternative refrigerant, R1234yf (GWP=4) has attracted great attention due to its similar thermophysical properties in comparison with R134a [7, 8]. Therefore, various theoretical and experimental comparison studies about R1234yf can be found in the literature. Among them; Naushad et al. theoretically investigated R1234ze and R1234yf as alternatives to R134a in simple vapour compression refrigeration system. They claimed that R1234yf can be a good alternative to R134a after made some necessary modifications, such as selecting suitable compressor oil and pipe sizes. On the other hand, their study showed that R1234ze requires bigger

compressor displacement volume to supply same cooling capacity [9]. Hoşöz et al. experimentally evaluated the automotive air conditioning (AAC) system with R1234yf as a function of different ambient temperatures. Their results showed that the cooling capacity and COP of R1234yf were lower between 3.50-6.99% and 5.98-21.42% than R134a. [10]. Zilio et al. experimentally and numerically investigated R1234yf in AAC system that was originally designed to work with R134a by making simple modifications. They found that the cooling capacity and COP of R1234yf were quite lower than R134a for the same system. However, their numerical simulations showed that at the same cooling capacities, the system with R1234yf would have higher COP by enhancing the effective areas of the condenser and evaporator by 20% and 10%, respectively [11]. Daviran et al. developed a simulation program to evaluate the performance comparison of the AAC system that works with R1234yf and R134a. They observed that the COP of the system with R1234yf was 18% higher than R134a in case of constant mass flow rate and lower for the equal cooling capacity by 1.3-5% [12]. Qi investigated the potentials

Article History:

Received: 2016/12/02

Accepted: 2017/02/13

Online: 2017/06/30

Correspondence to: Mehmet Direk,
Department of Energy Systems
Engineering, University of Yalova, Yalova,
TURKEY
E-Mail: mehmetdirek@hotmail.com

to improve the system performance parameters for the operation of an AAC system using R1234yf. He found that the cooling capacity and COP values of the system was increased up to 15% by changing the subcooling degree from 1K to 10K in the condenser. Moreover, he claimed that the cooling capacity of the system can increase 72.8% by increasing the compressor volumetric efficiency from 55 to 95% [13]. Navarro et al. experimentally studied with R1234yf as a drop-in alternative for R134a in vapour compression refrigeration system. They determined that the COP of R1234yf was 5 to 30% lower than R134a. In addition, when the condensation temperature increased from 313.15 to 333.15 K, they obtained that the COP difference between R1234yf and R134a decreased up to 8%. They concluded that the IHX would cause even more reduction in the COP difference [14]. Babiloni et al. investigated the performance of an air conditioning system using R134a, R1234yf and R1234ze. The results were presented as a function of various evaporator and condenser temperatures for three refrigerants. They determined that R1234yf and R1234ze were showed lower cooling capacity values compared to R134a by 9% and 30%, respectively. Additionally, they claimed that the cooling capacity values were diminished against the increased condensation temperature. They concluded that the cooling capacity and COP of the system with R1234yf would tend to increase by adding IHX at 30% effectiveness [15]. Domanski et al. determined the influence of the liquid line/suction line heat exchanger to the refrigeration system. According to the refrigerant properties and operating conditions, they obtained that the liquid line/suction line heat exchanger can be enhanced the system performance parameters [16]. Aprea et al. demonstrated the consequences of the adapting IHX to the refrigeration system. They expressed that preventing flash gas formation at the inlet of expansion valve and liquid contained vapour which enters to compressor are the benefits of IHX [17]. Klein et al. investigated the influence of IHX on the performance of a refrigeration system for a number of alternative refrigerants. They found that when IHX adapted to the system the mass flow rate of the system was decreased due to decreasing suction density. Additionally, they implied that for some refrigerants the cooling effect was increased with increasing subcooling degree supplied with IHX [18]. Mastrullo et al. conducted experiments to show the performance of 19 ozone friendly refrigerants. They implied that installation of IHX can have positive or negative effect regarding to the refrigerant fluids. Their results showed that the IHX had the same influence on the COP and refrigerating volumetric capacity [19]. Moles et al. performed theoretical comparison analysis with R1234yf and R1234ze in different single stage vapour compression refrigeration system configurations. They obtained the best performance for the system with IHX

when ejector or expander used as an expansion device. They claimed that using IHX with effectiveness over 45% significantly enhanced the COP of the system. Consequently, they determined the relative difference between R1234yf and R134a in COP and cooling capacity were lower for R1234yf by 4-8% and 4-7%, respectively [20]. Cho et al. conducted experiments to perform the energy and exergy analysis of the AAC system with and without using IHX. They determined that COP of the system with R1234yf was 3.6 to 4.5% lower than R134a. Additionally, with presence of IHX, the COP of the system was found to be 0.3-2.9% lower for R1234yf at the compressor speed between 800-1800 rpm. Moreover, they observed that it was 0.9% higher at 2500 rpm. On the other hand, they indicated that the total exergy destruction rate was decreased by adapting IHX to the system with R1234yf [21]. Navarro et al. experimentally determined the effects of IHX in conventional vapour compression refrigeration system. They carried out 36 steady-state tests with various operating conditions and compared the results between R1234yf and R134a. They found that the relative cooling capacity and COP was reduced using IHX by 2% and 6%, respectively [22]. Pottker et al. demonstrated that the COP of the system with R1234yf was increased by increasing subcooling degree of the condensed liquid when IHX used in the system. They used 1.5 m aluminium concentric double pipe IHX with 35% effectiveness in their system. They observed that the COP of their system was improved by 16% due to increased subcooling degree with IHX [23]. Coating materials are made for increasing corrosion resistance of material, preventing discontinuity on metals (scratches, pores) and gaining functional quality [2]. In gears while coating, decreases surface roughness of gear, scoring resistance and corrosion resistance are increased.

In this study a more comprehensive performance analysis approach was followed based on variable effectiveness of IHX and operating conditions. For this purpose, a conventional refrigeration cycle was considered. The result were discussed under two different parts. In the first part, the variations of subcooling, superheat and the compressor discharge temperature of the cycle with R1234yf were examined based on effectiveness. In the second part, the influence of the effectiveness on the cycle performance parameters for R1234yf was compared with the baseline cycle that utilizes R134a. The cooling capacity and COP values

Table 1. Operating Conditions

Parameters	Value(s)	Range
Evaporation temperature (T_{evap})	-20-0 °C	5
Condensation temperature (T_{cond})	40-50 °C	2
Reference superheat	5 °C	Fixed
Reference subcooling	10 °C	Fixed
IHX effectiveness (ϵ_{ihx})	0-100%	25

were investigated as performance parameters of the refrigeration cycle. Finally, the relative performance parameters were compared under various evaporation and condensation temperatures.

MATERIALS AND METHODS

Description of the Cycle

As seen in Figure 1, the theoretical cycle consists of a compressor, condenser, evaporator, expansion valve and the IHX which is added between the evaporator and condenser outlets. Zero effectiveness represents the basic cycle and R1234yf follows the same cycle with R134a. On the other hand, in the mathematical model, the effectiveness values of IHX are considered only for R1234yf.

Thermodynamic Analysis

In order to determine the performance parameters, the mathematical model based on energy balance of the theoretical cycle were developed. For this purpose, the operating conditions represented in Table 1 were considered as basis of the calculations. The subcooling and superheat was used as constant values for the zero effectiveness. Therefore, these are selected as the reference values of the cycle. Additionally, the range of condensation and evaporation temperatures was selected according to the working conditions of real refrigeration system.

The following assumptions were made in order to carry out the calculations:

1. Steady-state operating conditions were assumed.
2. The changes in kinetic and potential energies are negligible.
3. The pressure losses within components and pipes are negligible.
4. Volumetric efficiency (η_v) of the compressor is 1.
5. Isentropic efficiency (η_{is}) of the compressor is 1.
6. Compressor, expansion valve and pipes are adiabatic.
7. Isenthalpic process is considered at the expansion valve.

The energy calculations are based on kJ per kg. Additionally, the formulas were utilized for the ideal vapour compression refrigeration cycle with IHX using the first law of thermodynamics.

The suction line temperature (T_1) can be expressed as;

$$T_1 = T_{evap} + T_{sh} \quad (1)$$

Where, T_{evap} , represents the evaporation temperature and T_{sh} is superheat.

The temperature at the condenser outlet (T_3) can be defined as;

$$T_3 = T_{cond} - T_{sc} \quad (2)$$

Where, T_{cond} represents the condensation temperature and T_{sc} is subcooling.

ΔT_{max} is the difference between condenser outlet temperature and evaporator outlet temperature:

$$\Delta T_{max} = T_3 - T_1 \quad (3)$$

The maximum heat flux (q_{max}) can be determined by Equation 3.

$$q_{max} = Cp_1 \Delta T_{max} \quad (4)$$

Where, Cp_1 is the specific heat at constant pressure for the suction line.

Accordingly, the heat flux of IHX (q_{IHX}) based on effectiveness, is calculated as follows;

$$q_{IHX} = \epsilon_{IHX} q_{max} \quad (5)$$

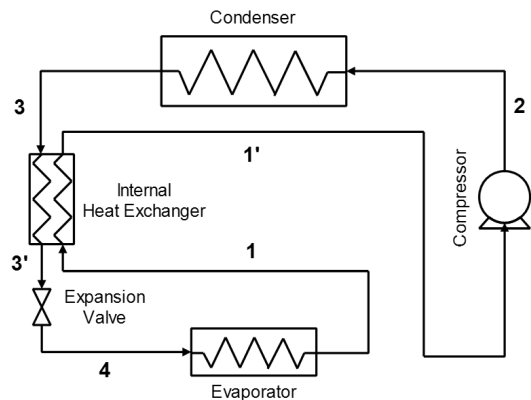


Figure 2. The changing of weight in the pinion to determine the critical scoring load

Where, ϵ is the effectiveness of IHX.

The refrigerant temperature at the IHX outlet for the evaporator side ($T_{1'}$) and for the condenser side ($T_{3'}$) can be calculated using Equations 6 and 7.

$$T_{1'} = (q_{IHX}/Cp_1) + T_1 \quad (6)$$

$$T_{3'} = T_3 - (q_{IHX}/Cp_3) \quad (7)$$

Where, Cp_3 is the specific heat at constant pressure for

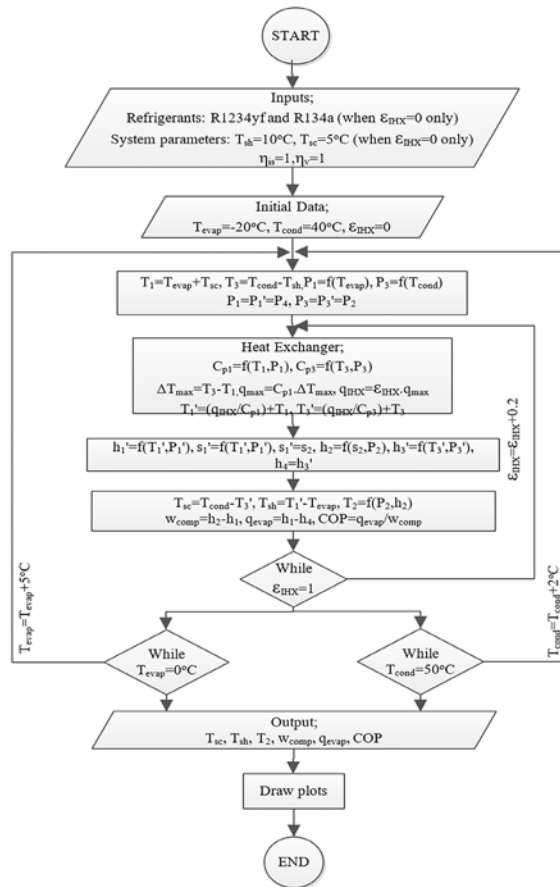


Figure 2. Flowchart for the refrigeration cycle

the subcooled refrigerant.

The compressor discharge temperature (T_2) and enthalpy value (h_2) were obtained by the isentropic compression process in the compressor. Additionally, the enthalpy value at the outlet of the expansion valve (h_4) was obtained by the isenthalpic process in the expansion valve.

The superheat and subcooling can be determined by Equations 8 and 9;

$$T_{sh} = T_{1'} - T_{evap} \tag{8}$$

$$T_{sc} = T_{cond} - T_{3'} \tag{9}$$

The cooling capacity (q_{evap}) can be expressed as;

$$q_{evap} = h_1 - h_4 \tag{10}$$

Compressor work can be calculated by Equation 11.

$$w_{comp} = h_2 - h_1 \tag{11}$$

COP can be expressed as;

$$COP = q_{evap} / w_{comp} \tag{12}$$

In order to compare the performance parameters of the cycles with R1234yf and R134a under various effectiveness values, the equations 13 and 14 was used;

$$COP\% = ((COP_{R1234yf} - COP_{R134a}) / COP_{R134a}) * 100 \tag{13}$$

$$q_{evap}\% = ((q_{evap,R1234yf} - q_{evap,R134a}) / q_{evap,R134a}) * 100 \tag{14}$$

The mathematical model was developed using Engineering Equation Solver (EES-V9.172-3D) and the enthalpy values were extracted from the EES database [24]. The program algorithm flowchart is shown in Figure 2.

RESULTS AND DISCUSSION

In the first part of this section, the variations of subcooling, superheat and the compressor discharge temperature of the cycle with R1234yf were investigated with respect to the effectiveness. In the second part, the influence of the effectiveness on the cycle performance parameters for R1234yf was compared with the baseline cycle that utilizes R134a. The changes in subcooling and superheat versus condensation temperature are shown in Figure 3a, b where the evaporation temperature is maintained

at -10°C . It is understood from the Figure 3a, that the subcooling increases with increasing effectiveness due to the raise in heat flux of the IHX against constant evaporation temperature. Additionally, the maximum

subcooling was obtained at the theoretical limits of the operating conditions where the condensation temperature and effectiveness were 50°C and 100%, respectively. On the other hand, superheat is increased

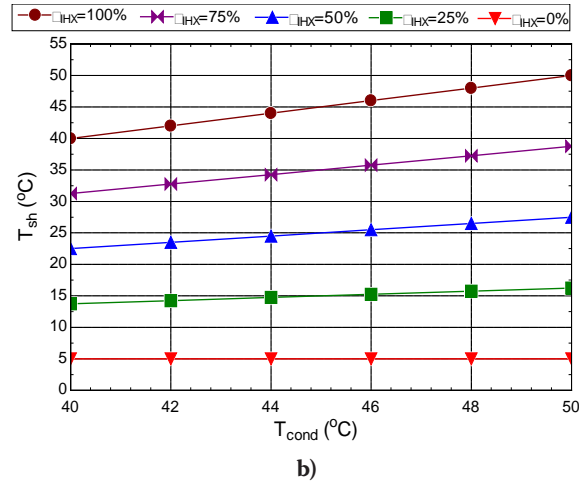
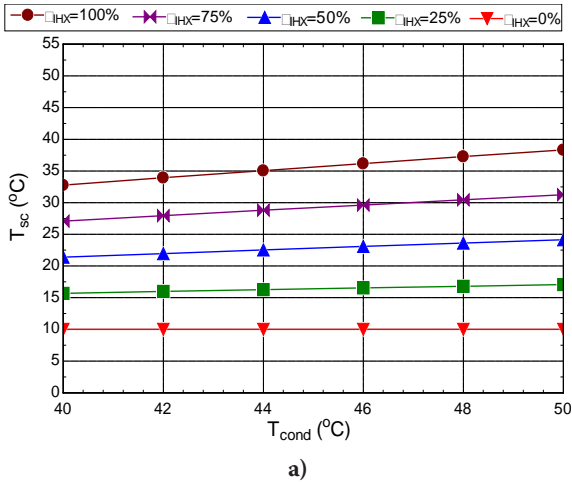


Figure 3. Variation of (a) Subcooling versus condensation temperature, (b) Superheat versus condensation temperature

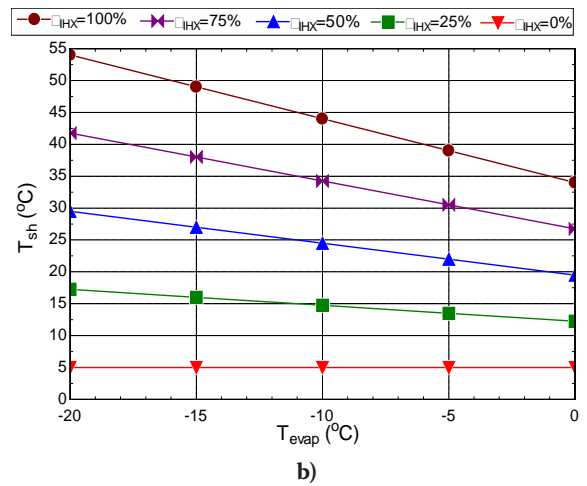
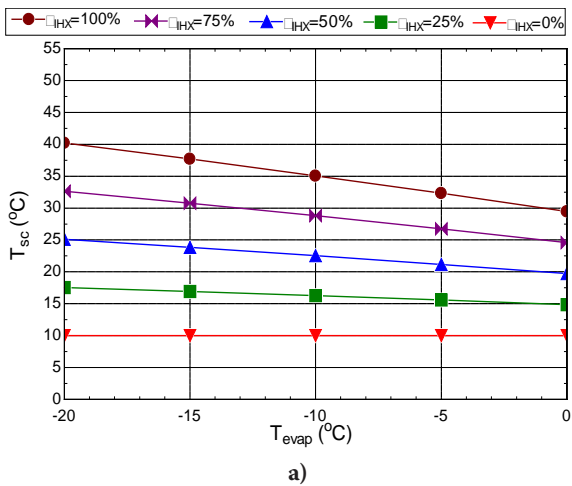


Figure 4. Variation of (a) Subcooling versus evaporation temperature, (b) Superheat versus evaporation temperature

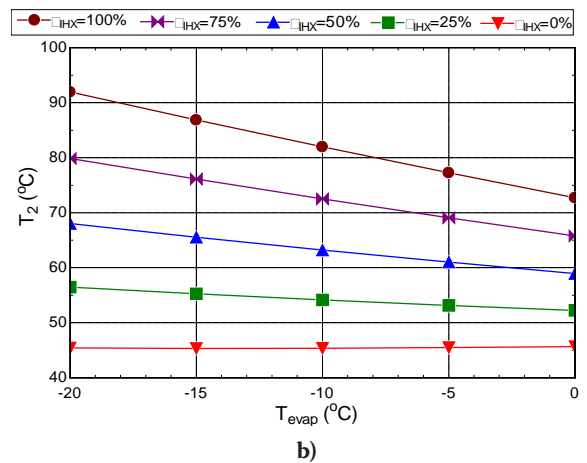
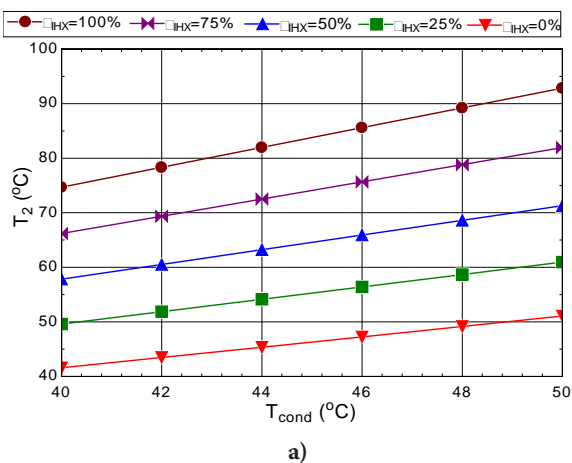


Figure 5. Variation of (a) with condensation temperature, (b) with evaporation temperature

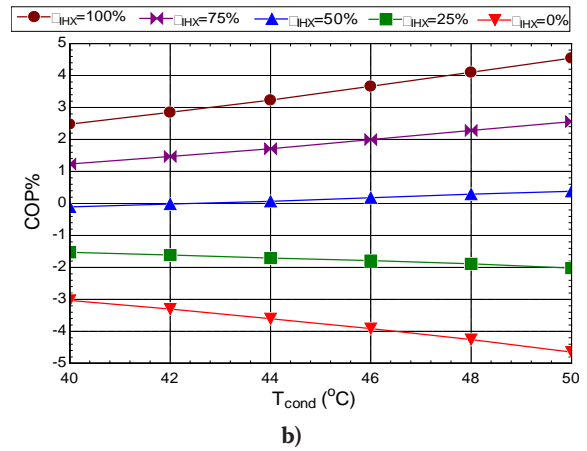
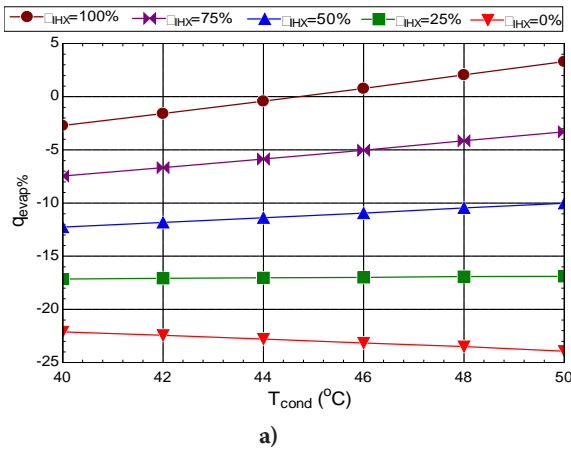


Figure 6. (a) $q_{evap}\%$ versus condensation temperatures, (b) COP% versus condensation temperatures

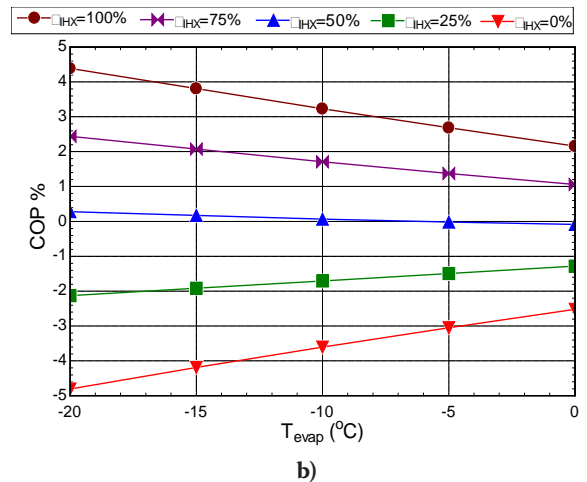
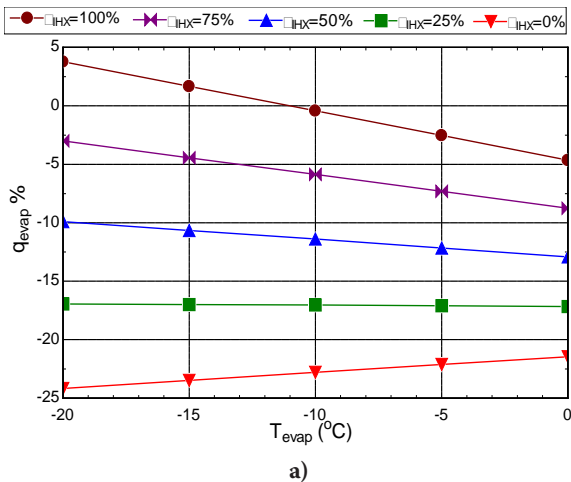


Figure 7. (a) $q_{evap}\%$ versus evaporation temperatures, (b) COP% versus evaporation temperatures

by increasing effectiveness as shown in Figure 3b. Furthermore, the rate of increase for superheat is higher than that of subcooling with increasing effectiveness.

Figure 4a, b shows the variations of subcooling and superheat versus evaporation temperature where the condensation temperature is maintained at 44°C. Subcooling and superheat tend to decrease while evaporation temperature increases due to reduction in specific heat values at the outlets of IHX for the evaporator and condenser sides. It has to be noted that at 44°C of condensation temperature and -10°C of evaporation temperature, the subcooling and superheat are the same with respect to the IHX effectiveness.

The compressor discharge temperature is an important parameter for compressor performance due to the compressor oil operating working range. Figures 5a, b indicates the variation of compressor discharge temperature based on effectiveness. It was observed that for all operating conditions, the compressor discharge tempe

rature did not exceed 93 °C. However, these values were calculated when the isentropic efficiency of the compressor assumed as 1. In reality, the actual values would be obtained higher than these amounts.

The performance parameters of the cycle such as COP and q_{evap} values are highly depend on the condensation and evaporation temperatures of the refrigerant. Therefore, in Figures 6 and 7, the influence of the effectiveness on the cycle performance parameters for R1234yf was compared with the baseline cycle that utilizes R134a under various evaporation and condensation temperatures.

Figure 6a shows that the cooling capacity was decreased with increasing condensation temperature when the effectiveness was zero for R1234yf. The main factor affecting the cooling capacity is the decreasing enthalpy difference in the evaporator associated with the increasing condensation temperature. Conversely, the cooling capacity was increased because of higher subcooling supplied with adapted IHX to the cycle. On the other hand, the

cooling capacity of R1234yf was higher than R134a after 44°C condensation temperature with 100% effectiveness. However, the relative COP difference was closed at 42°C condensation temperature with 50% effectiveness as shown in figure 6b. Above 50% effectiveness the COP of R1234yf is higher than R134a regardless to the condensation temperature. This situation is directly related with the energy consumption in the compressor. For instance, at 42°C condensation temperature with 50% effectiveness, the relative cooling capacity and COP are 12% and 0%, respectively. This is due to the smaller energy requirement of R1234yf to run the compressor for the same conditions in comparison with R134a.

Figure 7a shows that the cooling capacity increases with the increasing evaporation temperature at zero effectiveness. Besides, it was determined that the IHX was helped to improve the cooling capacity. The cooling capacity difference is nearly the same for all investigated evaporation temperature. However, when the effectiveness is above 25%, the difference is getting wider with increasing evaporation temperature. The most dramatically reduction was observed when the evaporation temperature is increased at the 100% effectiveness value. Figure 7b indicates that the relative COP difference changed similarly with the cooling capacity. However, the critical effectiveness to achieve the same COP is 50% for R1234yf.

CONCLUSION

In this theoretical study, the performance parameters of R1234yf were evaluated for various condensation and evaporation temperature by adding the IHX to the refrigeration cycle. The results were compared under varying IHX effectiveness with basic cycle of R134a. The outcomes from theoretical analysis can be summarized as follows:

- The subcooling and superheat degrees are increase with increasing condensation temperature. On the contrary, these values are declined with increasing evaporation temperature. Besides, these values increase with increasing effectiveness, regardless to the operating temperatures and the rate of increase for superheat is higher than that of subcooling.
- Similarly, increasing effectiveness causes the compressor discharge temperature increases. In reality, when the compressor discharge temperature exceeds 100°C, it should be considered for the safety reasons.
- At 25% effectiveness, the relative cooling capacity difference is not influenced by the variation of condensation and evaporation temperature.

Although, in high condensation and low evaporation temperature conditions, the relative cooling capacity difference increases with increasing IHX effectiveness.

- Moreover, relative cooling capacity and COP difference are changed similarly under various evaporation and condensation temperatures. Finally, the critical effectiveness value to achieve the same COP with R1234yf is 50%.

ACKNOWLEDGEMENTS

The authors would like to thank the University of Yalova for supporting this study through a Research Project No: 2015/BAP/123.

REFERENCES

1. Directive 2006/40/EC of the European Parliament and of the Council of 17 May 2006 Relating to Emissions from Air Conditioning Systems in Motor Vehicles and Amending Council Directive 70/156/EC, 2006.
2. Regulation 517/2014/EU of the European Parliament and the Council of 16 April 2014 on Fluorinated Greenhouse Gases and Repealing Regulation (EC) No 842/2006. Official Journal of the European Union, 2014.
3. Solomon S, Qin D, Manning M, Chen Z, Marquis M, Averyt KB, Tignor M, Mille HL. Contribution of Working Groups I, II and III to the Fourth Assessment Report of the Intergovernmental Panel on Climate Change. Cambridge University Press, New York, 2007.
4. Zhaofeng M, Hua Z, Jinyou Q, Mingjing L. Theoretical Analysis of R1234ze(E), R152a, and R1234ze(E)/R152a Mixtures as Replacements of R134a in Vapor Compression System. *Advances in Mechanical Engineering* 8 (2016) 1–10.
5. Mota-Babiloni A, Navarro-Esbri J, Barragan-Cervera A, Moles F, Peris B. Analysis Based on EU Regulation No 517/2014 of new HFC/HFO Mixtures as Alternatives of High GWP Refrigerants in Refrigeration and HVAC Systems. *International Journal of Refrigeration* 52 (2015) 21–31.
6. Jarall S. Study of Refrigeration System with HFO-1234yf as a Working Fluid. *International Journal of Refrigeration* 35 (2012) 1668–1677.
7. Papadimitriou VC, Talukdar RK, Portmann RW, Ravishankara AR, Burkholder JB. CF₃CF=CH₂ and (Z)-CF₃CF=CHF: Temperature Dependent OH Rate Coefficients and Global Warming Potentials. *Physical Chemistry Chemical Physics* 10 (2008) 808–820.
8. Akasaka R, Tanaka K, Higashi Y. Thermodynamic Property Modeling for 2,3,3,3-tetrafluoropropene (HFO-1234yf). *International Journal of Refrigeration* 33 (2010) 52–60.
9. Naushad AA, Bipin Y, Jitendra K. Theoretical Exergy Analysis of HFO-1234yf and HFO-1234ze as an Alternative Replacement of HFC-134a in Simple Vapour Compression Refrigeration System. *International Journal of Scientific & Engineering Research* 4 (2013) 137–144.
10. Hoşöz M, Suhermanto M, Aral MC. Comparative Experimental Performance of an Automotive Air Conditioning System Using Refrigerants R1234yf and R134a, in: Solmaz E, Kaya

- N, Öztürk F (Eds.). 8. Automotive Technologies Congress. Paper presented at Automotive Engineering Department, Uludağ University, Bursa, 23-24 May, 2016.
11. Zilio C, Brown JS, Schiochet G, Cavallini A. The Refrigerant R1234yf in Air Conditioning Systems. *Energy* 36 (2011) 6110-6120.
 12. Daviran S, Kasaeian A, Golzari S, Mahian O, Nasirivatan S, Wongwises S. A Comparative Study on the Performance of HFO-1234yf and HFC-134a as an Alternative in Automotive Air Conditioning Systems. *Applied Thermal Engineering* 110 (2017) 1091-1100.
 13. Qi Z. Performance Improvement Potentials of R1234yf Mobile Air Conditioning System. *International Journal of Refrigeration* 58 (2015) 35-40.
 14. Navarro-Esbri J, Mendoza-Miranda JM, Mota-Babiloni A, Barragan-Cervera A, Belman-Flores JM. Experimental Analysis of R1234yf as a Drop-in Replacement for R134a in a Vapor Compression System. *International Journal of Refrigeration* 36 (2013) 870-880.
 15. Mota-Babiloni A, Navarro-Esbri J, Barragan-Cervera A, Moles F, Peris B. Drop-in Energy Performance Evaluation of R1234yf and R1234ze(E) in a Vapor compression system as R134a replacements. *Applied Thermal Engineering* 71 (2014) 259-265.
 16. Domanski PA, Didion DA, Doyle JP. Evaluation of Suction Line - Liquid Line Heat Exchange in the Refrigeration Cycle, *International Refrigeration and Air Conditioning Conference*. Paper presented at Purdue University, pp.131-139, 1992.
 17. Aprea C, Ascani M, De Rossi F. A Criterion for Predicting the Possible Advantage of Adopting a Suction/Liquid Heat Exchanger in Refrigerating System. *Applied Thermal Engineering* 19 (1999) 329-336.
 18. Klein SA, Reindl DT, Brownell K. Refrigeration System Performance Using Liquid-Suction Heat Exchangers. *International Journal of Refrigeration* 23 (2000) 588-596.
 19. Mastrullo R, Mauro AW, Tino S, Vanoli GP. A Chart for Predicting the Possible Advantage of Adopting a Suction/Liquid Heat Exchanger in Refrigerating System. *Applied Thermal Engineering* 27 (2007) 2443-2448.
 20. Moles F, Navarro-Esbri J, Peris B, Mota-Babiloni A, Barragan-Cervera A. Theoretical Energy Performance Evaluation of Different Single Stage Vapour Compression Refrigeration Configurations Using R1234yf and R1234ze(E) as Working Fluids. *International Journal of Refrigeration* 44 (2014) 141-150.
 21. Cho H, Park C. Experimental Investigation of Performance and Exergy Analysis of Automotive Air Conditioning Systems Using Refrigerant R1234yf at Various Compressor Speeds. *Applied Thermal Engineering* 101 (2016) 30-37.
 22. Navarro-Esbri J, Moles F, Barragan-Cervera A. Experimental Analysis of the Internal Heat Exchanger Influence on a Vapour Compression System Performance Working with R1234yf as a Drop-in Replacement for R134a. *Applied Thermal Engineering* 59 (2013) 153-161.
 23. Pottker G, Hrnjak P. Experimental Investigation of the Effect of Condenser Subcooling in R134a and R1234yf Air Conditioning Systems with and without Internal Heat Exchanger. *International Journal of Refrigeration* 50 (2015) 104-113.
 24. Klein SA. Engineering Equation Solver (EES), Professional version V9.723-3D, F-Chart Software (2010).

Design and Analysis of In-Drum Outer Rotor BLDC Motor for Eddy Current Separator

Ahmet Fenercioglu¹ and Merve Sen Kurt²

¹Gaziosmanpasa University, Department of Mechatronic Engineering, Tokat, TURKEY

²Amasya University, Department of Electric and Electronics Engineering, Amasya, TURKEY

ABSTRACT

In this study, a novel In-Drum Brushless Direct Current (ID-BLDC) motor is proposed to Eddy Current Separator (ECS) which separates nonferrous metals from waste. The ECS's separation efficiency depends on magnetic drum speed. ID-BLDC motor is designed with outer rotor structure and placed in ECS magnetic drum in order to improve separation efficiency. The magnetic drum is directly driven by this motor because it doesn't require coupling mechanisms. It has very simple structure since no rotor windings, brushes and bracelets. The ID-BLDC motor has high reliability, high efficiency and high power-to-volume ratio. Proposed motor has 8 poles, 3 phases, 373 W (0.5 HP) and 1750 rpm rated speed. Output parameters are calculated for full load and verified by Finite Element Analysis (FEA) under the over load, full load, half load, quarter load and no load conditions for transient and steady state.

Keywords:

Brushless motors; Outer rotor motors; Permanent magnet motors; Finite element analysis (FEA); Eddy current separator

INTRODUCTION

ECS is a machine that provides recycling via separation of nonferrous metals by means of the eddy current effect. It separates copper, aluminum, brass, silver and similar valuable metals from wastes. The most important component of ECS that affects separation performance is magnetic drum. Higher rates of rotation and the multipolarity of the magnetic drum results in greater magnitudes of eddy currents in the metal that will be separated according to Faraday principles. In this case, the separation efficiency increases, while making the separation of smaller sized particles possible [1].

In General ECS, the drum is driven by a coupled motor. This motor rotates the drum directly by coupling or with a belt and pulley mechanism. In this case, reaching higher speeds is difficult due to loss in transfer organs and the balance effect. ECS machine and working principle scheme are given in Fig.1.

This study proposes the design of an outer rotor BLDC motor to be installed in the drum to increase the ECS performance and to separate metals with small particle sizes. A BLDC motor consists of a stator with

Article History:

Received: 2017/02/02

Accepted: 2017/04/05

Online: 2017/06/30

Correspondence to: Merve Sen Kurt,
Amasya University, Department of
Electric and Electronics Engineering,
Amasya, TURKEY.

Tel: +90 (358) 260-0066 (1468)

E-Mail: mervesenkurt@gmail.com

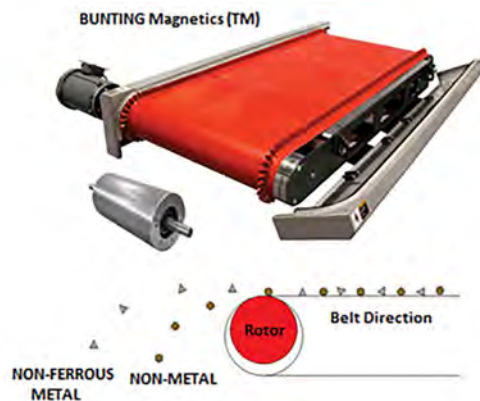


Figure 1. ECS machine and working principle (BUNTING Magnetics (TM)).

coils, a rotor with permanent magnets, position sensors and driver circuits. The driver circuits assume the role of the brush collector setup of classic brushed DC motors, while the position sensors provide the rotor position data to the controller. Based on position data and the rotation direction, the controller excites the related motor phase.

BLDC is placed in a drum with an out runner rotor. In these types of motors, the stator is fixed at the center of the motor and the rotor made of permanent magnets rotates around the stator. It drives the drum directly without a requirement of motion transfer organs. Hence, it has a higher efficiency due to the fact that there is no mechanical transfer loss and that it can work at high rates. The motor requires less space since it is located in the drum in comparison with drums that are driven externally and it is also aesthetically pleasing.

Literature surveys carried out put forth that there are no studies related to the application of BLDC motor in the drum. However, there are several studies about outer rotor BLDC designs. Some of these studies are summarized below:

In outer rotor BLDC motors, the width of the stator slots significantly affect the produced cogging torque. It was observed that BLDC motors designed with wide slots produced higher cogging torque [2].

The geometric structure and basic parameters (PM angle, PM residual induction, PM relative permeability, PM height, rotor yoke height) of permanent magnets that are present in the outer rotor BLDC motors affect the magnetic flux generated in the air gap. The change in magnetic flux generated for various parameters was analyzed by finite elements method by taking the geometric structure of the permanent magnets and the nonlinear characteristics into account [3].

The armature flux generated by the current passing through the BLDC motor's stator coils is omitted when the motor runs in an unsaturated area. However, when the motor is run in a saturated area, it is stated that this effect grows, disrupts the air gap flux density thus failing to reach a uniform torque distribution [4].

The outer rotor BLDC motor drives with permanent magnets were also covered for electrical and hybrid vehicles. The machine topology, driver operations and control strategies were emphasized [5].

An outer rotor BLDC motor was designed for light traction at low rates using finite elements method (FEM). Rate, phase current, power and torque curves with respect to time were assessed to observe the performance of the designed motor's [6].

A hybrid permanent magnet hydrodynamic bearing was designed. It works passively and contactless. Various permanent magnet topologies are studied and analyzed by FEM in terms of axial forces and stiffness [7].

It was studied about a current distribution control on dual direct-driven wheel motors for electric vehicles. The vehicle dynamics and control strategy are modeled and the control performance is simulated numerically [8].

The application of the VSS (variable structure system) approach to the position control of an AC brushless servo motor is discussed. A DSP (digital signal processor) is used to make the time needed to calculate the control input [9].

H2 and H_{∞} controllers were designed for a permanent-magnet synchronous motor drive system without using shaft position sensor, and presents the field-weakening control algorithm of the drive system. [10].

In this study, a BLCD motor design was proposed for an ECS magnetic drum drive. The motor has an outer rotor and is placed in the drum. This way, the system has a high efficiency, as is the case for direct drive, since there will be no power transfer losses in the drum. This predicted motor design was verified for the predicted system via analytical methods and magnetic analyses were carried out for various loads via finite elements methods. In these analyses, torque, phase currents and rate parameters were calculated for temporary and permanent states, and presented with graphs.

ID_BLDC MOTOR

The ID-BLDC motor is an outer brushless DC motor that is placed in the drum. The stator of this motor is fixed and attached to a fixed shaft. The rotor is coupled to the drum and provides motion. Permanent magnet poles are used in the motor's rotor. The power/volume ratio of the motor is high due to the additional power provided by the magnets. As such, the proposed motor can easily be placed in the drum due to its smaller size. Since the motor has an outer rotor, it provides advantages such as high torque and less noise [11], due to the increased rotor diameter. The only disadvantage of ID-BLDC motors is difficulty in cooling since it is inside the stator. However, since the motor in ECS works under the constant load, the motor works at nominal current. Therefore, overheating does not occur.

Motor Selection

The weight of the drum (m), inertia moment (J), angular acceleration (α) and motor speed (n) were taken into account in order to determine the predicted motor power. The drum in which the ID-BLDC was placed in is shown in Figure 2a and Figure 2b. The length of the drum $l_d = 0.3$ m, the outer radius $R_1 = 0.056$ m and the inner radius is $R_2 = 0.046$ m.

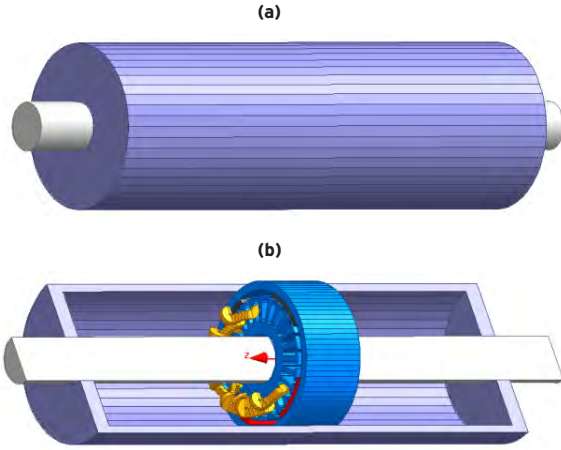


Figure 2. a) Drum, b) ID-BLDC motor inside of the drum

The acceleration time it took for the motor to reach the rated speed was taken as 3 seconds. With these data at hand, the volume and specific weight of the drum were initially considered, and the mass (m) of the drum was calculated as approximately 10 kg. To determine the inertial moment, the gyration radius (R_0) is calculated using Equation 1:

$$R_0 = \sqrt{\frac{R_1^2 + R_2^2}{2}} \quad (1)$$

From this point, the inertial moment is calculated with Equation 2:

$$J = mR_0^2 \quad (2)$$

The torque required to bring the drum to its rated speed in 3 seconds is calculated with Equation 3:

$$T = j\alpha \quad (3)$$

Using these equations, the moment is calculated as 1.59 Nm. When the 1750 rpm rate is taken into account, the required motor power is found as 291.38 W by using Equation 4. The nominal power of the motor is proposed as 0.5 HP (373 W) by taking the losses into consideration.

$$P = T\omega \quad (4)$$

The ID-BLDC motor can be controlled with an appropriate BLDC motor driver. Table 1 consists of nominal values of the ID-BLDC motor.

The ID-BLDC motor can be controlled with an appropriate BLDC motor driver. Table 1 consists of nominal values of the ID-BLDC motor.

Table 1. Rated values of the IN-BLDC motor

Nominal elements of the formulas	Nominal Value
Output Power (HP)	0.5
Voltage (V)	220
Current (A)	1.76
Efficiency (%)	82.92
Speed (rpm)	1750
Torque (Nm)	1.75

Table 2 shows the model's dimensions, and Figure 3 shows the cross-sectional view of the model.

Table 2. ID-BLDC motor dimensions

Symbol	Quantity	Size
D_{ri}	Rotor Inner Diameter	0.082 m
D_{ro}	Rotor Outer Diameter	0.092 m
D_{sh}	Shaft Diameter	0.03 m
D_{si}	Stator Inner Diameter	0.03 m
D_{so}	Stator Outer Diameter	0.074 m
L_{sl}	Stack Length	0.04 m
L_g	Air Gap Thickness	0.001 m
N_r	Number of Rotor Poles	8
N_s	Number of Stator Poles	24
β_m	Magnet Degree	0.79 rad

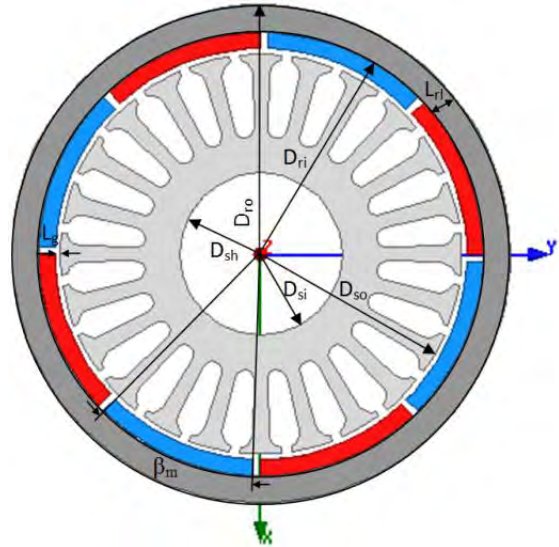


Figure 3. ID-BLDC's cross section and dimension expressions

Electromagnetic Model of ID-BLDC

Core reluctance was omitted as the air gap and the magnetic reluctance are high in BLDC motors. In this case, the air gap reluctance (R_g) and the permanent magnet reluctance (R_m) in the magnetic circuit of an ID-BLDC, as seen in Figure 4, is calculated using Equation 5. Where l_g is air gap distance and l_m is magnet length, S is the effective surface area of stator pole.

$$R_g = \frac{l_g}{\mu_0 S} \quad R_m = \frac{l_m}{\mu_m S} \quad (5)$$

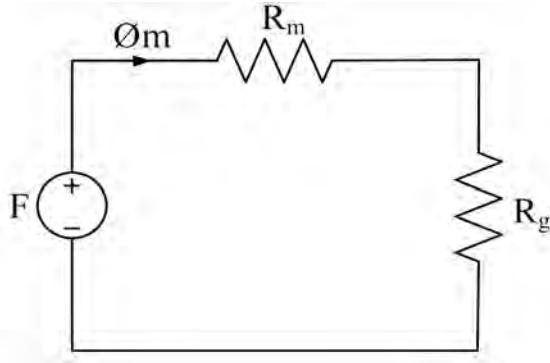


Figure 4. a) Drum, b) ID-BLDC motor inside of the drum

If magnet permeability (μ_m) and vacuum permeability (μ_0) are assumed to be equal ($\mu_m = \mu_0$) the total reluctance of the magnetic circuit is expressed as shown in Equation 6 [12].

$$R_t = R_g + R_m = \frac{l_g + l_m}{\mu_0 S} \quad (6)$$

Magnetic permanence (ρ_0) is calculated via Equation 7:

$$\rho_0 = \frac{1}{R_t} = \frac{\mu_0 S}{l_g + l_m} \quad (7)$$

The total flux (ϕ) in magnetic circuit shown in Figure 4 [13]. Where B_m, B_g are magnet and air gap magnetic flux densities, A_m, A_g are the cross sectional areas of magnet and air gap respectively. H_g is the magnetic field intensity in air gap.

$$\phi = B_m A_m = B_g A_g = \mu_0 H_g A_g \quad (8)$$

The magnetic flux density (B_m) is found by using Equation 9 [13]. Where μ_r is the relative permeability and H_m is the magnetic field intensity in the magnet.

$$B_m = \mu_r \mu_0 H_m \quad (9)$$

Equation 10 is derived from Equation 8 and Equation 9:

$$\phi = \mu_r \mu_0 H_m A_m \quad (10)$$

Magneto motive force (F) is found by using Equation 11:

$$F = \phi R_t = NI = l_m H_m + l_g H_g \quad (11)$$

Where N is the number of turn. The current (I) passing through the stator coils is derived from Eq.11 and is calculated by Eq.12 [14].

$$I = \frac{\phi R}{N} \quad (12)$$

The power (P) is supplied from the network is found by using Equation 13. The rated voltage applied on the motor is 220 V DC.

$$P = UI \quad (13)$$

Basically torque can be calculated by using Equation (4). The efficiency is output mechanical power (P_m) to input electrical power (P_i) ratio. Electrical and mechanical powers are found Eq.13 and Eq. 4 respectively.

ASSUMPTIONS

The magnetic flux in the core is assumed to be uniform in analytical calculations. The saturation effects were not taken into account and BH characteristic of the core material was assumed to be linear.

The analyses were carried out using ANSYS/Maxwell program which solves equations via 2D finite elements method. M19 material was used as core material. The BH curve of this material is given in Figure 5. The NdFeB (N35) magnets are allocated on rotor surface. For the motor control, a standard BLDC motor drive was used. In FEA, motor is driven by external circuit. This circuit is taken into consideration, voltages and speed are accepted as constant in steady state.

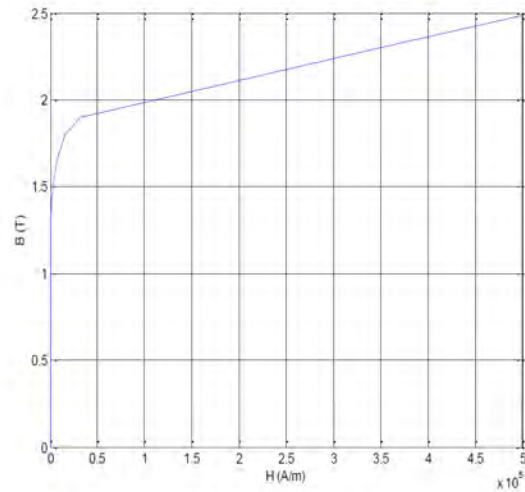


Figure 5. BH curve of M19 material

FINITE ELEMENT ANALYSIS (FEA)

2D transient analyses of proposed motor were carried out with FEA software AnSys Maxwell. For the analysis, the calculations were obtained for no-load, 25%, 50%, full-load, 125%, and overload (150%) conditions. The change in speed with respect to time are shown in Figure 6, with taking the FEA transient results into account. Figure 6a shows the change in speed with respect to load in transi-

ent state, and Figure 6b shows the average change in speed for steady-state conditions.

As can be seen in Figure 6a, the motor reaches steady state after 60 ms. And as seen in Figure 6a and 6b, as the motor load increases, the decrease in armature voltage and the flux in air gap increases, causing the decrease in motor speed.

For various loads of the ID-BLDC motor, Figure 7a shows the transient torque change, and Figure 7b shows the average electromagnetic torque curves for steady state.

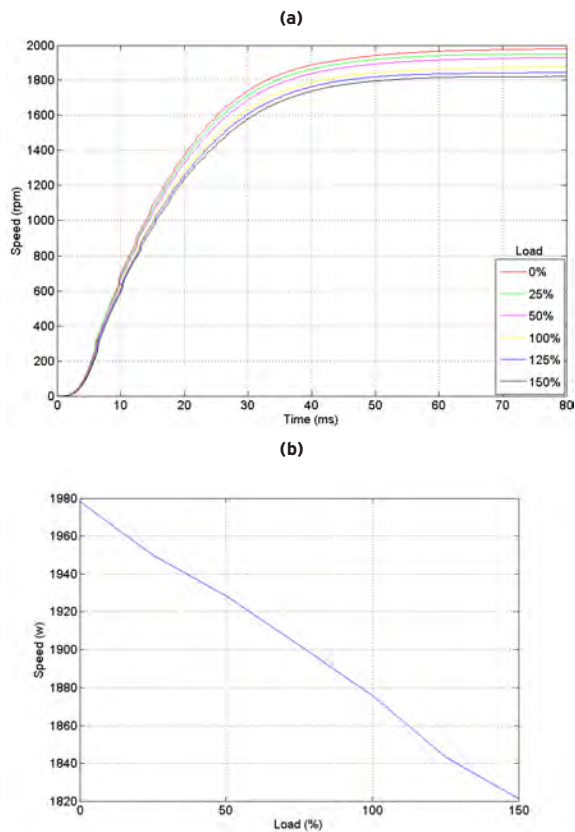


Figure 6. ID-BLDC change in motor rate a) transient rate b) steady state average rate

From Figure 7b, it can be seen that the torque increases with increasing load. With increasing current, the flux in the core increases. According to the BH characteristics, saturation in the core begins approximately at 1.5 T. In the saturated zone, the increase magnetic flux in the saturated zone does not increase proportionally with current; therefore the torque does not increase in the similar proportion. It is seen that after full-load, the average torque value increases less when compared to increasing load. The phase currents diagrams are shown in Figure 8. The phase current for full-load is calculated as 1.88 A in rms. The phase approxi-

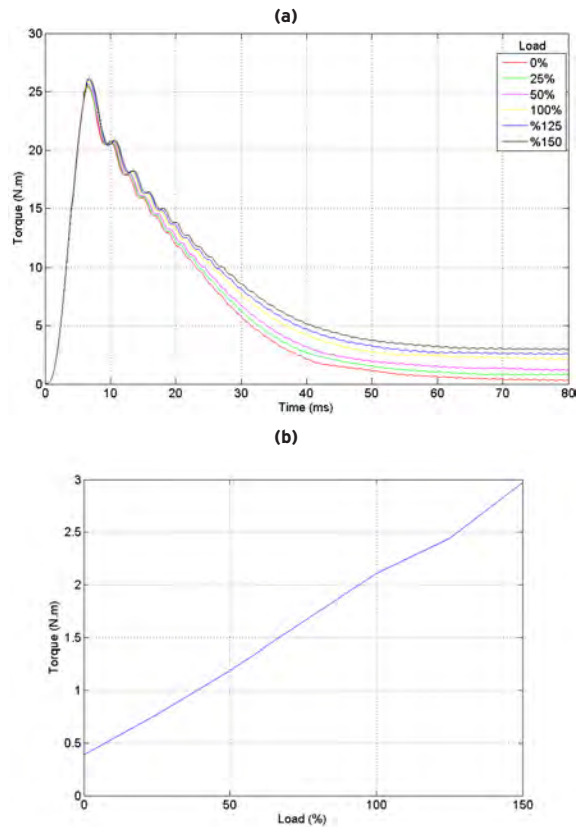


Figure 7. ID-BLDC motor electromagnetic torque profile a) transient torque b) steady state average torque

mately has a sinusoidal profile. It is seen that in the starting, motor phase currents are too much, and it reaches its rated value after 60 ms.

The stator magnetic flux density distribution of ID-BLDC motor at full-load is given in Figure 9. Flux density distributions have been shown a) vector at Figure 9a, b) magnitude at Figure 9b and c) flux curves at Figure 9c.

The BH curves of the core material chosen in the analyses are shown in Figure 5. The saturation begins after 1.5 T in this material. Saturation begins at stator slot teeth in flux

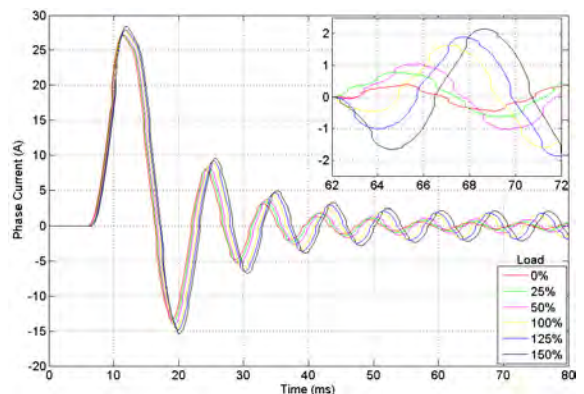


Figure 8. Phase currents according to load

distributions. There is approximately 1.2 T magnetic flux density in the rotor and the air gap. Additionally, the air gap flux density was calculated as 1.23 T analytically from the magnetic model. FEA and analytical results are compared in Table 3.

CONCLUSION

ECS are commonly used to separate and recycle nonferrous valuable metals such as copper, aluminium from waste. The most important component that affects ECS separation efficiency is the magnetic drum. The drum must be rotated at high speeds in order to separate small

The proposed motor has no brushes, bracelets, salient poles and rotor winding. Proposed new ECS drum which driven by ID-BLDC motor has no power transfer mechanisms. Thus it decreases the losses and the required maintenance, and has the motor works quietly. It can be reach high speed.

The motor power selected 0.5 HP (373 W) according to the drum dimensions. Designed ID-BLDC motor's rated values are 220 V, 1.71A, 1750 rpm, 1.70 Nm, %83 efficiency. Electrical and magnetic parameters such as power requirement of drum, magnetic reluctance, flux density, magneto motive force, current, torque, speed, efficiency and power were examined. Parameters were predicted by analytical calculations and verified by FE analyses for different load conditions. In full load, the power is calculated 371,7 W in analytical predictions and analyzed 414 W in FEA. Analytical solutions were made in linearity. FEA solutions were taken into consideration non-linearity and BH curve of the material. Thus the difference is in acceptable limits.

This ID-BLDC motor is an original study. It is proposed for a new ECS drum design to improve separation efficiency.

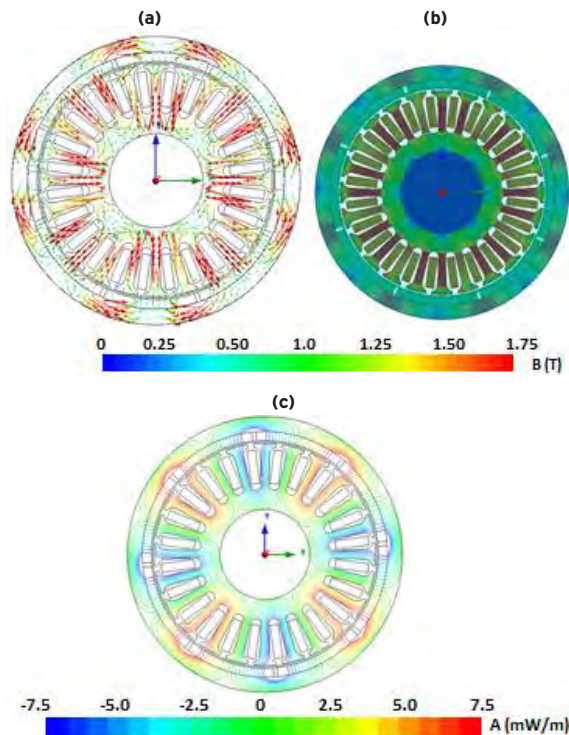


Figure 9. Flux distributions a) vector b) magnitude c) flux lines

Table 3. FEA and analytical results of motor output values at full-load

Results	Current(A)	Torque (Nm)	Power (W)	Rate (rpm)
FEA	1.88	2.106	414	1750
Analytical	1.64	1.98	361.7	1750

metals in form of granules. The losses are great and speed limits occur when the drum is driven via coupling, sprockets or belt-pulleys.

In this study, the BLDC motor has designed with outer (external) rotor and it has placed in the drum and driven directly. It has called ID-BLDC motor. The magnetic drum can reach high speeds with this motor thus making it possible to separate and recover small particles. In addition, the motor will cover less space while being aesthetically appealing since it will be completely in the drum.

REFERENCES

1. Rem PC, Beunder EM, van den Akker AJ. Simulation of eddy-current separators. *IEEE Transactions on Magnetics* 34 (1998) pp. 2280–2286.
2. Nizam M, Waloyo HT, and Inayati. Design of optimal outer rotor brushless dc motor for minimum cogging torque, 2013 Joint Int. Conf. on Rural Inf. & Communication Technol. and Electr.-Vehicle Technol. (rICT & ICeV-T), Bandung-Bali, Indonesia, 2013, pp. 1-4.
3. Dirba J, Lavrinovicha L, Onzevs O, Vitolina S. The influence of permanent magnet parameters on the effectiveness of brushless DC motor with outer rotor, 2012 Int. Conf. on Power Electronics Electr. Drives, Automation and Motion (SPEEDAM), Sorrento, Italy, 2012, pp. 718–723.
4. Kerdsup B, Fuengwarodsakul NH. Analysis of brushless DC motor in operation with magnetic saturation using FE method, 2011 8th Int. Conf. on Electr. Eng. Electronics, Comput. Telecommun. And Inf. Technol. (ECTI-CON), Khon Kaen, Thailand, 2011, pp. 629-632.
5. Chau KT, Chan CC, Chunhua L. Overview of permanent-magnet brushless drives for electric and hybrid electric vehicle. *IEEE Transactions on Industrial Electronics* 55 (2008) pp. 2246–2257.
6. Lopez-Fernandez XM, Gyselinck J. Design of an outer-rotor permanent-magnet brushless DC motor for light traction through transient finite element analysis, 2016 Int. Conf. on Computational Electromagnetics (CEM), Aachen, Germany, 2006, pp. 1-2.
7. Pohlmann A, Hameyer K. A study permanent magnet topologies for hybrid bearings for medical drives applied in ventricular assist devices. *Archives of Electrical Engineering* 60 (2011) pp. 371–380.
8. Yang YP, Lo CP. Current distribution control of dual

- directly driven wheel motors for electric vehicles. *Control Engineering Practice* 16 (2008) pp. 1285-1292.
9. Hashimoto H, Nakayama T, Kondo S, Harashima F. Practical variable structure approach for brushless servo motor control practical implementation of DSP, 19th Annu. IEEE Conf. on Power Electronics and Specialists, Kyoto, Japan, 1988, pp. 207-213.
 10. Liu TH, Cheng CP. Controller design for a sensorless permanent-magnet synchronous drive system. *IEE Proc. B-Electr. Power Applications* 140 (1993) pp. 369-378.
 11. Lelkes A, Krottsch J, Doncker RW. Low-noise external rotor BLDC motor for fan applications, 37th IAS Annu. Meeting on Ind. Applications Conf., USA, 2002, pp. 2036-2042.
 12. Wu H, Wang Z, Lv X. Design and simulation of axial flow maglev blood pump. *I. J. Inf. Engineering and Electronic Business* 2 (2011) pp. 42-48.
 13. Fitzgerald AE, Kingsley C, Umans SD. *Electric Machinery*, sixth ed. McGraw-Hill, New York, 2002.
 14. Hemati N, Leu MC. A complete model characterization of brushless DC motors. *IEEE Transactions on Industrial Applications* 28 (1992) pp. 172-180.

Seasonal and Spatial Variation of Epilithic Algal Community in Batlama Stream (Giresun, Turkey)

Faruk Maraşlıoğlu¹, Elif Neyran Soylu², Sibel Altürk Karaca²

¹ Hitit University, Department of Environmental Protection Technologies, Çorum, TURKEY

² Giresun University, Department of Biology, Giresun, TURKEY

ABSTRACT

Spatio-temporal changes in taxonomic composition and structure of epilithic algal community with some physicochemical features of the Batlama stream were assessed between June 2013 and May 2014 at the intertidal zone of the Batlama Stream, Giresun, Turkey. A total of 90 taxa were identified belonging to division of Bacillariophyta (80 taxa), Euglenophyta (3 taxa), Cyanobacteria (3 taxa), Charophyta (2 taxa) and Chlorophyta (2 taxa) on epilithic algae of Batlama Stream. *Encyonema minutum*, *Ulnaria ulna*, *Cocconeis placentula*, and *Navicula cryptocephala* species were the most abundant taxa among all samples of the four stations throughout the study.

The Shannon diversity index (H') values varied in the range from 0.5 to 1.2 and correlated with both species richness and relative species abundance (evenness). The results of the diversity analysis and the counting did not exactly match up with each other. Chlorophyll-a values of the stream and trophic classification (TDI, BDI) based on epilithic diatoms ascribed Batlama Stream to the mezotrophic range. Also, according to the calculated pollution index (PTI, S) values, all stations of the Batlama Stream were moderately polluted (β -mesosaprobity).

Keywords:

Stream; Epilithic algae; Seasonal variation; Diversity; Diatom index.

INTRODUCTION

Diatoms, besides the role of environmental condition indicator, also determine the water quality and are as interesting and intriguing phytoplanktons, as snowflakes. They took a primary role in various studies, in terms of oxygen, nutritional value and pollution indicator. The main primary producers in undisturbed and shaded zones of the streams are epilithic algae and play major roles in controlling energy flow of food webs in stream ecosystems [1, 2]. However, the overgrowth of epilithic algae may deteriorate water quality [3]. The production and dynamics of an epilithic algal composition in stream ecosystems are also largely influenced by physical variables such as flow rate, light and water temperature [4, 5]. The variation of epilithic algal biomass may indirectly affect the distribution of the Batlama stream. Water quality variables (electrical conductivity, pH, total dissolved solids, chemical oxygen demand, biochemical oxygen demand, and nutrients such as phosphorus and nitrogen from the surrounding lands) also play major roles in regulating the production rate and species com-

position of epilithic algae in streams [6]. However, in complex stream ecosystems, the dynamics of epilithic algal biomass may nonlinearly interact with the combination of abiotic and biotic factors. Therefore, some index varieties may help to describe the nonlinear relationships between epilithic algal biomass and aforementioned factors.

In Turkey, studies of diatom were began by Yıldız in Meram stream [7] and followed by other researchers which mostly concentrated on various physicochemical factors affecting the development of diatoms in addition to their flora in central anatolian [9, 10, 11, 12, 13, 14, 15, 16]. In recent years, some topics that determine trophic state and water quality level of a stream monitoring by means of diatom indices based on the variety and density of the diatoms in water or on the substrat have become popular [17, 18, 19].

The TDI was designed with the practical needs of busy water industry biologists in mind and, as a result,

Article History:

Received: 2017/01/06

Accepted: 2017/02/18

Online: 2017/06/30

Correspondence to: Faruk Maraşlıoğlu,
Hitit University, Department of
Environmental Protection Technologies,
Çorum, TURKEY

Tel: +90 (364) 223-8000-3376

Fax: +90 (364) 223-8004

E-Mail: farukmaraslioglu@hitit.edu.tr

was designed to be robust and easily learnt. It uses the weighted average equation of Zelinka and Marvan [20] to interpret benthic diatom community structure in terms of the nutrient concentrations in the river.

Epilithic algal samples obtained in the present study comprised of mixed forms growing on silicate-rich stones and phytoplankton forms commonly living in littoral and pelagic zones of freshwaters, however, in this context this all community was termed as epilithon. The aims of the present study were to describe the species composition of diatom assemblages, to determine which environmental factors explain the composition of epilithic diatoms and to assess the response of common diatom taxa to these environmental variables..

MATERIALS AND METHODS

Samples analysed in this work were collected monthly between June 2013 and May 2014 from four stations (Fig. 1). Stones collected from the stations in the stream were brushed clean of algae and the samples fixed the formaldehyde solution (4%). The epilithic diatoms were then placed on permanent slides which had been prepared according to Round [21]. At least 300 diatom valves per slide were counted at 400x magnification on Olympus BX51 microscope. In the evaluations, the average of three countings from the station was used [22]. Species identifications were based primarily on the John *et al.* [23], Krammer and Lange-Bertalot [24, 25, 26, 27]. In addition, current systematic status of algae taxa is checked by way of AlgaeBase databases [28] and the author names are given in abbreviated form according to Brummit and Powel [29].

The Shannon diversity index, the evenness and species

richness were applied on epilithic flora at different stations. The software used was PRIMER version 5.0 from Plymouth Marine Laboratory for Shannon-Wiener index [30]. Trophic diatom index (TDI) and Biological Diatom Index (BDI) were calculated by using the formula [31] and "IBD Calculate With Excel" programme [32], respectively. Also, the saprobic index (S) was evaluated based on the formula proposed by Pantle and Buck [33] and the diatom pollution tolerance index (PTI) was calculated based on the formula [34]. Water temperature (°C), pH, and dissolved oxygen concentration (mg/l) were measured in situ with WTW multi 340i/SET model pH meter. After filtering through GF/C and extracting in cold 90% acetone, chlorophyll-a (chl-a) was determined according to the equations of Strickland and Parsons [35].

RESULTS AND DISCUSSION

A total of 90 taxa belonging to division of Bacillariophyta (80), Euglenophyta (3), Cyanobacteria (3), Charophyta (2) and Chlorophyta (2) were identified in this study (Table 1). Bacillariophyta members were rich in species diversity and intensity in the algal flora of Batlama Stream (Fig. 2).

Encyonema minutum, *Ulnaria ulna*, *Cocconeis placentula*, and *Navicula cryptocephala* were predominantly found species in all sampling stations in the study area (Fig. 3). Sienkiewicz [36] stated that *U. ulna* have wide trophic tolerance and can live in oligo-eutrophic water. So, to be dominant of *U. ulna* throughout the study period point to a mesotrophic environment. *Navicula cryptocephala* and *Ulnaria ulna* are known that broad to distribution in Turkey [37, 38].

Total organisms decreased their numbers during the months of high rainfall. Sivacı and Dere [39] reached also a



Figure 1. Locations of the sampling stations in Batlama Stream

Table 1. The list of common taxa found in all four stations of the Batlama Stream

Division: Bacillariophyta	
<i>Amphora ovalis</i> (Kütz.) Kütz.	<i>Melosira varians</i> C. Agardh
<i>Closterium navicula</i> (Bréb.) Lütkem.	<i>Navicula cryptocephala</i> Kütz.
<i>Cocconeis placentula</i> Ehrenb.	<i>Navicula lanceolata</i> (C. Agardh) Kütz.
<i>Cymatopleura solea</i> (Bréb.) W. Sm.	<i>Navicula menisculus</i> Schum.
<i>Cymbella affinis</i> Kütz.	<i>Navicula rhynchocephala</i> Kütz.
<i>Cymbella helvetica</i> Kütz.	<i>Navicula tripunctata</i> (O.F.Müller) Bory
<i>Cymbella tumida</i> (Bréb.) Van Heurck	<i>Navicula viridula</i> var. <i>linearis</i> Hustedt
<i>Diatoma vulgare</i> Bory	<i>Nitzschia acicularis</i> (Kütz.) W. Sm.
<i>Didymosphenia geminata</i> (Lyngb.) M.Schmidt	<i>Nitzschia palea</i> Kütz.
<i>Encyonema caespitosum</i> Kütz.	<i>Rhoicosphenia abbreviata</i> (C.Agardh) Lange-Bert.
<i>Encyonema minutum</i> (Hilse) D.G.Mann	<i>Surirella minuta</i> Bréb.
<i>Encyonema silesiacum</i> (Bleisch) D.G.Mann	<i>Ulnaria ulna</i> (Nitzsch) Compère
<i>Eunotia minor</i> (Kütz.) Grunov	Division: Chlorophyta
<i>Fragilaria capucina</i> Desmaz.	<i>Botryococcus braunii</i> Kütz.
<i>Gomphonema augur</i> Ehrenb.	Division: Cyanobacteria
<i>Gomphonema minutum</i> (C. Agardh) C. Agardh	<i>Oscillatoria tenuis</i> C. Agardh
<i>Gomphonema olivaceum</i> (Hornem.) Bréb.	Division: Euglenophyta
<i>Gyrosigma scalproides</i> (Rabenh.) Cleve	<i>Euglena gracilis</i> G.A.Klebs
<i>Hannaea arcus</i> (Ehrenb.) R.M.Patrick	<i>Euglena viridis</i> (O.F. Müll.) Ehrenb.

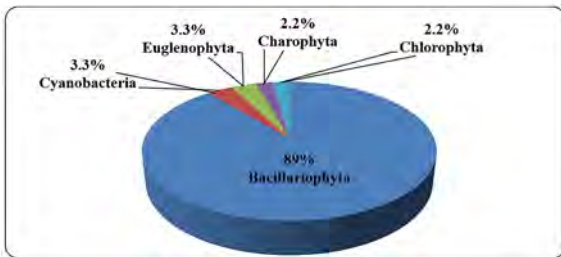


Figure 2. % Distribution of Epilithic Algal Composition in Batlama Stream

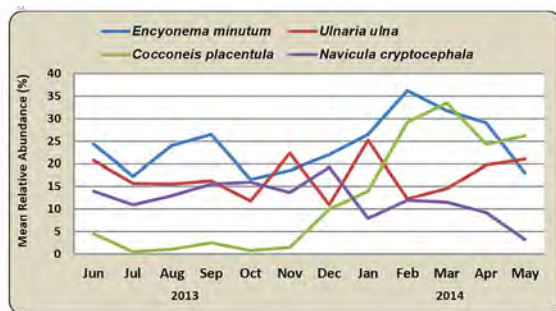


Figure 3. Seasonal variations of predominant species in the epilithon of the Batlama stream

very similar conclusion during their study. Species diversity increased in the months of which the water temperature rise. Yavuz and Çetin [40] had recorded that relationship between seasonal variation of algae and water temperature.

The all parameters are high during the study period except winter. Water temperature ranged between 5.2 and

24.3°C in the stream. The development of epilithic algae in the stream affected by water temperature. The epilithic algal density was lower in some months except February and November than the other months when the temperature was low. In the stream throughout the research period, whereas the maximum oxygen level was 14 mg/l, the minimum level was 2 mg/l. The solubility of oxygen in the water decreases with the increase in temperature [41]. The density of oxygen in a natural oligotrophic freshwater having a temperature around 20°C is about 10 mg/l [42]. The average pH value of 7.8 indicates that the stream is slightly alkaline. The abundance of *Encyonema minutum*, *Ulnaria ulna* and *Navicula cryptocephala* in present study supports the Round's idea [43] that these species are widespread in alkaline waters. When total cell numbers were found to be high in autumn and winter seasons the pH values also reached similarly high values in these months in the study area. This result did not support the Vinebrooke's view [44] that algal growth decreases with pH increase.

The amount of chlorophyll-a were calculated monthly and chlorophyll-a showed usually similar values at the sampling stations. Chl-a ranged from 0.2 to 15.2 mg/m³ in Batlama stream. According to Moses [45] has stated that running water with chlorophyll-a values between 10 and 30 mg/m³ was mesotrophic. In term of the values, Batlama stream has a mesotrophic character.

The seasonal variation of Shannon diversity and even-

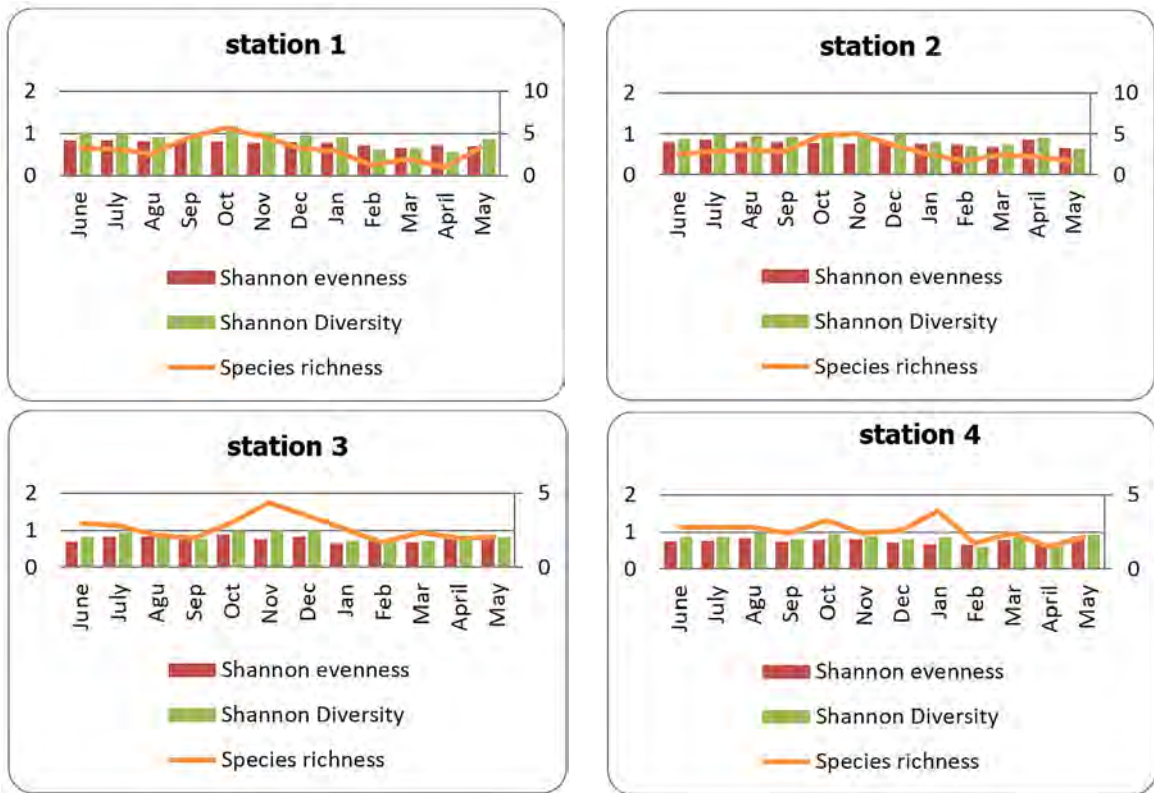


Figure 4. Shannon diversity, evenness, and species richness of the Batlama stream

ness did not vary greatly during the study period. While the highest values of the H' during the year was usually recorded in October, the lowest value was recorded in April. Recording the low value of Shannon diversity in April may be due to heavy rain mostly seen in Giresun in this month of the spring. In our study it was found that species diversity decreased in the spring and confirmed this with the Shannon diversity index. Species evenness index varied from 0.7–0.8. The lower species evenness values were often associated with the rainy season. Approaching the zero value of relative species abundance (evenness) indicates dominance of organism linked to single-species that *Encyonema minutum* and *Coconeis placentula* comprised of more than 80% of the all organisms in April 2014. Recording a decrease of H' and J' values with being the result of the excessive increase of these species indicates that Batlama stream is under pressure in these months of the year. The seasonal variations of species richness presented a decrease especially in cold period, while the highest values of species richness were recorded in autumn period (Fig. 4).

BDI and TDI indices provide information about trophic states of the lotic ecosystems. In the study, taxa with a mean relative abundance (%) less than 5 throughout the year were not included in the index calculation. Accordingly, 22 diatom taxa were used in St.1 and 19 diatom taxa in the other three stations to calculate the diatom index scores of the four stations to determine the trophic status and water

quality of the Batlama Stream. While the lowest value of the TDI was recorded in station 3 as 49.8, the station has the lowest BDI value was station 4. Both values of the indices indicate oligo-mesotrophic features. TDI and BDI values of the four stations ranged between 50–55 and 14.7–15.4 respectively (Table 2). However, mean values of TDI (53.5) and BDI (15.1) indicated that the trophic structure of Batlama stream is mesotrophic. Similarly, according to PTI and S values, the studied site was moderately polluted (β -mesosaprobity). The present results coincide with the conclusions of Köster and Hübener [46], who suggested that the best method for monitoring freshwater by diatoms is the combined application of saprobity and trophic indices.

CONCLUSION

Agriculture, livestock activities and domestic waste water into the Batlama stream, are factors that increase of water pollution. The factors are decreased of density of epilithic algae. The present study results demonstrated that epilithic algal composition is distributed gradients of environmental factors. Temperature and rain are more important factor in explaining the seasonal variation of epilithic algae of Batlama stream. More research is needed to analyse the causes of the observed variation in the nutrient status and biomass of benthic algae in Batlama stream.

According to the diversity values, one can conclude that Batlama stream is on eutrophic level, however, the species

Table 2. Diatom indice values of the four stations in Batlama Stream derived from TDI, BDI, PTI and S

	kind of index	Station 1	Station 2	Station 3	Station 4	Average
Trophic index	TDI	53.8	55.3	49.8	55.3	53.5
	BDI	15.3	15	15.4	14.7	15.1
Pollution index	PTI	2.5	2.5	2.4	2.4	2.5
	S	2.3	2.3	2.4	2.4	2.4

composition of the stream, TDI, BDI, and chl-a values indicate that the stream is mesotrophic. So, diversity indices calculated using epilithic diatoms did not exactly represent the trophic status of the stream. Consequently, based on all these results, it can be said that Batlama stream does not yet reach the level of pollution and having mesotrophic characteristics as a trophic structure.

REFERENCES

- Pan Y, Stevenson RJ, Hill BH, Kaufmann PR, Herlihy AT. Spatial patterns and ecological determinants of benthic algal assemblages, stream slope, TP, TN and riparian canopy coverage. *J. of Phycology* 35 (1999) 460–468. DOI: 10.1046/j.1529-8817.1999.3530460.x
- Hill W, Dimick SM. Effects of riparian leaf dynamics on periphyton photosynthesis and light utilization efficiency. *Freshw. Biol.* 47 (2002) 1245–1256. DOI: 10.1046/j.1365-2427.2002.00837.x
- Lin HJ, Peng TR, Cheng IC, Chen LW, Kuo MH, Tzeng CS. A trophic model of the subtropical headwater stream habitat of the Formosan landlocked salmon, *Oncorhynchus formosanus*. *Aquatic Biol.* 17 (2012) 269–283. DOI: https://doi.org/10.3354/ab00481
- Quinn JM, Cooper AB, Stroud MJ, Burrell GP. Shade effects on stream periphyton and invertebrates: an experiment in streamside channels. *N. Z. J. of Mar. and Freshw.* 31 (1997) 665–683. DOI: 10.1080/00288330.1997.9516797
- Soininen J, Könönen K. Comparative study of monitoring South-Finnish rivers and streams using macroinvertebrate and benthic diatom community structure. *Aquatic Ecology* 38 (2004) 63–75. DOI:10.1023/B:AECO.0000021004.06965.bd
- Bowman MF, Chambers PA, Schindler DW. Epilithic algal abundance in relation to anthropogenic changes in phosphorus bioavailability and limitation in mountain rivers. *Canadian J. Fisheries Aquatic Sci.* 62(1) (2005) 174–184. DOI: 10.1139/f04-244
- Yıldız K. Investigations on algae communities of Meram stream, section 3–Algae living on sediment. *J. of Nat. Sci. A2*, 9(2) (1985) 428–434 (in Turkish).
- Kılınc S, Sivacı ER. A study on the past and present diatom flora of two alkaline lakes. *Turkish J. of Botany* 25 (2001) 373–378.
- Maraşlıoğlu F, Soylu EN, Gönüloğlu A. A study of the composition and seasonal variation of the epilithic diatoms of Lake Ladik (Samsun, Turkey). *International J. on Algae* 7(1) (2005) 58–70. DOI: 10.1615/InterJAlgae.v7.i1.40
- Maraşlıoğlu F, Soylu EN, Gönüloğlu A. Seasonal Variation and Occurrence of Epiphytic Diatom Assemblages on Mats of *Cladophora glomerata* in Lake Ladik, Samsun, Turkey. *Cryptogamie Algologie* 28(4) (2007) 373–384.
- Sivacı ER, Pabuççu K. Epilithic and epilithic diatoms of the Balıklı Spa in central Anatolia, Turkey. *J. of Freshw. Ecology* 22 (2007) 145–146. DOI: 10.1080/02705060.2007.9664154
- Soylu EN, Maraşlıoğlu F, Gönüloğlu A. Epilithic algae and seasonal variation of Gıcı Lake (Samsun–Bafra). *J. of Fisheries Sciences* 4(4) (2010) 437–445.
- Çiçek NL, Kalyoncu H., Akköz C., Ertan Ö. Seasonal Distribution and Species of Epilithic Algae in Darıören and Isparta Stream (Isparta–Turkey). *J. of Fisheries Sciences* 4(1) (2010) 78–90.
- Çolak-Sabancı F. Relationship of Epilithic Diatom Communities to Environmental Variables in Homa Lagoon (İzmir, Turkey). *Aquatic Biol.* 13 (2011) 233–241. DOI: 10.3354/ab00367
- Maraşlıoğlu F, Soylu EN, Gönüloğlu A. Seasonal Variations and Occurrence of Algal Turf Community in Lake Ladik (Turkey). *J. of Environmental Biol.* 34 (2013) 107–111.
- Ongun–Sevindik T, Küçük F. Benthic Diatoms as Indicators of Water Quality in the Acarlar Floodplain Forest (Northern Turkey). *Fresenius Environmental Bull.* 25(10) (2016) 4013–4025.
- Kalyoncu H, Lerzan–Çiçek N, Cengiz Akköz C, Yorulmaz B. Comparative performance of diatom indices in aquatic pollution assessment. *African J. of Agricultural Research* 4 (10) (2009) 1032–1040.
- Tokatlı C.. Use of Some Diatom Indices for Evaluating Water Quality: Sample of Gürleyik Stream (Eskişehir). *Dumlupınar University, J. of Nat. Sci.* 29 (2012) 21–28.
- Solak CN, Fehér G, Barlas M, Pabuççu K. 2007. Use of epilithic diatoms to evaluate water quality of Akçay Stream (Büyük Menderes River) in Mugla/Turkey. *Large Rivers* 17 (3–4) (2007) 327–338. DOI: 10.1127/lr/17/2007/327
- Zelinka M, Marvan P. Zur Prazisierung derbiologischen Klassifikation des Reinheit fliessender Gewässer. *Arch. für Hydrobiologie* 57 (1961) 389–407.
- Round FE. An investigation of two benthic algal communities in Malharm Tarn, Yorkshire. *J. of Ecology* 41 (1953) 97–174. DOI: 10.2307/2257108
- Sladeckova A. Limnological investigation methods for the perifiton (Aufwuch) community. *Botanical Review* 28 (1962) 286–350.
- John DM, Whitton BA, Brook AJ. *The Freshwater Algal Flora of the British Isles: An identification guide to freshwater and terrestrial algae. The Natural History Museum and The British Phycological Society, Cambridge University Press,*

- Cambridge, 2003.
24. Krammer K, Lange-Bertalot H. Sübwasserflora von Mitteleuropa. Bacillariophyceae, 3. Teil. Centrales, Fragillariaceae, Eunoticeae. Gustav Fischer Verlag, Stuttgart, 1991a.
 25. Krammer K, Lange-Bertalot H. Sübwasserflora von Mitteleuropa. Bacillariophyceae, 4. Teil. Achnantheaceae, Kritische Ergänzungen zu Navicula (Lineolate) und Gomphonema Gesamtliterat. Gustav Fischer Verlag, Stuttgart, 1991b.
 26. Krammer K, Lange-Bertalot H. Sübwasserflora von Mitteleuropa. Bacillariophyceae, 1. Teil. Naviculaceae. Spectrum Acad. Verlag, Berlin, 1999a.
 27. Krammer K, Lange-Bertalot H. Sübwasserflora von Mitteleuropa. Bacillariophyceae, 2. Teil. Bacillariaceae, Epithemiaceae, Surirellaceae. Spectrum Academischer Verlag, Berlin, 1999b.
 28. Guiry MD, Guiry GM. AlgaeBase. World-wide electronic publication. Galway: National University of Ireland, 2016. Retrieved from <http://www.algaebase.org>.
 29. Brummitt RK, Powell CE. Authors of plant names. A list of authors of scientific names of plants, with recommended standart forms of their names, including abbreviations, Royal Botanic Gardens, Kew, 1992.
 30. Shannon CE, Weaver W. The Mathematical Theory of Communication. The University of Illinois Press, 1949.
 31. Kelly MG, Whitton BA. The trophic diatom index: A new index for monitoring eutrophication in rivers. J. of Appl. Phycology 7 (1995) 433-444. DOI: 10.1007/BF00003802
 32. Lenoir A, Coste M. Development of a practical diatom index of overall water quality applicable to the French National Water Board network, in: Whitton BA and Rott E (eds.) Use of Algae for Monitoring Rivers II. Institut für Botanik, Universität Innsbruck. pp. 29-43, 1996.
 33. Pantle R, Buck H. Die biologische Überwachung der Gewässer und die Darstellung der Ergebnisse (Biological monitoring of water bodies and the presentation of results). Gas -und Wasserfach 96 (1955) 604-618.
 34. Muscio C. The diatom pollution tolerance index: assigning tolerance values. Water Protection & Development Review Department. Environmental Resource Management, 2002.
 35. Strickland JDH, Parsons TR. A Pratical Handbook of Seawater Analysis. Fisheries Research Board of Canada, 1972.
 36. Sienkiewicz E. Limnological record inferred from diatoms in sediments of Lake Skaliska (north-eastern Poland). Acta Palaeobotanica 53(1) (2013) 99-104. DOI: 10.2478/acpa-2013-0007
 37. Gönüloğlu A, Öztürk M, Öztürk M. A Check-list of the Freshwater Algae of Turkey. Ondokuz Mayıs University, Faculty of Arts and Science, J. of Sci. 7(1) (1996) 8-46 (in Turkish).
 38. Gönüloğlu A. 2017. Turkishalgae Electronic Publication, Samsun, Turkey. <http://turkiyealgleri.omu.edu.tr>. (searched on 07 February 2017)
 39. Sivacı R, Dere Ş. Seasonal Changes of Epilithic (Aksaray-Ihlara) Diatom of Melendiz Stream and Effect on Total Organisms of Water Flow. Ekoloji 16(6) (2007) 29-36 (in Turkish).
 40. Yavuz O, Çetin K. Seasonal Variation and Algae on Pelagic Region of Cip Stream (Elazığ-Turkey). Firat University, J. of Sci. and Eng. 12(2) (2000) 25-39 (in Turkish).
 41. Wetzel RG. Limnology. Michigan State University. Academic Press, 2001.
 42. DSI. Water Quality and Dam Lakes which Provide Drinking Water of Ankara. DSI General Directory Research Reports, Ankara, 1998.
 43. Round FE. The Ecology of Algae. Cambridge University Press, Cambridge, 1981.
 44. Vinebrooke RD. Abiotic and Biotic Regulation of Periphyton in Recovering Acidified Lakes. J. of the N. Am. Benthological Soc. 15 (1996) 318-331. DOI: 10.2307/1467280
 45. Moses BS. The status of the fisheries downstream in river Niger the Kainji Dam, in: Proceedings of International Conference of Kainji Lake and River Basins Development in Africa. New Bussa, Nigeria, Kainji Lake Research Institute pp. 612, 1979.
 46. Köster D, Hübener T. Application of Diatom Indices in a planted ditch constructed for tertiary sewage treatment in Schwaan, Germany. Internationale Revue der Gesamten. Hidrobiologie 86 (2001) 241-252.

Evaluation of Chitosan /Organoclay Composite as Bone Tissue Engineering Scaffold

Aysel Koç Demir

Ankara University, Department of Biochemistry, Ankara, TURKEY

ABSTRACT

In this study, a scaffold composed of chitosan (C) and organoclay (OC) was prepared by utilizing freeze-drying method. The composition of resulting composite scaffold was evaluated using FTIR and SEM. The in vivo cytocompatibility of the composite was evaluated in vivo, by seeding MC3T3-E1 cells on composite scaffolds. In-vitro cell viability and proliferation were investigated using the MTT assay, while cell-scaffold constructs were evaluated using scanning electron microscopy. Preliminary in vivo experiments were also performed to evaluate tissue compatibility and ectopic bone-forming potential of C/OC composite scaffolds with MC3T3-E1 cells. The findings suggest that C/OC construct supported the proliferation of MC3T3-E1 cells, presented histobiocompatibility and promoted formation of calcified matrix. Based on the results, we conclude that the characterized C/OC composite system may have potential for use in bone tissue engineering applications.

Keywords:

Bone tissue engineering; Chitosan; Organoclay; Composite scaffold; Organically modified calcium-smectite

INTRODUCTION

The important stage of tissue engineering is choosing the best material to create the most suitable template. Scaffolds should be porous, biocompatible, biodegradable and have sufficient mechanical properties. Furthermore, they also should induce cellular attachment, proliferation and differentiation.

A variety of natural and synthetic polymers have been widely used in tissue engineering studies to create the best tissue scaffold. Natural polymers have been receiving a lot of attention in recent years [1,2]. Among numerous natural polymers, chitosan is considered as a promising material in the synthesis of scaffolds for bone tissue engineering. The characteristic properties which make chitosan useful in tissue engineering applications are its similarity to glycosaminoglycans (GAGs), hydrophilicity, biocompatibility and biodegradability [3,4]. Chitosan can be cast in different forms such as sponges, foams, gels, fibers and so on [5]. Thanks to these properties, it facilitates the attachment of cells and promote bone growth. Despite its advantageous structure, because of the unfavorable mechanical property

and bioactivity of chitosan, it is inconvenient to use it as bone tissue templates as its low mechanical strength cannot match the demand of bone tissue applications in many cases [6,7]. In this regard, incorporation of chitosan with a filler material is an effective way to improve its mechanical properties and biological activity [8]. The combination of polymers and inorganic fillers seem to be a promising approach, because they exhibit remarkable improvement in material properties compared to the free polymers [9].

As a filler, clay minerals are favorable candidates for tissue engineering studies due to their excellent properties such as good biocompatibility, high cation exchange capacity and promise for controlled release [10]. From the economical point of view, they are relatively low cost materials due to their abundance in nature. In order to expand the interlayer distance of clay minerals, they can be modified with organic substances. The obtaining structure is called as 'organo-clay'. The resulting structure can be incorporated with organic materials much easier than that of pure clay minerals.

Article History:

Received: 2017/02/07

Accepted: 2017/04/10

Online: 2017/06/30

Correspondence to: Aysel Koç Demir,
Ankara University, Department of
Biochemistry, Ankara, TURKEY
Tel: +90 (312) 212-6720 (1037)
Fax: +90 (364) 223-2395
E-Mail: aykoc@science.ankara.edu.tr

The objectives of this work were to report the fabrication and characterization of the developed porous C-based biocomposite with improved mechanical properties and examine the feasibility of using the obtained material as bone tissue engineered scaffold by conducting cell culture study.

MATERIALS AND METHODS

Chitosan powder ($M_r = \sim 400000$; degree of deacetylation $>85\%$) was purchased from Fluka Chemical Company (Milwaukee, WI). Anilinium modified calcium-smectite (127 meq of CEC/100g) was gifted by Dr. Sibel Uzun. 3-(4,5-dimethylthiasol-2-yl)-2,5-diphenyltetrazolium bromide (MTT) was supplied from Sigma Aldrich Company except otherwise stated.

2 % chitosan in aqueous acetic acid solution was prepared and organically modified smectite powder was added under continuous mixing and stirring for 12 h [C/OC, 9/1 (w/w)]. Subsequently, the obtained mixture was casted on cell culture dishes and stored in a freezer at -40°C for 12 h. The samples were transferred into a freeze dryer to obtain a porous structure (Alpha 1-4 LD, Christ, Osterode am Harz, Germany) for 24 h and then neutralized by immersion in a 1 M NaOH solution. The samples were rinsed three times in double distilled water and lyophilised again. Finally, the samples were cut into $4 \times 4 \times 4$ mm cubes using surgical blade. The structural characterization of C/OC sponges was carried out by means of IR spectroscopy and SEM.

MC3T3-E1 cells were cultured in the α -Modified Eagle's minimal essential medium (α -MEM), supplemented with 10 % fetal bovine serum (FBS), and 1% penicillin-streptomycin (standart medium; SM) acquired from Sigma Chemical Company. Cells at $\sim 90\%$ confluency were digested using trypsin/EDTA. Cells were suspended in culture medium ($1.0 \times 10^7/\text{mL}$) and the cells were seeded onto each sponge. The loaded-scaffolds were agitated at 37°C for 30 min on a shaker at low speed to allow cells to adhere and then they were transferred in a new culture plate. The culture was maintained in osteogenic medium (SM supplemented 10 nM dexamethasone, 50 mg/mL L-ascorbic acid and 10 mM β -glycerophosphate) at 37°C in 5% CO_2 humidified atmosphere for up to 4 weeks.

Cell morphology on the sponges was inspected by SEM. The samples were washed with PBS and fixed in 2.5% glutaraldehyde solution for 12 h at 4°C . After fixation, the samples were rinsed twice in PBS and dehydrated with increasing concentrations of ethanol in water. The air-dried samples were sputter coated with palladium and analyzed by SEM (400F Field Emission, QUANTA, Hillsboro, OR).

MTT was used to assess cell viability. This assay is ba-

sed on mitochondrial redox reaction. A pale yellow MTT reagent is reduced to a dark blue formazan crystal by mitochondrial dehydrogenase activity of viable cells [11]. Briefly, MTT solution was prepared at 5 mg/mL in PBS and required amount of MTT solution was added to each well containing cell-sponge constructs. After an incubation of 4 h at 37°C and 5% CO_2 to allow MTT formazan formation. The reduced insoluble formazan crystals were observed under an inverted microscope (Nikon TS 100, Tokyo, Japan). After removing the supernatant, the formazan crystals were solubilized in 0.1 N HCl. The absorbance intensity was measured using a microplate reader at 570 nm.

The cell loaded C/OC composite sponges were implanted into the epigastric fasciovascular flap of rats under aseptic conditions to investigate their tissue compatibility and ectopic bone forming capacity. Twelve adult male Wistar rats weighing 200-300 g were used at predetermined time points. All procedures were performed according to the standards of international regulations. The cell loaded-sponges were maintained in a humidified incubator at 37°C with 5% CO_2 overnight before implantation. The samples were implanted into fasciovascular flaps through a 2-3 cm long mid-line incision (Cell free C/OC sponges used as controls) following anaesthetization with Avertin (300 mg/kg; 1.25%). Animals were sacrificed at days 7, 14, and 28 and the implants with surrounding tissue were harvested carefully from the epigastric area together. All the explants were fixed with 2.5% glutaraldehyde for 10 min and then immersed in 0.1 M potassium phosphate buffer (pH 7.4) containing 15% sucrose for 15 min. Finally, the specimens were frozen after embedding in tissue freezing medium (Tissue-Tek, Sakura Finetek, The Netherlands) for 30 minutes and frozen at -80°C . The tissue blocks were cut into $5 \mu\text{m}$ sections using a cryostat (Leica CM 1900, Wetzlar, Germany) and stained with hematoxyline and eosin (H&E) and von Kossa for histological evaluation.

RESULTS AND DISCUSSION

Structural evaluation of composite scaffold

FTIR was used to determine the chemical interactions between C, OC and C/OC composite scaffolds. The spectra of pure chitosan exhibits characteristic peaks at 3424 cm^{-1} (O-H stretch), 2923 cm^{-1} (C-H stretch), 1637 cm^{-1} (amide I) and 1071 cm^{-1} (C-O stretch) (Fig. 1). OC exhibits its characteristic bands at 3626 cm^{-1} (O-H stretch), 2926 and 1637 cm^{-1} (N-H stretch) and 1036 cm^{-1} (Si-O stretch). The spectrums of C/OC includes all the specific absorption peaks of C and OC, indicating that C/OC scaffold was produced successfully.

Fabrication of three-dimensional porous scaffolds with higher porosities having interconnected pore structure is really important, as these properties have an impact

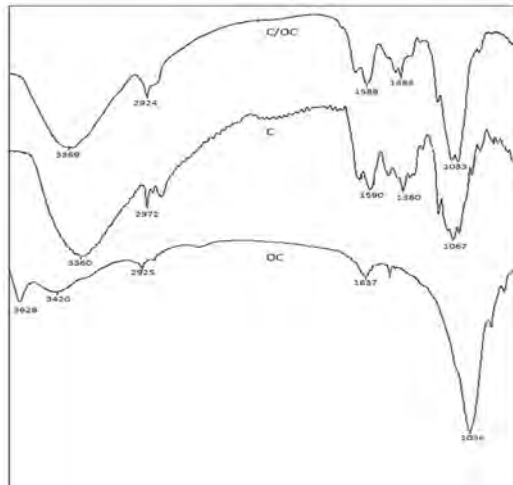


Figure 1. FTIR spectra of C, OC and C/OC composite scaffold.

on cellular behaviour like cell attachment, proliferation and differentiation [12]. The porous structure and surface morphology of the scaffolds were studied using SEM. SEM micrographs indicated that the composite scaffold obtained by freeze drying method had highly heterogeneous porous structure with interconnected architecture. The SEM image also showed that the pore size of composite scaffold was about 50-200 μm which allow cell-cell communication, cell infiltration, growth, and also diffusion of nutrients (Fig. 2) [13].

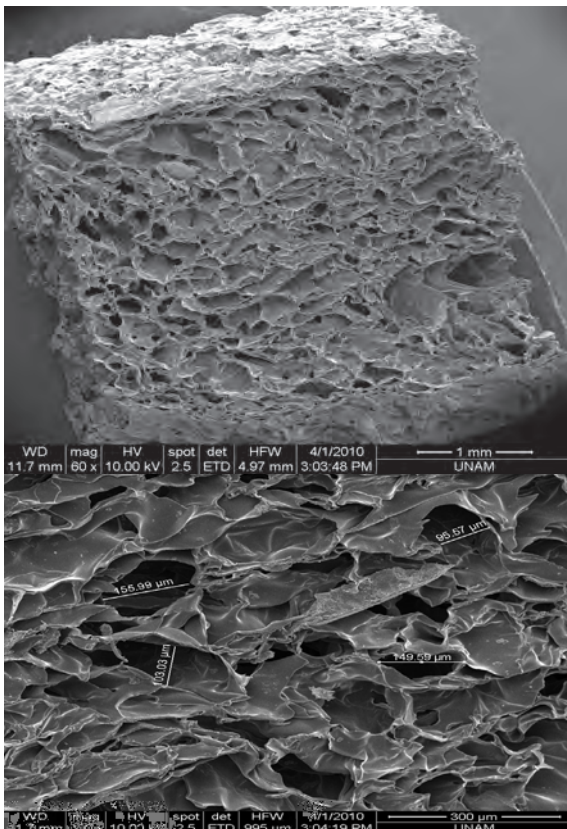


Figure 2. SEM images of acellular composite scaffold.

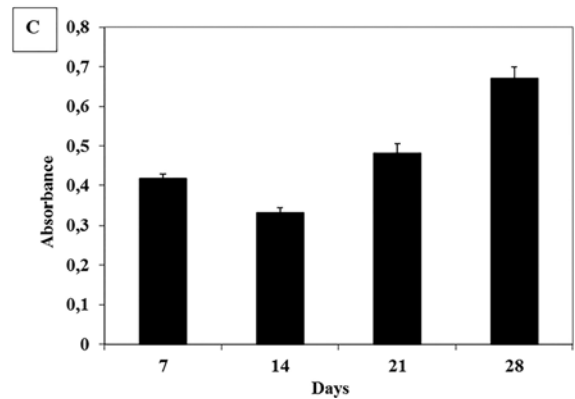
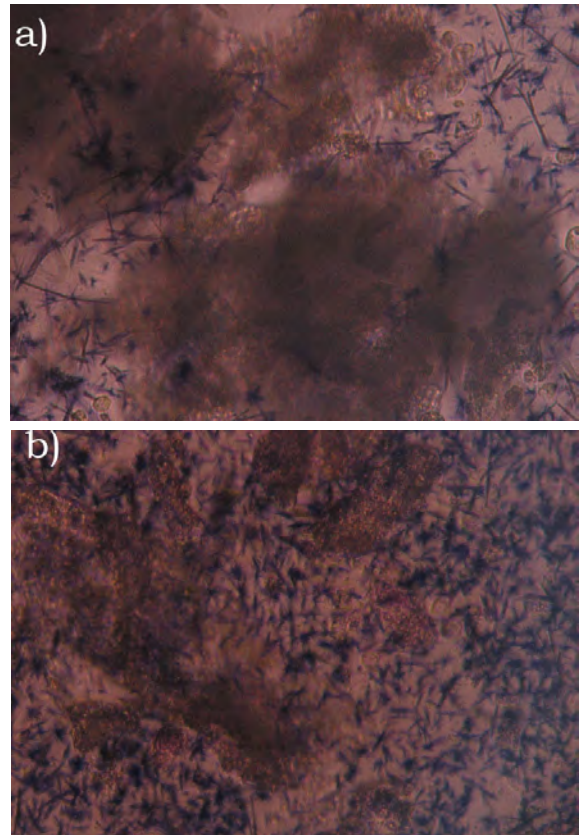


Figure 3. MTT formazan crystals inside sponge pores after 14 (A) and 28 (B) days. Mitochondrial activity of cells cultured on the composite scaffolds (C) (n=3).

Cell viability and proliferation on composite scaffolds

The assessment of viability and proliferation of cells on the material is very important for the determination of the feasibility of materials in tissue engineering applications. There are different methods available to investigate this feature, such as MTT and XTT. In this study, MTT assay was performed to determine the viability of cells on the scaffolds. Firstly, the MTT activity of the seeded cells was assessed qualitatively. Phase-contrast imaging showed that the formazan crystals were formed and clearly visible (Fig. 3 (A, B)). The intensity of formazan

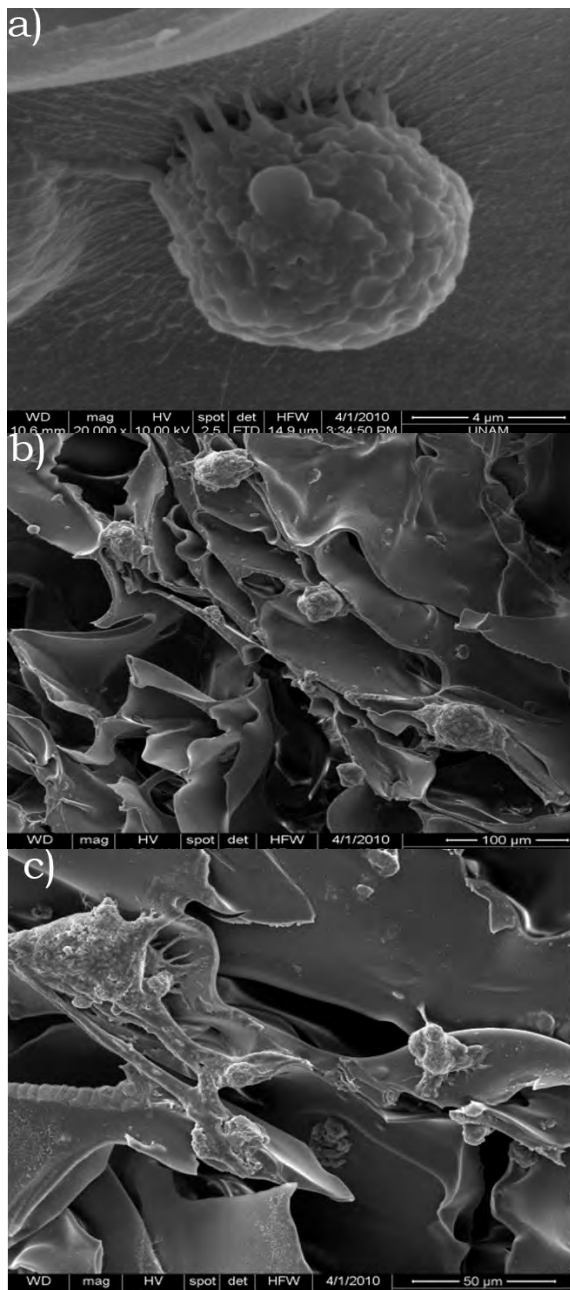


Figure 4. SEM micrographs of cell-loaded C/OC composite scaffolds at days 7 (A, B), and 14 (C).

crystals increased with culturing time. Moreover, the distribution of crystals were homogenous, indicating that the distribution of cells inside the scaffold was uniform. Quantitative data obtained spectrophotometrically revealed that MTT activity of MC3T3-E1 cultured on the scaffolds gradually increased from day 14 to day 28, indicating that cells were viable and proliferated within the scaffolds (Fig. 3C).

SEM was performed to evaluate the attachment and proliferation of cells on the composite scaffolds (Figure 4). SEM observations demonstrated that cells were attached to the scaffold surface in rounded shape on day 7 (Fig.

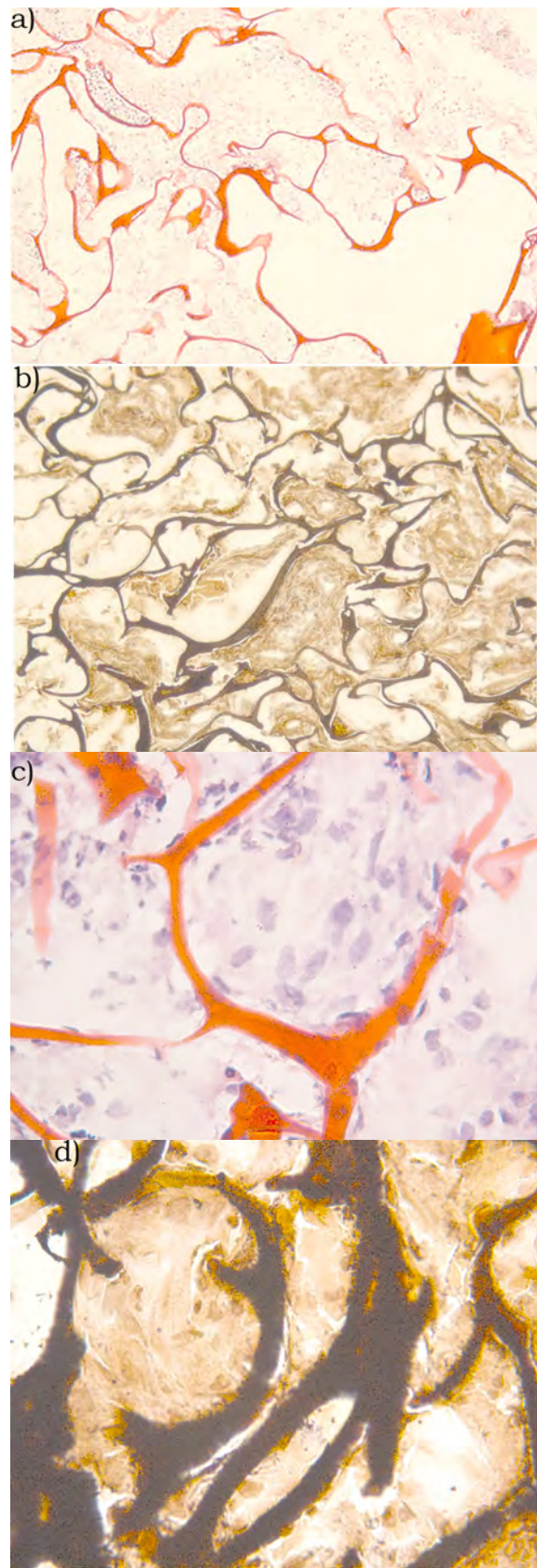


Figure 5. H&E staining of cell-seeded C/OC scaffolds at days 14 (A) and 28 (C); von Kossa staining of cell-seeded C/OC scaffolds at days 14 (B) and 28 (D).

4A). This image also confirmed that cells migrated and proliferated on the composite scaffold with time, and also the cell-pseudopodia have connected with the matrices, indicating that the developed composite scaffold shows no toxic effect to the cells and it is a convenient template as bone tissue engineering scaffold. SEM micrographs also revealed that the composite scaffold preserved the porous structure during the experimental periods.

In vivo findings

In vivo experiment was performed to determine the effect of the cell-loaded scaffolds on the formation of ectopic bone-like tissue. Although acute inflammatory reaction was observed at the first week post-implantation, cell-loaded scaffold did not cause a significant reaction, indicating that the material was biocompatible. The H&E staining was performed to document the formation of new tissue. Histological observations confirmed that cells attached and proliferated on the scaffold and bone-like tissue was formed by the time.

The cell-loaded scaffold was filled with fibrous connective tissues (Fig. 5 A, C). Von Kossa or Alizarin Red S are generally used to detect bone tissue development [13]. In this study, in vivo differentiation and calcification of MC3T3-E1 cells were evaluated by von Kossa staining. Von Kossa staining was performed on the 14-day and 28-day specimens. The obtained light microscopy images show the presence of calcium produced by the cells. Von Kossa was visible starting from the second week of implantation and gradually increased up to 4 weeks. The gained data indicates that the scaffold are able to provide an osteogenic environment to MC3T3-E1 cells and hence it can be used as bone tissue engineering scaffold.

CONCLUSION

Various composite materials have been widely investigated to create an ideal hard tissue template. In this study, the C/OC composite scaffold was successfully produced and characterized. The findings of this study suggest that obtained scaffold provides a suitable environment to MC3T3-E1 cells. Owing to the biocompatibility and sufficient porosity of the developed organic-inorganic composite system which supports cell attachment and proliferation, we conclude that it can be a promising template for bone engineering applications.

ACKNOWLEDGMENTS

I wish to express my deepest and sincere gratitude to Professors Y. Murat Elçin and A. Eser Elçin for their guidance, and for giving me the opportunity to completion of this study at ElcinLab. I also thank Dr. Sibel Uzun for providing me the organoclay.

REFERENCES

1. Wu S, Liu X, Yeung KW, Liu C, Yang X. Biomimetic porous scaffolds for bone tissue engineering, *Mater. Sci. Eng. R. Rep.* 80 (2014) 1-36.
2. Levengood SKL, Zhang M. Chitosan-based scaffolds for bone tissue engineering, *J. Mater. Chem. B* 2, (2014) 3161-3184.
3. Afshar HA, Ghaee A. Preparation of aminated chitosan/alginate scaffold containing halloysite nanotubes with improved cell attachment. *Carbohydrate Polymers* 151 (2016) 1120-1131.
4. Kumar MNRL. A review of chitin and chitosan applications. *Reactive and Functional Polymers* 46, (2000) 1-27.
5. Hu Q, Li B, Wang M, Shen J. Preparation and characterization of biodegradable chitosan/hydroxyapatite nanocomposite rods via in situ hybridization: a potential material as internal fixation of bone fracture. *Biomaterials* 25 (2004) 779-85.
6. Kumar RL, Narayan AK, Dhivya S, Chawla A, Saravanan S, and Selvamurugan N. A review of chitosan and its derivatives in bone tissue engineering. *Carbohydrate Polymers* 151 (2016) 172-188.
7. Puppi D, Chiellini F, Piras AM, Chiellini E. Polymeric materials for bone and cartilage repair. *Progress in Polymer Science* 35 (2010) 403-440.
8. Kai D, Prabhakaran MP, Stahl B, Eblenkamp M, Wintermantel E, Ramakrishna S. Mechanical properties and in vitro behavior of nanofiber-hydrogel composites for tissue engineering applications. *Nanotechnology* 23 (2012) 1-10.
9. Rezwani K, Chen QZ, Blaker JJ, Boccaccini AR. Biodegradable and bioactive porous polymer/inorganic composite scaffolds for bone tissue engineering. *Biomaterials* 27 (2006) 3413-3431.
10. Choy JH, Choi SJ, Oh JM, Park T. Clay minerals and layered double hydroxides for novel biological applications *Applied Clay Science* 36 (2007) 122-132.
11. Mosmann T. Rapid colorimetric assay for cellular growth and survival: Application to proliferation and cytotoxicity assays. *Journal of Immunological Methods* 65 (1983) 55-63.
12. Loh QL and Choong C. Three-dimensional scaffolds for tissue engineering applications: Role of porosity and pore size. *Tissue Eng Part B Rev.* 19(6) (2013) 485-502.
13. Khan F, Tanaka M, Rafi Ahmad S. Fabrication of polymeric biomaterials: a strategy for tissue engineering and medical devices. *J. Mater. Chem. B* 3 (2015) 8224-8249.
14. Christenson RH. Biochemical markers of bone metabolism: an overview. *Clin Biochem.* 30 (1997) 573-593.

Quantized Conductance Measurement System for Liquids and Application to DNA Solution

Yavuz Öztürk¹, Büşra Yıldırım², Koray Şekerin² and Alper Bayram³

¹ Department of Electrical and Electronics Engineering, Ege University, Izmir 35100, TURKEY

² Department of Electrical and Electronics Engineering, Boğaziçi University, Istanbul 34342, TURKEY

³ Department of Material Science and Engineering, Ege University, Izmir 35100, TURKEY

ABSTRACT

In this study, a system for undergraduate and graduate laboratories was designed in order to investigate quantized conductivity behavior of solutions. The quantized conductivity of the DNA solution was examined by using the designed system. The quantized conductivity peculiarity of DNA solution was observed. The same quantized feature couldn't be reached after repeated experiments for buffer solution, mutated DNA solutions. It is concluded that it is possible to differentiate similar kind of solution by measuring the quantized conductance behavior.

Keywords:

Quantized conductivity; Healthy DNA; Mutated DNA; DNA biosensor.

INTRODUCTION

Nanoscale researches have gained a great interest in recent years. Moreover, there is a need of students and researchers for the understanding and developing new ways with research of nanoscale [1]. One of the interesting research subjects in nanoscale is the quantized conduction [2]. There are several simple experiments related to nanoscale conduction [3,4]. Quantized conductivity was shown with these very simple systems by using the formation of nano size contacts with mercury [3] or gold wire [4].

On the other hand, several researches were conducted to investigate electronic properties of DNA molecules which can be defined as a continuous stack of aromatic heterocycles, the base pairs, which extends down the helical axis [5-7]. In literature, there is large dispersion of DNA conductance values. The results of several experiments show that DNA could be conducting, insulating or semiconducting [8] depending on the DNA may be in [9] or ambient conditions [10], or on an inorganic substrate [11]. It is known that interpretation of experimental studies and the results attained on DNA conductivity can be difficult. Measurement of charge transport mechanism in DNA solution being complicated because of many factors such as electrode type, medium of DNA [12].

Our work has potential to contribute to the studies on electrical conductivity of DNA based solutions with the advantage of its simplicity. In our study, quantized conductivity measurements conducted for the solutions of DNA, and mutated DNA by developing the system that was presented by Tolley et.al. [4]. Most important innovation which comes with our system is its ability to investigate quantized conductivity of solutions by using a relatively simple setup.

MATERIALS AND METHODS

The designed system has three main parts namely flexible plate with gold wire in a cuvette, a translation stage and an electronic circuit with computer interface (figure 1). Firstly, 99.99%-pure and 100 µm diameter gold wire prepared on a flexible plate covered with insulator band. The middle point of the wire was fractured to control the breaking point. Because of the applied force from the translation stage's tip the curve of plate can be controlled. The wire can be broken or reconnected by controlling the bend of the plate. It can be seen without applied force in figure 2a and with applied force in figure 2b. As a result, it is possible to create nano contacts during this breaking or reconnecting operation at the fractured part of wire [4].

Article History:

Received: 2017/02/14

Accepted: 2017/03/14

Online: 2017/06/30

Correspondence to: Alper Bayram, Ege University, Department of Material Science and Engineering, Izmir, TURKEY.

Tel: +90 (232) 311-5246

Fax: +90 (232) 311-5243

email: aalperbayram@gmail.com

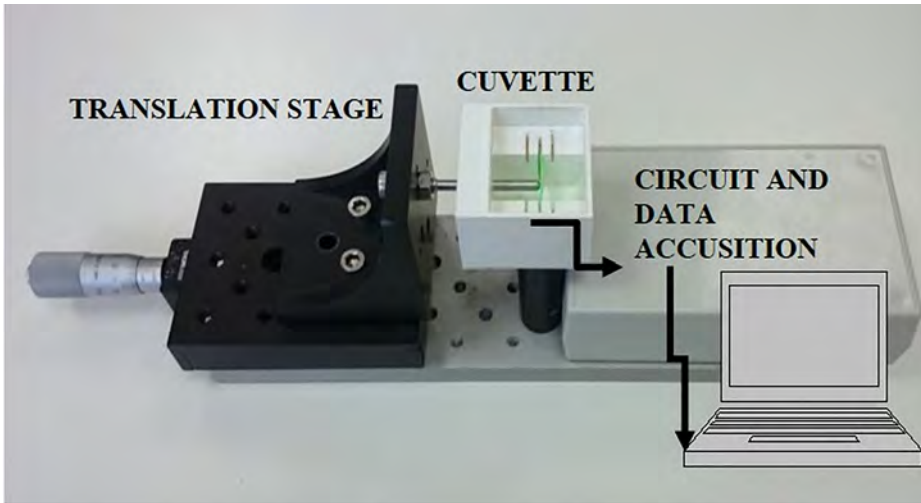


Figure 1. Quantized conduction measurement system.

Since the proposed system will be work in liquid medium, the gold wire was insulated to make sure that only fractured part will be in contact with the environment. The cuvette was printed with 3D printer to hold the flexible plate and liquid. After that, Thorlabs PT1/M 25 mm model translation stage extension connected to flexible plate. The cuvette system was sealed to prevent any liquid leakage during the measurement of solutions.

Resistance changes of gold wire were measured via the circuit presented in figure 3a. The circuit was designed to ensure that the voltage applied to DNA molecules in solutions is in millivolt range. For this reason, a resistor of 290 kΩ (R_{ext}) was connected in series to the resistance of 10 kΩ (R_p) and the gold wire. A 1.5 V battery ($V_{battery}$) was utilized to drive the circuit. Potential difference between the golden wire ends measured with DAQ, LabJack U3-LV unit connected to a computer. When the gold wire breaks, there will be no contact and the measured potential difference will be equal to the voltage on the 10 kΩ resistance. When the wire is broken, the micrometer could be turned to an opposite direction to provide reconnection. During both processes nano contacts occurs at the fractured point of the gold wire. The quantized conduction mechanism can be explained as a result of these nano sized atomic contacts..

Conduction or resistance values of gold wire can be

calculated by using the quantized conduction equation $G_0(n) = (2e^2/h) n$ where $n=1, 2, 3, \dots$ is an integer value. The potential difference between the ends of the gold wire ($V_{labjack}$) was formulated as in equation 1.

$$R_{gw} = \left\{ \begin{array}{l} \text{Open circuit} \leftarrow \text{Broken} \\ 1/G_0(n) \leftarrow \text{Atomic contact} \\ \text{Short circuit} \leftarrow \text{Intact} \end{array} \right\}$$

$$V_{labjack} = \left\{ \begin{array}{l} \frac{V_{battery} R_p}{R_{ext} + R_p} = 54 \text{ mV} \leftarrow \text{Broken (open circuit)} \\ \frac{V_{battery} (R_p // R_{gw})}{R_{ext} + (R_p // R_{gw})} \leftarrow \text{Atomic contact} \\ 0 \text{ V} \leftarrow \text{Intact (short circuit)} \end{array} \right\} \quad (1)$$

Where R_{gw} and $(R_p // R_{gw})$ is the resistance of the gold wire and equivalent resistance value of parallel connected resistances respectively. Calculated values of $V_{labjack}$ with respect to the quantum number n were plotted in figure 3b. According to the circuit described in figure 3, in the broken condition of gold wire the potential difference was calculated as 54 mV. As expected, the gold wire starts to behave like short circuit and the voltage value converges to the 0 V as the quantum number n increases.

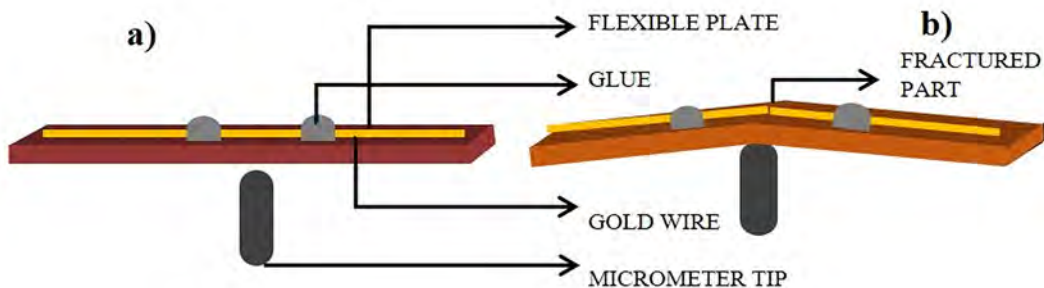


Figure 2. Flexible plates with gold wire (a) before bending (reconnected) and (b) after bending (broken).

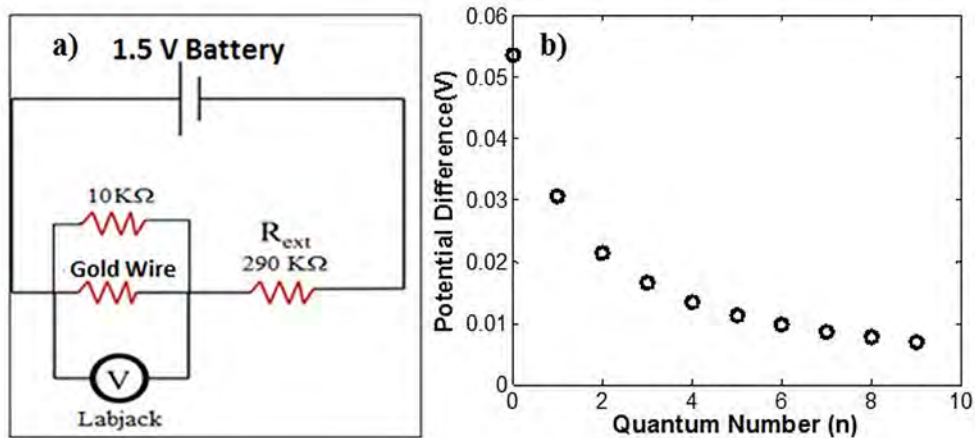


Figure 3. (a) The circuit diagram (b) calculated voltage values of $V_{labjack}$

Table 1. Solutions for liquid applications.

Analytes:	Concentration of solution:
DNA - Pure water solution	2, 1, 0.5, 0.25 mg/mL
DNA - Phosphor buffer solution (pH: 7.4)	1 mg/mL
Mismatched DNA - Phosphor buffer solution (pH: 7.4)	1 mg/mL
Albumin - Pure Water	1 mg/mL
Brine solution	1 mg/mL
Acetic acid (liquid form)	1 mg/mL

Several solutions were prepared given in Table 1 to test the system. All solutions were prepared at the Ege University Science Faculty Department of Biochemistry. Herring sperm DNA (D3159) was purchased from Sigma Aldrich while the 14-mer DNA oligonucleotides as mutated DNA were obtained from Genset Oligos.

RESULTS AND DISCUSSION

Our initial measurements were taken without any liquid to ensure that our setup working as described in Tolley et.al. [4]. Measured levels of the quantized

conductance were presented in the figure 4. Values up to 0.4 seconds were measured in the transition from broken state to contact state. The data given after 0.4 seconds was collected while the wire was breaking. Measured quantize levels were named according to the calculated values by using the equation 1.

Experiments with solution were conducted after the observation of quantized levels in control experiments. Wire left as an open circuit (broken state) just after the observation of quantized levels. This will ensure that distance between the broken wire ends at fractured point will be around nm range without any physical contact. DNA-distilled water solution of 1 mg/ml concentration was added to cuvette and voltage changes were observed.

Although there is no external mechanical effect, it is observed that the circuit gains conductivity after the DNA solution was poured into the system. Time over voltage graph of measurement was presented in figure 5. According to the resistance value of the circuit, depending on the quantum number n in which quantized voltage values can be seen. It is seen that voltage levels of the calculated and

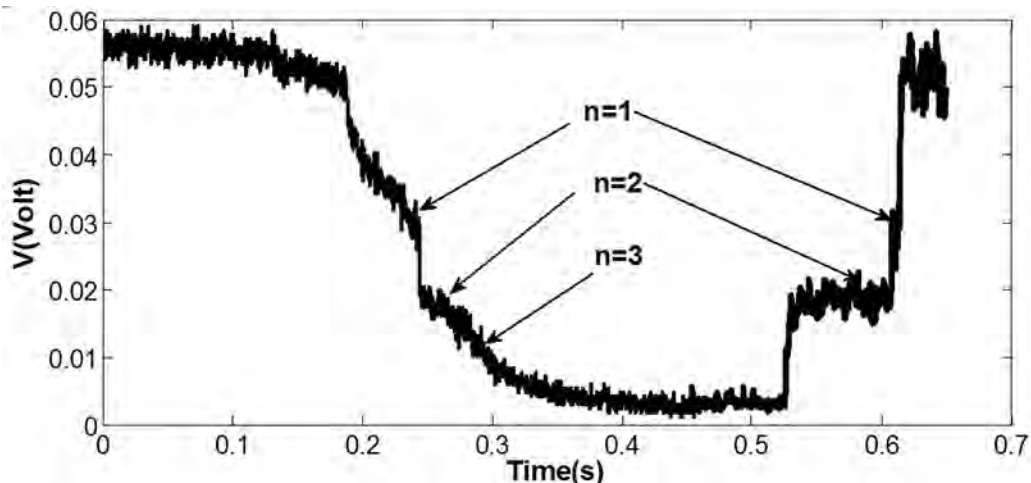


Figure 4. Measured voltage values while breaking the wire (0-0.4 s) and reconnecting the wire (after 0.4 s).

experimental levels are approximately at the same level. The experiment was repeated after solving the DNA at phosphate buffer with 7.4 pH. The pH value of phosphate buffer solution was in the range of blood pH value (7.35-7.45). Similar quantized conduction result was observed again. Pure water and phosphate buffer added to the system separately to ensure that the effect is not caused by these solvents. For these solvents no conductivity change was observed.

Our results indicate that the observed conductivity change was clearly resulting of the DNA molecules in the solutions. Since DNA is negatively charged biomolecule, we believe that when it is added in to the medium, it connects electrically the two ends of the wire and make the wire short circuit. The voltage change before the first quantized level is not discrete as can be seen from the figure 5. We can explain this part of measurement with two factors. One of them is the impurities in the solution where they act as scattering centers and effects the quantized conductance levels [13]. Another one is the conductivity of solution. Before and during the formation of nano-channels the conductivity of solution effects equivalent resistance values in the circuit so the measured potential difference.

As a next step, different kind of molecules with strand structures were tried to further investigate the results observed. Prepared albumin solution, brine solution, and acetic acid solution were measured with the setup separately. It was observed that these materials have no effect on the conductivity. The results of other ionic solutions were ensured that the obtained quantized conduction result of DNA was not originated from the ions and other structures in the solution. As a final step to investigate the DNA conductivity, the mismatched DNA solved in phosphate buffer and it is added to the testing apparatus, and also for this case no conductivity change has been observed. It is known that the mismatched or single base bulged or protein binded DNA to not show any conductivity [5]. Electron

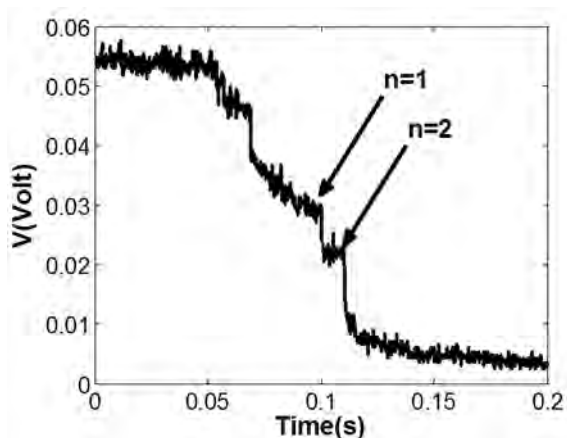


Figure 5. The potential difference change after 1 mg/mL DNA distilled water solution added into the system.

charge transport mechanism shown by these studies was in accordance with our results of DNA. So, it is detected that the quantized conductance change has been ensured by only healthy DNA solutions among the solutions presented in Table 1. Another important result was only DNA solutions were caused gold wire to switch open circuit to short circuit among the solutions tested.

Kasumov et al. observed that conductance of DNA value is in order of on the order of the resistance quantum ($h/2e^2 \approx 12.9 \text{ k}\Omega$) [14]. But following studies showed that DNA conductance values are found to be between $10-5G_0$ and $10-2G_0$ [15]. Studies of Xu et al. showed that conductance of DNA in buffer solution gives quantized conduction values during the stretching of DNA between the scanning tunneling microscopes (STM) electrodes. According to studies of Xu et al. occurrence of quantized conductance levels were due to the increase of the number of DNA molecules in the junction [9]. Conductance values of DNA in these studies were not in accordance with our results taken by our setup for DNA solution except the studies of Kasumov [14]. One of the reasons of observed high conductivity in this study can be explained by applied voltage value to the ends of wire. The applied potential difference between fractured wires ends causes to positively and negatively charged electrodes. This potential difference can cause forces on DNA and so can create nano contacts. Another reason might be the interaction between tips of broken wire and negative charges in DNA causes the DNA to act like a metallic structure. This possibility is supported by the researchers where they found that the DNA is conductive [16].

The results of this study show that the presented setup could be used for to investigate quantized conductance behavior of solutions and materials in liquid form. One of the key features of our study is the quantized conductance observation of DNA. Another one is the only healthy DNA solution causes broken gold wire to behave like short circuit. We could not observe this phenomenon with the other prepared solutions. These results clearly indicate that this system can be used for DNA sensor applications and used for to distinguish the healthy DNA.

CONCLUSION

In our study, quantized conductance was shown with a relatively simple system for the DNA solutions. Because of this DNA structures are negatively charged, we believe that DNA is making the circuit conductive by going into the junction. As a consequence of several experiments, no quantization conduction observed for pure water, phosphate solvents, albumin solution, brine solution, acetic acid solution and mismatched DNA solution. These results show that obtained quantized conduction

is specific to the DNA solutions. Our proposed system could be used for to determine healthy DNA in the solutions. Consequently, it is shown that the designed system can be used for investigation of the conductivity of the molecules in solutions.

REFERENCES

1. Sullivan TS, Geiger MS, Keller JS, Klopčič JT, Peiris FC, Schumacher BW, Spater JS, Turner PC. Innovations in nanoscience education at Kenyon College. *IEEE Transactions on Education* 51(2) (2008) 234–241.
2. Agrait N, Yeyati AL, Van Ruitenbeek JM. Quantum properties of atomic-sized conductors. *Physics Reports* 377(2) (2003) 81–279.
3. Costa-Krämer JL, García N, García-Mochales P, Serena PA, Marqués MI, Correia A. Conductance quantization in nanowires formed between micro and macroscopic metallic electrodes. *Physical Review B* 55(8) (1997) 5416.
4. Tolley R, Silvidi A, Little C, Eid KF. Conductance quantization: A laboratory experiment in a senior-level nanoscale science and technology course. *American Journal of Physics* 81(1) (2013) 14–19.
5. Muren NB, Olmon ED, Barton JK. Solution, surface, and single molecule platforms for the study of DNA-mediated charge transport. *Physical Chemistry Chemical Physics*, 14(40) (2012) 13754–13771.
6. Kelley SO, Jackson NM, Hill MG, Barton JK. Long Range Electron Transfer through DNA Films. *Angewandte Chemie International Edition* 38(7) (1999) 941–945.
7. Delaney S, Barton JK. Long-range DNA charge transport. *The Journal of organic chemistry* 68(17) (2003) 6475–6483.
8. Dekker C, Ratner M. Electronic properties of DNA. *Physics World* 14(8) (2001) 29.
9. Xu B, Zhang P, Li X, Tao N. Direct conductance measurement of single DNA molecules in aqueous solution. *Nano letters* 4(6) (2004) 1105–1108.
10. Porath D, Bezryadin A, De Vries S, Dekker C. Direct measurement of electrical transport through DNA molecules. *Nature* 403(6770) (2000) 635–638.
11. Storm AJ, Van Noort J, De Vries S, Dekker C. Insulating behavior for DNA molecules between nanoelectrodes at the 100 nm length scale. *Applied Physics Letters* 79(23) (2001) 3881–3883.
12. Qi J, Edirisinghe N, Rabbani MG, Anantram MP. Unified model for conductance through DNA with the Landauer-Büttiker formalism. *Physical Review B* 87(8) (2013) 085404.
13. Chu CS, Sorbello RS. Effect of impurities on the quantized conductance of narrow channels. *Physical Review B* 40(9) (1989) 5941.
14. Kasumov AY, Kociak M, Gueron S, Reulet B, Volkov VT, Klinov DV, Bouchiat, H. Proximity-induced superconductivity in DNA. *Science* 291(5502) (2001) 280–282.
15. Tan B, Hodak M, Lu W, Bernholc J. Charge transport in DNA nanowires connected to carbon nanotubes. *Physical Review B* 92(7) (2015) 075429.
16. Fink HW, Schönberger C. Electrical conduction through DNA molecules. *Nature* 398(6726) (1999) 407–410.

Contributions to the Knowledge of Mammals in Çorum Province, Turkey

Şafak Bulut¹, Burak Akbaba² and Ahmet Karataş³

¹Hitit University, Department of Biology, Çorum, TURKEY

²Hacettepe University, Department of Biology, Ankara, TURKEY

³Ömer Halisdemir University, Department of Biology, Niğde, TURKEY

ABSTRACT

A total of 42 mammal species were determined and new records reported for the first time in Çorum Province, Turkey. Field studies were carried between 2009-2010 and 2015-2016. One species of hedgehog and shrew, four bat species, six rodent species, roe deer and three carnivore species were recorded for the first time. We also expanded the known distribution and confirmed the presence of four rodent species (*Spermophilus xanthophyrmnus*, *Microtus dogramaci*, *Mesocricetus brandti* and *Meriones tristrami*) in the province. In addition, some information related to the distribution and the habitat associated to some taxon were provided in the study.

Article History:

Received: 2017/01/20

Accepted: 2017/03/03

Online: 2017/06/30

Correspondence to: Şafak Bulut,
Hitit University, Department of Biology,
Çorum, TURKEY
E-Mail: safakbulut@hitit.edu.tr

Keywords:

Mammal fauna; Çorum; Camera trap; Sherman trap.

INTRODUCTION

Turkey is the only country which was covered almost entirely by three of the world's 34 biodiversity hotspots: The Caucasus, Irano-Anatolian, and Mediterranean [1]. In Palaearctic Region, mammals are represented by 13 orders, 42 families and 843 species [2]. Turkey is located among Asian, European, and African continents, resulting in the diversification in ecological conditions, the geological structure, climatic conditions. This leads to a rich biodiversity. It is known that Turkey has more species in terms of the number of mammals than that of any other region in the world (North Africa: 84; Iberia: 77; Italy: 72, Balkans: 80, Near East: 62 [3], 1999, Turkey: 132 [4-6]).

Çorum located in two different geographical regions is located in between Central Anatolian and Black Sea Regions. Kızılırmak River which divides the city into two parts has an important role in the formation of Anatolia's biodiversity. Depending on these geographic features, the diversity of mammals also varies. To date, few studies on the determination of the mammal fauna have been carried out to shed light on the biodiversity in Çorum. In addition, those were local studies including small number of species. So far,

a total of 26 mammal species were reported in Çorum (Table 1).

When the studies reported in the literature on mammalian species present in Çorum is taken into account, it is seen that these works only includes small mammalian species and the data were obtained from systematic studies.

In this work, it was aimed to determine mammal fauna and important areas for mammals in Çorum. A total of 42 mammal species was identified in the field studies. Of these species, 26 had been already reported in the literature and 16 of them were observed for the first time in Çorum. In addition, new locality reports of some species were provided.

MATERIALS AND METHODS

Systematical field studies were carried out between 2009-2010 and 2015-2016 at all areas located in Çorum province, in order to determine the mammals spreading within the borders. The GPS points of all stations were recorded in UTM format and the records were taken at this coordinates and its immediate vicinity. Passive infrared camera traps

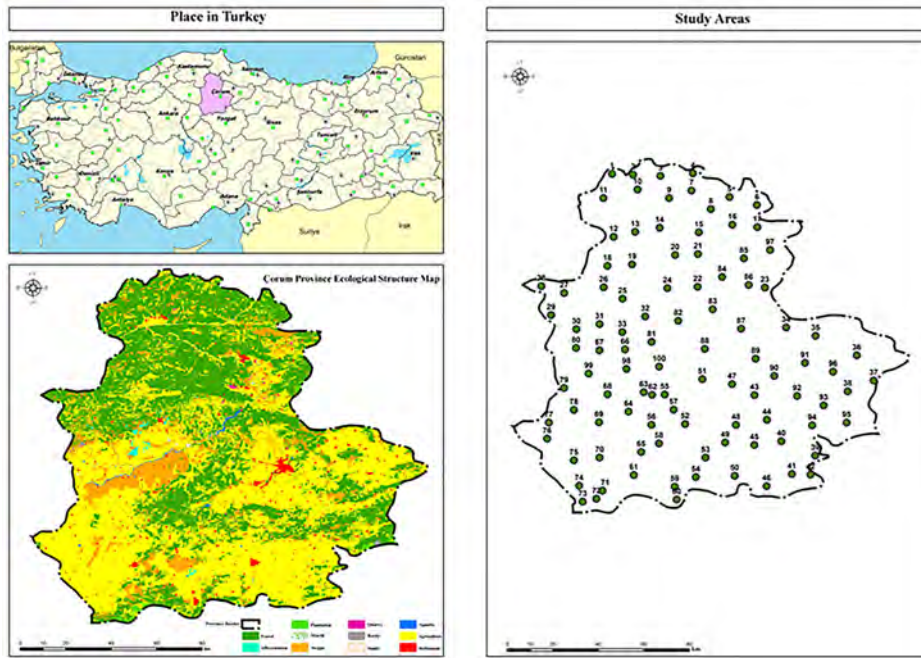


Figure 1. Map of localities listed in the text. Numbers correspond to those are given in Appendix

(Scoutguard SG570V and Bushnell Trophy Cam) were employed to determine large mammals. In addition to camera traps, large mammal fauna was also recorded using noninvasive methods such as counting scats, footprints, and other remaining.

In the detection of small mammals, Sherman live capture traps were used. The small mammalian individuals caught in the trap were released after identification of the species. Individuals who cannot be morphologically diagnosed were identified by karyotype and skull characteristics examined in laboratory conditions.

Studies to identify bat species were conducted at three different localities and ultrasonic device (Pettersson D 500X) was implemented to record the sounds. BatSound and BatExplorer computer software were used for further analysis. Species conservation status were organized according to the IUCN, BERN and CITES criteria's. The localities where the studies were conducted is shown in Figure 1.

RESULTS AND DISCUSSION

Within the scope of this study, a total number of 42 mammal species belonging to Erinaceomorpha, Soricomorpha, Chiroptera, Lagomorpha, Rodentia, Carnivora and Artiodactyla were detected. 16 of these species were recorded in Corum for the first time. The results obtained from our study along with those reported previously for Corum province is summarized in Table 1. The taxonomy of the new records present in Çorum province is provided using Wilson and Reeder [7]. Additional records are also provided for some species.

Comparison with the previously reported studies

Orhan and Beaucournu [8] recorded *Crocivora suaveolens* in Abdullah Plateau located in Kos Mountain at northern part of Corum. In addition to being present in Kos Mountain, we also found this species in floodplain forestland areas of Kos Mountain. We also observed the presence of this species in Kırkdilim, Gölün yazı Lake, Osmançık, and Kargı districts. In the same study, the authors also recorded *Apodemus sylvaticus* in the same region. On the other hand, in our study we indicated that this record was not valid. It may be suggested that this species might be *A. witherbyi* instead of *A. sylvaticus*. Orhan and Beaucournu [8] also recorded *Microtus levis* in the same area, which was confirmed by our study. Kefelioglu et al. [18] and Kyrstufek et al. [19] recorded *Microtus socialis* in Çayköy village of Mecitözü, a district of Çorum province. On the other hand, in our field study, this species was not observed in this area. Our results showed that cytotypes of *Nannospalax xanthodon* species was present in Corum regardless of the region but densely forested and rocky mountainous regions, which in an excellent agreement with the reports previously published [21,22].

Forest dormouse samples were collected from Çorum province in the studies on allozyme variations and biometrics of *Dryomys nitedula* [15,25]. On the other hand, our results did not indicate the presence of this species. In some studies conducted to the identify of age group of *Martes foina* (Beech Marten) in Turkey, the authors collected some samples in Çorum province [31,32]. We showed that this species is present in entire Çorum province.

In another study, Albayrak [33] stated that factory wastes

Table 1. Mammal species of Çorum Province (including comparisons with our study)

Family Name	Species	English Name	BERN	CITES	IUCN	Former Studies	This Study with the location numbers
ERINACEIDAE	<i>Erinaceus concolor</i>	Southern White-breasted Hedgehog	-	-	LC	-	This species is spreading throughout Turkey except Thrace. Up to date, no records were given for Çorum, but we have determined that this species spreads throughout the Çorum.
SORICIDAE	<i>Crocidura suaveolens</i>	Lesser White-toothed Shrew	Ek II	-	LC	[8]	X
SORICIDAE	<i>Crocidura leucodon</i>	Bicolored Shrew	Ek III	-	LC	-	Dead individuals were encountered at each stations of 13 and 74. Work station number 13 is an old-coniferous forest.
LEPORIDAE	<i>Lepus europaeus</i>	European Hare	-	-	LC	[9]	X
SCIURIDAE	<i>Sciurus anomalus</i>	Caucasian Squirrel	Ek II	-	LC	[10, 11]	X
SCIURIDAE	<i>Spermophilus xanthophymnus</i>	Asia Minor Ground Squirrel	-	-	NT	[12-16]	X
CRICETIDAE	<i>Mesocricetus brandti</i>	Turkish Hamster	-	-	NT	[12]	X
CRICETIDAE	<i>Arvicola amphibius</i>	Water Vole	-	-	LC	-	52 (Küçük Keşlik Village, water canal)
CRICETIDAE	<i>Microtus subterraneus</i>	European Pine Vole	-	-	LC	-	13 (Kös Mountain), 63 (Uğurludağ), 87 (Çatak Nature Park)
CRICETIDAE	<i>Microtus levis</i>	Sibling Vole	-	-	LC	[8]	X
CRICETIDAE	<i>Microtus guentheri</i>	Guenther's Vole	-	-	LC	-	All agriculture areas south part of Province
CRICETIDAE	<i>Microtus dogramacii</i>	Doğramacı's Vole	-	-	LC	[17]	X
CRICETIDAE	<i>Microtus socialis</i>	Social Vole	-	-	LC	[18, 19]	-
CRICETIDAE	<i>Meriones tristrami</i>	Tristram's Jird	-	-	LC	[20]	X
SPALACIDAE	<i>Nannospalax xanthodon</i>	Lesser Mole Rat	-	-	DD	[21, 22]	X
MURIDAE	<i>Apodemus witherbyi</i>	Steppe Field Mouse	-	-	LC	[8]	X
MURIDAE	<i>Apodemus mystacinus</i>	Broad-toothed Field Mouse	-	-	LC	-	1
MURIDAE	<i>Apodemus flavicollis</i>	Yellow-necked Mouse	-	-	LC	-	3, 10
MURIDAE	<i>Rattus rattus</i>	Brown Rat	-	-	LC	-	25, 82
MURIDAE	<i>Rattus norvegicus</i>	Black Rat	-	-	LC	[23]	X
MURIDAE	<i>Mus macedonicus</i>	Macedonian Mouse	-	-	LC	[24]	X
MURIDAE	<i>Mus domesticus</i>	House Mouse	-	-	LC	[24]	X
GLIRIDAE	<i>Dryomys nitedula</i>	Forest Dormouse	Ek III	-	LC	[15, 25]	-
RHINOLOPHIDAE	<i>Rhinolophus ferrumequinum</i>	Greater Horseshoe Bat	Ek II	-	LC	-	59 (Boğazkale, rocky place). Maximum frequency 67,1 kHz, Minimum frequency 60,6 kHz, Peak frequency 106,0 kHz, call length 9,2 ms, call distance 30 ms.
RHINOLOPHIDAE	<i>Rhinolophus hipposideros</i>	Lesser Horseshoe Bat	Ek II	-	LC	-	84
VESPERTILIONIDAE	<i>Myotis blythii</i>	Lesser Mouse-Eared Bat	Ek II	-	LC	[26]	-
VESPERTILIONIDAE	<i>Myotis myotis</i>	Greater Mouse-eared Bat	Ek II	-	LC	-	59 (Boğazkale)
VESPERTILIONIDAE	<i>Pipistrellus pipistrellus</i>	Common Pipistrelle	Ek III	-	LC	-	29 (Bayat)
VESPERTILIONIDAE	<i>Eptesicus serotinus</i>	Serotine Bat	Ek II	-	LC	[27]	-
CANIDAE	<i>Canis lupus</i>	Grey Wolf	Ek II	Ek II	LC	[28]	X
CANIDAE	<i>Canis aureus</i>	Golden Jackal	-	Ek III	LC	-	13
CANIDAE	<i>Vulpes vulpes</i>	Red Fox	-	Ek III	LC	[29]	X
URSIDAE	<i>Ursus arctos</i>	Brown Bear	Ek II	Ek II	LC	[28]	X
MUSTELIDAE	<i>Mustela nivalis</i>	Least Weasel	Ek III	-	LC	[30]	X
MUSTELIDAE	<i>Martes foina</i>	Beech Marten	Ek III	Ek III	LC	[31, 32]	X
MUSTELIDAE	<i>Meles meles</i>	Badger	Ek III	-	LC	-	12, 13, 14, 63, 38 (dead sample)
MUSTELIDAE	<i>Lutra lutra</i>	Otter	Ek II	Ek I	NT	[33]	X
FELIDAE	<i>Felis silvestris</i>	Wild Cat	Ek II	Ek II	LC	[31]	-
FELIDAE	<i>Lynx lynx</i>	Lynx	Ek III	Ek II	LC	-	12, 13, 14, 62, 63
SUIDAE	<i>Sus scrofa</i>	Wild Boar	Ek III	-	LC	[34]	X
CERVIDAE	<i>Cervus elaphus</i>	Red Deer	Ek II	Ek III	LC	[31]	X
CERVIDAE	<i>Capreolus capreolus</i>	Roe Deer,	Ek III	-	LC	-	12, 13, 14, 63

and uncontrolled hunting resulted in the extinction of *Lutra lutra* in Kuruçay in Cemilbey district. Our study supported the author statement and the population of this species was not detected in the same area. Another study conducted by our group (data not shown here) indicated the presence of this species in Kargı and Kızılırmak.

Unlike Kumerloev [31] who reported the presence of *Felis silvestris* in Osmancık Province, this species was not detected in our study. The records of *Cervus elaphus*, also presented in the same study, have been verified in our study. This species has not been found elsewhere in Corum. Kefelioglu [20] recorded *Meriones tristrami* around the district of Dodurga. In this study, the presence of this species was validated in Kirkdilim, Central District and its distribution in Corum was expanded. While Tunçdemir [12] reported the presence of *Mesocricetus brandti* in the vicinity of center of Corum, our results revealed that this species exist in the steppe areas around agricultural areas in the south and southeastern parts of Corum. As a result, the distribution of *Mesocricetus brandti* was expanded.

Albayrak et al. [10] and Aslan et al [11] used 9 individuals belong to *Sciurus anomalus* collected in Çorum in their studies. In our study, this species was observed frequently at the forested areas in the northern part of the province.

Although Beron [26] reported that *Myotis blythii* species dwell around Bogazkale and Benda et al. [27] observed bone residues of *Eptesicus serotinus* in their study on *Strix aluco* pellets around Bogazkale, any individual or voice record belong to these species were observed. According to the report on population and protection status of the large mammals in Turkey, *Canis lupus* and *Ursus arctos* exist in Corum province [28]. During camera trap study, brown bear was captured in Kargı District and wolf was recorded in almost all habitats outside the agricultural areas in Corum.

Krystufek and Vohralik [15] stated that *Spermophilus xanthopyrmnus* had a wide spread in Anatolia, including Denizli, Afyonkarahisar, Eskişehir, Ankara, Kastamonu, Çorum, Sivas, Trabzon, Bayburt, Kars, Iğdır, Ağrı, Erzurum, Malatya, Mersin, Konya, Antalya, and Van. They used samples of this species which were collected from the district of Dodurga in Corum. In addition, the authors recorded the same species in Amasya, Hamamonu, Dedekoy. As a result of this finding the authors suggested that samples were actually collected from Amasya instead of Corum. In the study on the phylogenetic relations of European and Asia minor ground squirrel, Çorum province Sungurlu district samples collected from Kavşut and Büyük İncesu villages and Alaca district have been used [16]. In our study we sampled the species from a new point in Central District additional to previous locations and expanded the distribution area of this species.

Mus macedonicus and *M. domesticus* samples for morphological studies have been collected from different parts of Turkey including Çorum by Çolak et al. [24]. In our study, these two species are frequently observed in Çorum.

In a karyological study on the tapping of *Lepus europaeus* from Turkey, researchers have studied 2 male individuals collected from Çorum province borders (Demirtas et al., 2010). In almost all of Çorum, it is possible to observe the species outside settlements.

Mustela nivalis were recorded in Kırıkkale and Çorum in biological studies [30]. In the whole of Çorum province, the species were recorded by camera traps, direct observations and questionnaire surveys.

In the study that aimed to investigate allozyme variations of *Rattus norvegicus*, researchers collected samples from Çorum province have also been used [23]. In our study, the species was sampled especially in settlements.

İbis et al. [29] also used a sample of *Vulpes vulpes* collected from the Boğazkale district of Çorum province in the study on red fox populations in Turkey. They used examples from Çorum province in his study on the phylogeny of *Sus scrofa* (Wild boar). The individuals belonging to these two species were observed in all of the areas where we conducted the field study and they were thought to be spread all around Çorum.

CONCLUSION

This was the first long term study on mammals covers whole of Çorum province. A total of 42 mammal species were detected and 16 of these species were recorded from the village for the first time. On the other hand, it was determined that presence of some species referenced by previous literature in the village were doubtful and some species have been found to distribute widespread areas than previously mentioned. Only when these outputs are taken into consideration, it is obvious that our work is an important inventory for Çorum province and will be an important baseline source for future biological studies.

In our study, we captured lynx using camera traps for the first time in Çorum province, in black pine forests of Uğurludağ and Kös Mountain Wildlife Development Area. Although it was not recorded in the Çatak Nature Park, it is thought to be using Nature Park due to the similarity of vegetation. Another large mammal species, golden jackal was also captured for the first time in province, also in Kös Mountain Wildlife Development Area.

Kızılırmak, one of the larger rivers of Turkey forms

a barrier between Kös Mountain Wildlife Development Area and Ilgaz Mountains and also rest of Blacksea Region. Therefore, for large mammal species, this area, which has very narrow transition corridors, has been identified as a highly important ecosystem area in Çorum. This region has a great ecological importance and it is highly sensitive. For this reason, we defined this area as a “protection priority area”.

For small mammal species (shrew, hedgehog and rodents), different parts of the province have important ecological characteristics in terms of habitats and vegetation types. As a result of our study, fauna of small mammal in Çorum was detailed but further species-specific studies should be done to distinguish hot spots for small mammals in Çorum.

ACKNOWLEDGEMENTS

This work has been done by DOKAY Environmental Consultancy Company by the Directorate of Nature Conservation and National Parks of the Ministry of Forestry and Water Affairs and the Provincial Directorate of Corum Nature Conservation and National Parks. We would like to thank Tuğçe Türecan and Çorum Nature Conservation and Provincial Directorate of National Parks who provided us with all kinds of data support for this study, Hayri Kömür and Mustafa Gözler for their help in the field work and their generous behavior in data sharing.

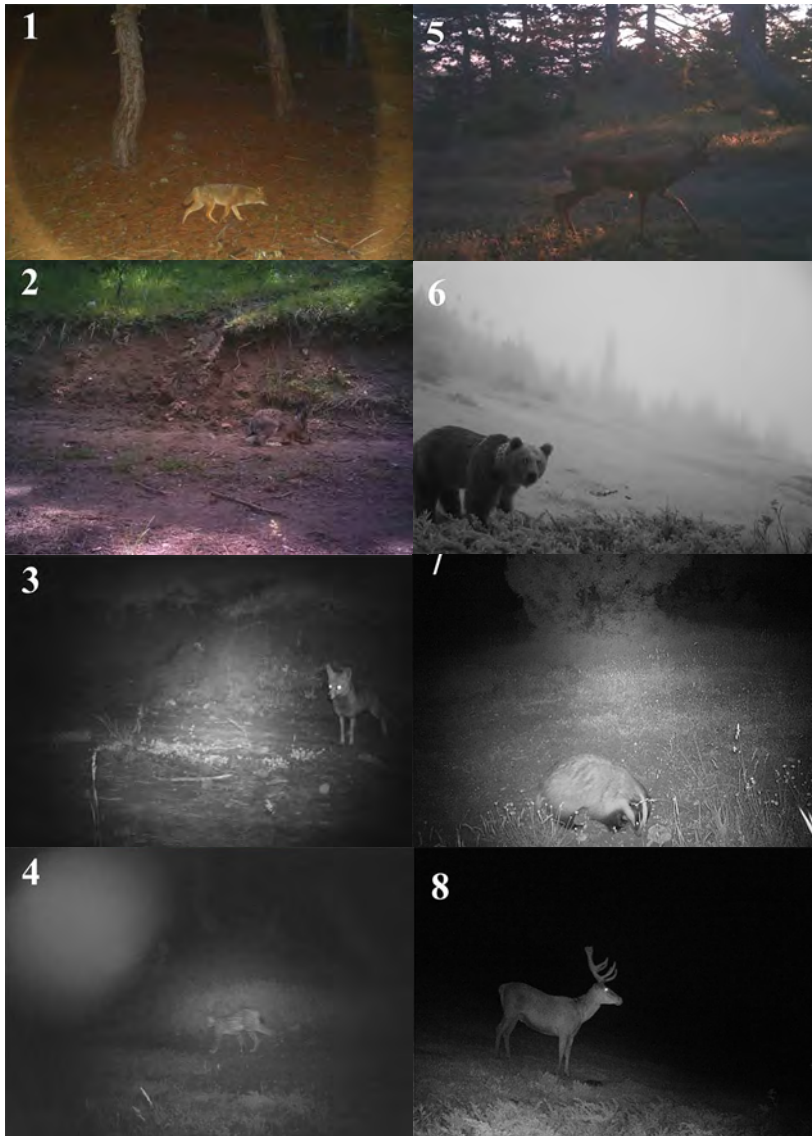


Figure 2. Some mammals records from Çorum Province. 1. Grey Wolf; 2. European Hare; 3. Red Fox; 4. Eurasian Lynx; 5. Roe Deer; 6. Brown Bear; 7. Badger; 8. Red Deer

Table 2. Station numbers and coordinates

Station Numbers	UTM Zone	N	E
1	36T	613482	4569441
2	36T	620494	4569220
3	36T	629559	4568849
4	36T	640265	4570189
5	36T	652612	4560030
6	36T	661772	4556763
7	36T	639923	4562625
8	36T	646537	4554631
9	36T	632566	4559226
10	36T	622089	4562787
11	36T	610806	4558817
12	36T	614457	4541877
13	36T	621568	4544187
14	36T	629678	4546168
15	36T	642754	4544387
16	36T	653832	4547959
17	36T	662159	4547043
18	36T	612572	4529093
19	36T	620787	4529890
20	36T	635063	4534270
21	36T	642626	4534833
22	36T	642803	4520430
23	36T	665212	4520608
24	36T	632701	4519682
25	36T	617866	4514788
26	36T	611468	4519691
27	36T	598344	4516979
28	36T	590694	4519918
29	36T	594090	4507298
30	36T	602645	4501231
31	36T	610361	4503540
32	36T	625544	4507149
33	36T	617988	4500165
34	36T	672716	4503268
35	36T	682655	4499807
36	36T	696627	4491583
37	36T	702582	4480738
38	36T	693991	4475720
39	36T	683864	4447341
40	36T	672260	4453349
41	36T	676156	4438997
42	36T	682420	4438903
43	36T	662786	4473381
44	36T	667177	4462631
45	36T	663189	4451463
46	36T	667736	4433589
47	36T	655187	4478017
48	36T	656854	4460191
49	36T	653353	4452376
50	36T	656867	4437840

Station Numbers	UTM Zone	N	E
51	36T	645157	4479962
52	36T	639749	4460229
53	36T	646896	4445641
54	36T	643801	4437012
55	36T	632693	4473042
56	36T	628458	4459705
57	36T	635749	4466416
58	36T	631099	4451545
59	36T	636733	4432704
60	36S	637522	4427093
61	36T	622905	4437558
62	36T	628429	4472806
63	36T	625646	4473880
64	36T	620613	4465359
65	36T	625199	4447686
66	36T	619043	4492597
67	36T	610497	4492048
68	36T	613491	4472835
69	36T	610826	4460461
70	36T	611209	4445008
71	36T	612396	4430509
72	36S	610402	4426921
73	36S	605815	4425632
74	36T	604504	4432547
75	36T	602569	4443680
76	36T	593464	4453099
77	36T	593944	4460147
78	36T	602291	4465819
79	36T	598848	4475368
80	36T	602656	4492966
81	36T	629657	4498965
82	36T	641260	4504988
83	36T	649308	4511242
84	36T	651892	4525767
85	36T	660055	4535449
86	36T	660593	4524855
87	36T	657594	4503438
88	36T	652167	4499524
89	36T	665179	4495095
90	36T	671181	4486018
91	36T	683178	4489223
92	36T	676121	4476921
93	36T	685408	4472838
94	36T	678687	4461595
95	36T	692472	4464297
96	36T	690315	4486519
97	36T	666875	4540934
98	36T	623221	4491262
99	36T	617430	4487100
100	36T	634545	4493222

REFERENCES

1. Mittermeier RA, Myers N, Mittermeier CG, Robles Gil P. Hotspots: Earth's biologically richest and most endangered terrestrial ecoregions, Cemex, SA, Agrupación Sierra Madre, SC, 1999.
2. Cole FR, Reeder DM, Wilson DE. A synopsis of distribution patterns and the conservation of mammal species. *Journal of Mammalogy* (1994) 75(2): 266–276.
3. Blondel J, Aronson J. *Biology and wildlife of the Mediterranean region*, Oxford University Press, USA, 1999.
4. Kence A, Kurtonur C, Özkan B, Albayrak İ, Kivanç E, Kefelioğlu H. Türkiye Omurgalılar Tür Listesi (Memeliler), Nural Matbaacılık AŞ, Ankara, 975–403-054-2, 1996.
5. Demirsoy A. *Memeliler (The mammals)*, Meteksan AS, Ankara, Turkey, 1997.
6. Yiğit N, Çolak E. Contribution to the geographic distribution of rodent species and ecological analyses of their habitats in Asiatic Turkey. *Turkish Journal of Biology* (1998) 22(4): 435–446.
7. Wilson DE, DeeAnn MR eds. *Mammal species of the world: a taxonomic and geographic reference*. JHU Press, 2005.
8. Orhan V, Beaucournu JC. Données nouvelles sur les puces de Turquie (Siphonaptera). *Bulletin de la Société Entomologique de Egyptian Society of Parasitology* (1986) 10(1): 5–18.
9. Demirbaş Y, Aşan N, Albayrak İ. Cytogenetic study on the European brown hare (*Lepus europaeus* Pallas, 1778) (Mammalia: Lagomorpha) in Turkey. *Turkish Journal of Biology* (2010) 34: 247–252.
10. Arslan A, Albayrak İ, Oshida T. Banded karyotypes of the Persian squirrel *Sciurus anomalus* from Turkey. *Caryologia* (2008) 61(2): 139–143.
11. Albayrak İ, Arslan A. Contribution to the taxonomical and biological characteristics of *Sciurus anomalus* in Turkey (Mammalia: Rodentia). *Turkish Journal of Zoology* (2006) 30: 111–116.
12. Tunçdemir Ü. 1987. Karadeniz bölgesindeki zararlı kemirici türlerinin, yayılış alanları ve zarar yaptığı bitkilerin tespiti üzerine araştırmalar. *Bitki Koruma Bülteni Ankara* (1987) 27: 65–85.
13. Osborn, DJ. Notes on the moles of Turkey. *Journal of Mammalogy* (1964) 45(1): 127–129.
14. Dogramacı S, Kefelioğlu H, Gündüz İ. Karyological analysis of the genus, *Spermophilus* (Mammalia: Rodentia) in Turkey. *Turkish Journal of Zoology* 1994 18(3): 167–170.
15. Kryštufek B, Vohralík V. *Mammals of Turkey and Cyprus. Rodentia I. Sciuridae, Dipodidae, Gliridae, Arvicolinae*. Koper, Slovenia: Knjižnica Annales Majora, 2005.
16. Gündüz İ, Jaarola M, Tez C, Yenyurt C, Polly PD, Searle, JB. Multigenic and morphometric differentiation of ground squirrels (*Spermophilus*, *Sciuridae*, *Rodentia*) in Turkey, with a description of a new species. *Molecular Phylogenetics and Evolution* (2007) 43: 916–935.
17. Yavuz Sağlam D. İç Anadolu'da yayılışı gösteren *Microtus* türlerinin morfolojik ve biyometrik özelliklerinin incelenmesi. Master Thesis, Ankara University, Ankara, 2004.
18. Kefelioğlu H. Taxonomy of *Microtus socialis* Group (*Rodentia: Microtinae*) in Turkey, with Description of a New Species. *Journal of Natural History* (1999) 33(2): 289–303.
19. Krystufek B, Kefelioğlu H. Redescription and species limits of *Microtus irani* Thomas 1921 and description of a new social vole from Turkey (Mammalia, Arvicolinae). *Bonner Zoologische Beiträge* (2001) 50(1–2): 1–14.
20. Kefelioğlu H. 1997. Taxonomic status and karyological characters of *Meriones tristrami* Thomas, 1892 (Mammalia: Rodentia) in Turkey. *Turkish Journal of Zoology* (1997) 21: 57–62.
21. Kivanç E. Türkiye Spalax'larının Coğrafik Varyasyonları (Mammalia: Rodentia). PhD Thesis, Ankara University, Ankara, 1998.
22. Sözen M, Çataklı K, Eroğlu F, Matur F, Sevindik M. Distribution of chromosomal forms of *Nannospalax nehringi* (Satunin, 1898) (*Rodentia: Spalacidae*) in Çankırı and Çorum provinces, Turkey. *Turkish Journal of Zoology* (2011) 35(3): 367–374.
23. Yiğit N, Çolak E, Özkurt SÖ, Özlük A, Çolak R, Gül N, Saygılı F, Yüce D. Allozyme variation in wild rats *Rattus norvegicus* (Berichenhout, 1769) (Mammalia: Rodentia) from Turkey. *Acta Zoologica Bulgarica* (2010) 62: 79–88.
24. Çolak E, Yiğit N, Sözen M, Çolak R, Özkurt ŞÖ, Kankılıç T, Kankılıç T. The morphological analysis of *Mus domesticus* and *Mus macedonicus* (Mammalia: Rodentia) in Turkey. *Turkish Journal of Zoology* (2006) 30: 309–317.
25. Yiğit N, Çolak E, Çolak R, Özlük A, Gül N, Çam P, Saygılı F. Biometric and Allozymic Variations in the Genus *Dryomys* (*Rodentia: Gliridae*) in Turkey. *Acta Zoologica Bulgarica* (2011) 63(1): 67–75.
26. Beron P. Données nouvelles sur les acariens parasites des mammifères en Bulgarie, en Yougoslavie, en Turquie et aux îles de Corse et de Crète. *Bulletin de l'Institut de Zoologie et Musée* (1974) 40, 59–69.
27. Benda P, Horá ek I. Bats (Mammalia: Chiroptera) of the Eastern Mediterranean. Part 1. Review of distribution and taxonomy of bats in Turkey. *Acta Societatis Zoologicae Bohemicae* (1998) 62: 255–313.
28. Can OE. Status, Conservation and Management of Large Carnivores in Turkey. Strasbourg, France: Council of Europe, 2004.
29. İbiş O, Tez C, Özcan S. Phylogenetic Status of the Turkish Red Fox (*Vulpes vulpes*), based on Partial Sequences of the Mitochondrial Cytochrome b Gene. *Vertebrate zoology*. (2014) 64 (2): 273–284.
30. Demirbaş Y, Aşan Baydemir N. The least weasel (*Mustela nivalis*) (Mammalia, Carnivora) from Central Anatolia: An overview on some biological characteristics. *Hacettepe Journal of Biology and Chemistry* (2013) 41(4): 365–370.
31. Kumerloeve H. *Die Säugetiere (Mammalia) der Türkei*. Veröffentlichungen der Zoologischen Staatssammlung München (1967) 18: 69–158.
32. Albayrak İ, Özen AS, Kitchener AC. A contribution to the age-class determination of *Martes foina* Erxleben, 1777 from Turkey (Mammalia: Carnivora). *Turkish Journal of Zoology* (2008) 32(2): 147–153.
33. Albayrak İ. Contributions To Distributon Of The Otter (*Lutra lutra* L. 1758) in Turkey (Mammalia: Carnivora). *Tabiat ve İnsan* (2000) 34(1): 3–7.
34. Demirbaş Y, Özkan Koca A, Pamukoğlu N, Sert H, Suchentrunk F. Mitochondrial DNA control region variability of wild boar *Sus scrofa* with various external phenotypes in Turkey. *Turkish Journal of Zoology* (2016) 40: 957–971.

Investigation of Poison Gland of *Sphex flavipennis* Fabrius, 1793 (Hymenoptera: Sphecidae): Morphology and Ultrastructure

Menderes Suiçmez¹, Mustafa Duran² and Kasım Özmen³

¹ Hitit University, Department of Molecular Biology and Genetics, Çorum, TURKEY

² Pamukkale University, Department of Biology, Denizli, TURKEY

³ State Hospital of Dr. Cevdet AYKAN, Tokat, TURKEY

ABSTRACT

The structure of poison gland of *Sphex flavipennis* was investigated by using, scanning electron microscopy and transmission electron microscopy. Poison apparatus consists of poison gland, poison sac, Dufour's gland and poison needle. Poison is produced in a gland consisting of two ramified glandular tubules terminating in a common sac. Each tubule is 6-8 mm in length and approximately 90 µm in diameter. These tubules are lined with the secretory cells and duct cells. The secretory cells have a well-developed secretory unit which is open to the lumen of tubules. In addition, there are free ribosomes, large secretory vesicle and a few mitochondria in the cells. Apical surface of cells are lined by irregular microvilli. Glandular tubules go into pear-like sac. Apical surface of the cells in the poison sac are lined cuticle. Outer surface of poison sac is surrounded muscle fibril and connective tissue. Lumen side of glandular tubules and poison sac are surrounded with monolayer epithelial cells.

Keywords:

Poison gland; Poison sac; *Sphex flavipennis*; Morphology; Ultrastructure.

INTRODUCTION

Poison glands are ectodermic-originated and their organization has the same model in all Hymenoptera studied [1]. A portion of the poison apparatus of *Pimpla turionellae* was placed in the abdomen, whereas another part is on the 8th, 9th and 10th ventral segments [2]. The other one of the part is placed at the end of the abdomen as a unique part and extended position. The complex-structured poison glands of *Pimpla turionellae* is composed of a sac, a toxin channel and a poison tube [3]. The needle of *Liris niger* lies down in between rectum and nervous system at the rear end of the abdomen [4]. All species investigated (*Amblyopo reclinata*, *Mystrium camillae*, *Prionopelta kraepelini*, *Onchomyrmex hedleyi*) have poison glands with two secretory tubes characterized by non-folded gland and combined with a poison sac [5]. The needle apparatus of *Pepsis pallidolimbata* consists of three anatomical structures: needle, poison gland and Dufour's gland [6]. The poison glands in *Polistes versicolor* consists of two independent tubes connected separately to poison sac [7].

Parasitic wasps lay eggs onto or inside of the hosts that make up a large part of the Hymenoptera species and the significant regulators of insect populations [8]. Poisonous bees contribute significantly to the protection of ecological balance due to the fact that they use some other insects both to breed and to be fed. Female ones among sharp-needle wasps living alone (including fossorial wasps) produce paralyzing poisons for victims (insects or spiders) they needle once or several times. The victim then taken to a prepared nest and the egg is laid down over or inside the victim. The suitable means to inject the poisons into the circulatory or neural system is an injection needle device with a modified ovipositor. Once they needle the victim, they inject poison into the haemolymph or muscle-nerve (neuromuscular) connections regions. Paralyzed victim acts as a live food source for the larvae of wasps [4]. Some pompilids sting their victims and cause temporary paralysis, then the stung spider is caught actively, consumed and normally survive until the emerging (developing) wasps will savage it [9]. The poison apparatus of Hymenoptera is directly grown from the ovipositor and makes function

Article History:

Received: 2017/01/23

Accepted: 2017/03/10

Online: 2017/06/30

Correspondence to: Menderes Suiçmez,
Hitit University, Department of
Molecular Biology and Genetics, Çorum,
TURKEY

Tel: +90 (364) 223-8000-3376

Fax: +90 (364) 223-8004

E-Mail: menderessuicmez@hitit.edu.tr,

menderessuicmez@gmail.com

as an effective defensive weapons for the colony in Aculeata [10].

Morphology and the ultrastructure of poison apparatus of many Hymenoptera have been studied [4,6,8,9,11,12,13], but there are no studies on *Sphex flavipennis*. In this study, the poison glands and poison sac were investigated using scanning and transmission electron microscopes.

MATERIALS AND METHODS

Adults of *Sphex flavipennis* Fabricus, 1793 (Hymenoptera: Sphecidae) were collected from Tokat, Pınarlı village, Turkey. The samples were killed by freezing and their poison gland was rapidly dissected from posterior of the abdomen under a binocular microscope.

Scanning Electron Microscopy (SEM)

For the scanning electron microscopic studies, the alimentary canal was fixed in 3% glutaraldehyde in phosphate buffer, pH 7.2, for 4 h at 4°C. Then samples were dehydrated in a graded acetone series (70%, 80%, 90%, 100%), critical point dried, coated with gold, and analysed under a Jeol 5400 scanning electron microscope [7].

Transmission Electron Microscopy (TEM)

For the transmission electron microscope examination, gut tissues of *S. flavipennis* were fixed in 3% glutaraldehyde in sodium phosphate buffer, pH 7.2, for 4 h at 4°C. After fixation, samples were washed with the same buffer and post-fixed in 1% osmium tetroxide and in sodium phosphate buffer, pH 7.2, for 1 h at 4°C. Tissue samples were washed with the same buffer for 2 h at 4°C, dehydrated in a graded acetone series and embedded in Araldite resin. Thin sections were stained with 2% uranyl acetate and lead citrate. The sections were viewed and photographed under a Zeiss Libra 120 transmission electron microscope [13].

RESULTS

Anatomically, the poison apparatus of *Sphex flavipennis* consists of poison glands, poison sac, Dufour's gland and poison needle. Poison glands consists of two tubular portions connected separately to poison sac. The great numbers of trachea recess along the convoluted tubes branched at the cylindrical distal ends. Each tube has a length of 6-8 mm and approximately 90 µm in diameter. (Figure 1 A). Poison sac (reservoir) are surrounded by pear-shaped externally network-like muscle fibres (Figure 1 B).

Ultrastructural observation of poison glands make one thought that the secretory and duct cells are positioned around the lumen of collecting duct. Secretory cells constitute the secretory unit with the duct cells. Secretory

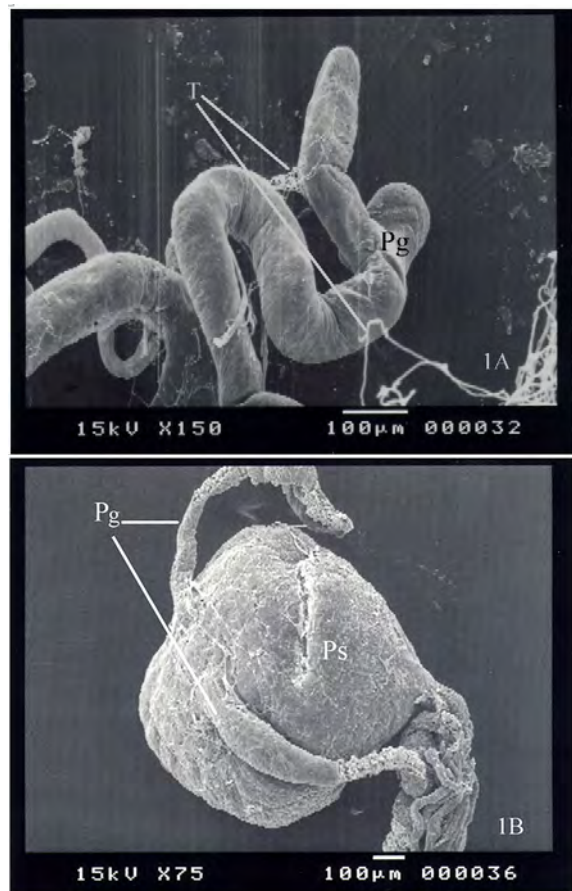


Figure 1 A. Poison Gland. Pg, Poison gland; T, Trachea. (SEM) X 150.1 B. Poison gland and Poison sac. Pg, Poison gland; Ps, Poison sac. (SEM) X 75.

unit is connected with tubulin by means of a canaliculi that is lined by a thin cuticle (Figure 2).

Each secretory unit has a large extracellular space including a great number of microvilli and each of secretory cell contains a porous outer epicuticular layer and a inner fibrous layer. A great number of microvilli is directed into the apical surface of cuticular lining of secretion apparatus. Irregularly shaped nuclei of secretory cells are relatively large and almost in central location. These cells have

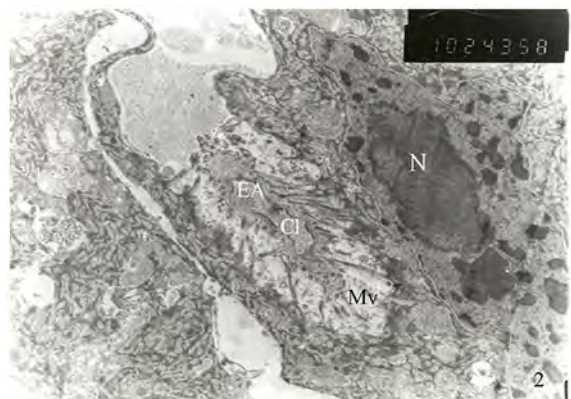


Figure 2. Secretory unit. N, Nucleus; Mv, Microvilli; EA, End apparatus; Cl, Cuticular lining. (TEM) X 10 000.



Figure 3. Secretory cell. M, Mitochondria; rer, Rough endoplasmic reticulum. (TEM) X 20 000.

numerous free ribosomes, rough endoplasmic reticulum, mitochondria, and secretory vesicles. A very dense granular endoplasmic reticulum is in the form of cisternae (Figure 3).

Secretory vesicles are observed abundantly in the peripheral cytoplasm of the cell. Some of these vesicles have light-electron density while some do intense electron-density (Figure 4 A, 4 B).

Duct cells have little amount of cytoplasm, granular endoplasmic reticulum, a few mitochondria and free ribosome (Figure 2). Poison sac is coated with by a single layer of epithelium surrounded by a thick intima layer

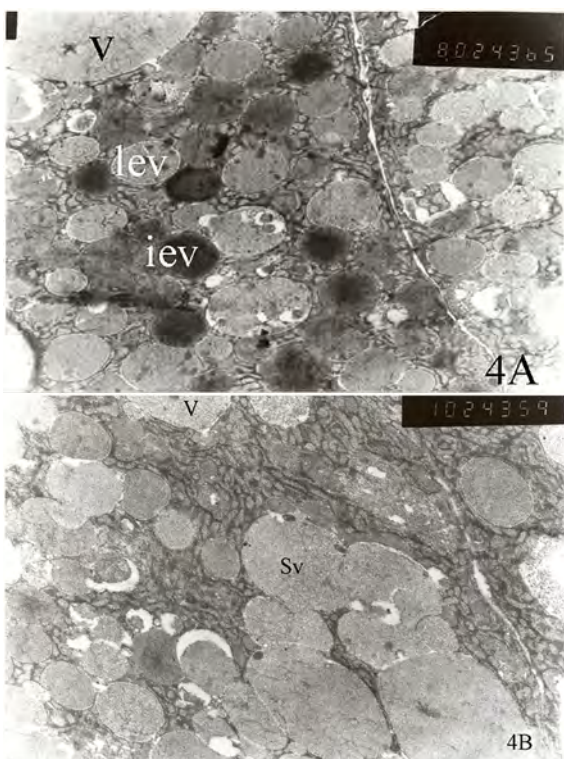


Figure 4. Peripheral cytoplasm of Secretory cell. Sv, Secretory vesicles; iev, intense electron-density vesicle; lev, light electron-density vesicle; V, Vacuole. (TEM) A X 8 000, B X 10 000.

inside. Epithelial cells are surrounded externally by the basal membrane and the muscle layer. These cells contain a relatively extended nucleus containing many mitochondria and heterogeneously dispersed chromatin (Figure 5).

DISCUSSION

Morphology

Some pompilids cause their victims have temporary paralysis, then needle-spider is caught actively, and it continues to function normally until growing wasps will consumed it [9]. The *Sphex flavipennis* that we have studied use some Orthoptera species for larval development. As defined in many studies for different species of Hymenoptera [6,8,11,12], the poison apparatus of *S. flavipennis* consists of the poison glands, poison sac, Dufour gland and poison needle.

The poison apparatus of female *Rhynchium cyanoptenum* consists of two parts as secretory part and a poison sac. The secretion part of the gland consists of two cylindrical convoluted glands, proximal end of which opens by entering separately to the poison sac while the distal end extends freely within the haemolymph [13]. The poison glands of *Sphex flavipennis* consists of two convoluted tubular parts connected separately to the poison sacs. Cylindrical tubules extends to the haemolymph freely and ramifies in distal ends.

The poison glands consist of two tree-like branched tubular glands connected to a joint bladder-like reservoir. Each of tubular glands has a length of 5-8 mm (Φ about 150 μ m). Near the reservoir entry point, branches of each tubular glands are united to form a common generating channel (Φ about 80 μ m). Poison sac is spherical when the sac is filled (Φ about 0.8 mm; volume approximately 270 nl) and is surrounded by bundles of thin network of muscle fibers [4]. Muscle fibers arranged in the form of transverse and oblique forms the sac essentially muscled in the form of four different lobes. The tubes are cylindrical and there

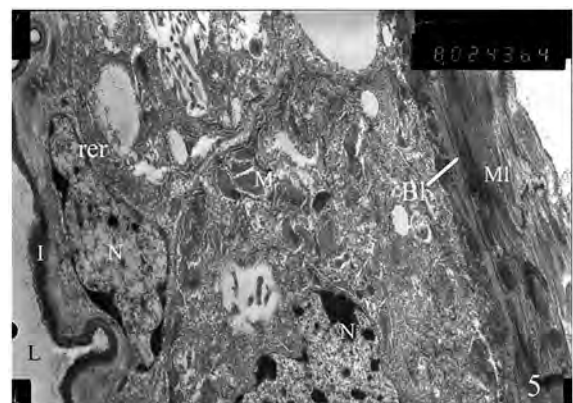


Figure 5. The cell of poison sac. N, Nucleus; M, Mitochondria; I, intima; Bl, Basal lamina; ML, Muscular layer; L, Lumen; rer, Rough endoplasmic reticulum (TEM) X 8 000.

are some slight protrusions formed on the surface due to the press of the epithelial cells [7]. The wall of poison sac in all individuals under investigation is surrounded by fairly well-developed muscle sheath [6]. The pear-shaped poison sac of *Sphex flavipennis* is surrounded outside by muscle fibres. The convoluted poison gland connected separately to poison sac have the length of 6-8 mm long and a diameter of 90 µm. The morphology and ultrastructure of poison apparatus have been studied in most of the Hymenoptera [4,5,6,8,9,11,13], but there are no studies found on this issue about *Sphex flavipennis*.

Ultrastructure

Secretion apparatus (secretory unit) tip is the terminal part containing numerous amount of microvilli and opening to secretion ducts in each of the secretory cells with large extracellular surface and epicuticular layer fibrillated inside and porous outside. In addition to microvillus, end of each apparatus is provided with secretion duct making the secretion go to the lumen [12,14]. There are some open electron density vacuoles (Φ ranges from 0.54 to 1.57 µm) available in the cytoplasm of *Pteromalus puparum* secretory cells. Secretory vesicles are often observed as scattered in peripheral cytoplasm in the cell. There are also secretory granules, a nucleus, rough endoplasmic reticulum and vacuoles available in these cells [12]. In *Sphex flavipennis*, there is a large surface with numerous amount of microvillus including epicuticular layer fibrillated inside and porous outside in secretory unit. The numerous amount of microvillus are directed towards cuticular lining on the apical surface of the secretion apparatus as defined for *Pteromalus puparum* [12] and in *Pachycondyl striata* [14]. Irregularly shaped nuclei of secretory cells are relatively large and centrally located. As noted by the researchers, these cells have granulated endoplasmic reticulum, the nucleus, secretory vesicles and secretory granules. In addition, there are a lot of rough endoplasmic reticulum and mitochondria for expression of secretory proteins in these cell types and to meet the energy required in the process of secretion and absorption, respectively. The cytoplasm of the secretory cell is characterized with abundant free ribosomes distributed to all around the cytoplasm and with a large number of spherical ergastoplasmic sac [13].

The poison sac of *Polistes versicolor* exhibits a dense muscular structure combined with thick cuticle on the reservoir wall. In reservoir, there is a well-developed epithelium continue with the outer tubular part anatomically. However, there is no secretory cell observed on the reservoir wall [7,11]. Similarly, it is observed that the sac of *Sphex flavipennis* is surrounded by dense muscle fibres, but not secretory cells on the reservoir wall. On the contrary, Abreu implies that there are secretory cell on the reservoir wall of

Apis mellifera [15]. Although it is noted that there are no specific organelles in the cytoplasm of reservoir epithelium cells of *Pteromalus puparum* [12], there are numerous amount of mitochondria observed in the epithelial cells of the sac of *Sphex flavipennis*.

CONCLUSION

In this study, we investigated morphological and ultrastructural features of poison gland of *S. flavipennis*. The features of poison gland and poison sac were found to have differences from both morphological and ultrastructural structures which help us to clarify and better understand each portion in the poison gland of this species.

REFERENCES

- Noirot C, Quennedey A: Fine structure of insect epidermal glands. *Ann. Rev. Entomol.* 19 (1974) 61-80.
- Güven T, Yel M.: *Pimpla turionellae* (Hymenoptera: Ichneumonidae)"; da zehir bezinin ince yapısı. *Doğa Türk Biyoloji Dergisi*, 14 (1) (1990) 17-3.
- Uçkan F: The Morphology of the Venom Apparatus and Histology of Venom Gland of *Pimpla turionellae* (L.) (Hym;Ichneumonidae) Females. *TR.J.Zoology* 23 (1999) 461-466.
- Gnatzy W, Volkmandt W: Venom Gland of the Digger Wasp *Liris niger*: Morphology, Ultrastructure, Age-Related Changes and Biochemical Aspects. *Cell Tissue Res.* 302 (2000) 271-284.
- Schoeters E, Ito F, Miyata H, Billen J: Abberant venom glands in *Amblyoponini* (Formicidae, Ponerinae): morphology, ultrastructure and histochemistry. *Acta Zoologica* 80 (1999) 3-9.
- Schoeters E, Schmidt JO, Billen J: Venom Gland Morphology in *Pepsis pallidolimbata pallidolimbata* and Biological Use and Activity of *Pepsis* Venom. *Canadian Journal of Zoology* 75 (1997) 1014-1019.
- Britto F B, Caetano F H: Ultramorphological analysis of the venom glands and their histochemical relationship with the convoluted glands in the primitive social paper wasp *Polistes versicolor* (Hymenoptera: Vespidae). *J. Venom. Anim. Toxins incl. Trop. Dis.* 11 (2) (2005) 160-174.
- Quicke DLJ: *Parasitic Wasps*. Chapman and Hall, London. 1997.
- Simon LH: A second record of tarantula parasitism by *Notocyphus dorsalis arizonicus* Towners (Hymenoptera: Pompilidae). *Pan-Pac. Entomol.* 65 (1989) 34-37.
- Hermann HR: Elaboration and reduction of the venom apparatus in aculeate Hymenoptera, H.R. Hermann, Editor, *Defensive Mechanisms in Social Insects*, Fraeger, New York, 1984.
- Schoeters E, Billen J: Morphology and Ultrastructure of the Convoluted Gland in the Ant *Dinoponera australis* (Hymenoptera: Formicidae). *International Journal of Insect Morphology and Embryology* 24 (1995) 323-332.

12. Zhu JY, Ye GY, Hu C: Morphology and ultrastructure of the venom apparatus in the endoparasitic wasp *Pteromalus puparum* (Hymenoptera: Pteromalidae). *Micron* 39 (2008) 926–933.
13. Bilen J, Hefetz A: Fine Structure of the Secretory Tubules of the Venom Gland in the Eumenid Wasp *Rhynchium cyanopterum*. *Israel Journal of Zoology* 48 (2002) 83–86.
14. Ortiz G, Camargo–Mathias MI: Venom gland of *Pachycondyla striata* worker ants (Hymenoptera: Ponerinae). Ultrastructural characterization. *Micron*, 42 (2006) 103–116.
15. Abreu RM: Padrões citoquímicos das glândulas de veneno de operárias de *Apis mellifera* L. (Hymenoptera, Apidae). Universidade Estadual Paulista, Instituto de Biociências, Rio Claro, 176 2000.

Permeability Characteristics of Sand Grouted with Glyoxal Blended Sodium Silicate

Eyubhan Avci

Bursa Technical University, Department Civil Engineering, Bursa, TURKEY

ABSTRACT

The goal of this study was to investigate the permeability characteristics of glyoxal blended sodium silicate injected sand specimens with different relative densities and gradations. Initially, rheological characteristics of glyoxal blended sodium silicate grouts were determined. Accordingly, the gel time decreased as the sodium silicate content increased. Viscosities of glyoxal blended sodium silicate grouts increased as the silicate content increased. Syneresis increased as the silicate content increased up to 37% but then started decreasing as the silicate content continued to increase. The groutability of glyoxal blended sodium silicate grouts into different graded sands specimens formed at various relative densities was highly successful. Grouted sand samples were kept in humidity room at a temperature of 20 °C till test time and put to permeability tests at different time intervals. In general, glyoxal blended sodium silicate grouting decreased the permeability of different graded sand specimens. The permeability of sodium silicate-glyoxal grouted sand specimens increased with time as a conclusion of syneresis.

Article History:

Received: 2017/02/06

Accepted: 2017/03/29

Online: 2017/06/30

Correspondence to: Eyubhan Avci, Bursa Technical University, Department of Civil Engineering, Bursa, TURKEY
Tel: +90 (507) 465-6336
E-Mail: eyubhanavci@gmail.com

Keywords:

Permeability; Chemical grout; Sand; Glyoxal; Sodium Silicate.

INTRODUCTION

Grouting is one of the oldest and widely used ground improvement methods in civil engineering applications all over the world. It is mainly used for reducing permeability and increasing the strength of soil or rock. It is also employed in decreasing the deformability of soil under foundations, stabilizing ground cutting face and excavations and controlling the settlement of ground surface during the opening of a tunnel [1]. Different grouting materials such as suspensions, solutions and emulsions are used for grouting purposes [2-4].

Chemical grouts were developed where the pore size in rock or soil units were too small to be penetrated by conventional Portland cement suspensions [5]. They were fluid at the beginning but reacts after a predetermined time to form a solid, semisolid or gel. Various chemical grouts have been introduced so far, and each one has characteristics suitable for different uses. The most common chemical grouts were introduced by US Army corps of engineers in five categories i.e., sodium silicate, acrylate, lignin, urethane and resin grouts [5].

Sodium silicate grouts, among them, are the most popular ones owing to their safety and environmental suitability. Therefore, the rheology of sodium silicate based grouts and the engineering properties of the grouted soils would be the field of interest. In the past, the hydraulic conductivity of sodium silicate injected sand specimens was studied by Bodocsi and Bowers, Krizek and Spino but their studies were limited to some extent [6,7].

The prime aim of this study was to find out the effect of sand gradation, relative density, and syneresis on the permeability of sodium silicate-glyoxal grouted sand thus contributing to the relevant literature.

MATERIALS AND METHODS

In this study, Quartz sand taken from Kızılırmak River next to Çorum was used. The specific gravity of sand's was specified to be 2.61 according to ASTM D854-02 [8]. Sand specimen was primarily separated into 2 various subgroups. Both of the subgroups were formed utilizing 2 sets of sieves in a manner that

Sample Preparation and Grouting

The grouting test apparatus consisted of a manometer, 100 molds for hydraulic conductivity, a grout tank with propeller and related connections. Molds were 52 mm in diameter and 120 mm in length. The test apparatus was detailed in Figure 2. The grouting test apparatus was developed by Mollamahmutoglu and Avcı [12].

The internal surfaces of the molds were slightly greased to eliminate specimens' disturbance while the samples were removed from molds after grouting. During specimen preparation, a coarse layer of sand regarding eight mm in thickness was former located at the base of the molds to evenly distribute the grout into the specimens. Specimens were then placed into molds in 3 equal layers. Each layer was compacted utilizing a vibratory hammer to accomplish the required relative density prior to the next one. For 30, 50 and 70 percent relative densities of samples, the first void ratios (e_v) were calculated from the empirical relation of relative density since the max. and min. void ratios were obtained by experiments as explained earlier. Afterwards, depending on specific gravity and void ratio of samples, the relevant dry unit weight was figured out and the essential mass of samples was calculated. From every one of these amounts, each layers' relative density was controlled.

Afterwards forming the samples at the required relative density, a coarse layer of sand about eight mm in thickness was put on the upper part of the molds. Next the base and top end-plates of the molds were assembled using tie rods (Figure 2). Lastly, specimens were filled with water. The

Table 3. Gyoxal blended Sodium Silicate solution grouts

Solution No	Water (%)	Sodium Silicate (%)	Reactant (%)
SG ₁	67	29	4
SG ₂	56	37	4
SG ₃	46	46	8
SG ₄	36	53	11

bottom and top ends were sealed against water leakage and put aside till the injection date. Before grouting, the samples were saturated by the upward flow of tap water through the bottom under the pressure of 20 kPa. Water was permitted to flow through the sand specimens ensuring that no air bubbles came out from the outlet at the upper of the mold.

The specimens' grouting pressures were performed by trial and error and the penetration pressures were determined in this direction. The injection pressures was provided with air compressor and observed by a manometer.

Before grouting, water and the pre-measured contents of reactant were blended completely in a holder by an attractive stirrer and after that sodium silicate was then included and the entire solution was mixed again. The grout was poured into grouting tank and was lastly grouted into the samples in molds. The contents of chemical substances forming sodium silicate grouts for this experimental study were presented in Table 3.

TESTING PROGRAM

Gel Time, Viscosity and Syneresis Tests

Firstly, the gel times of sodium silicate solution grouts in Table 3 were determined. They were defined as the

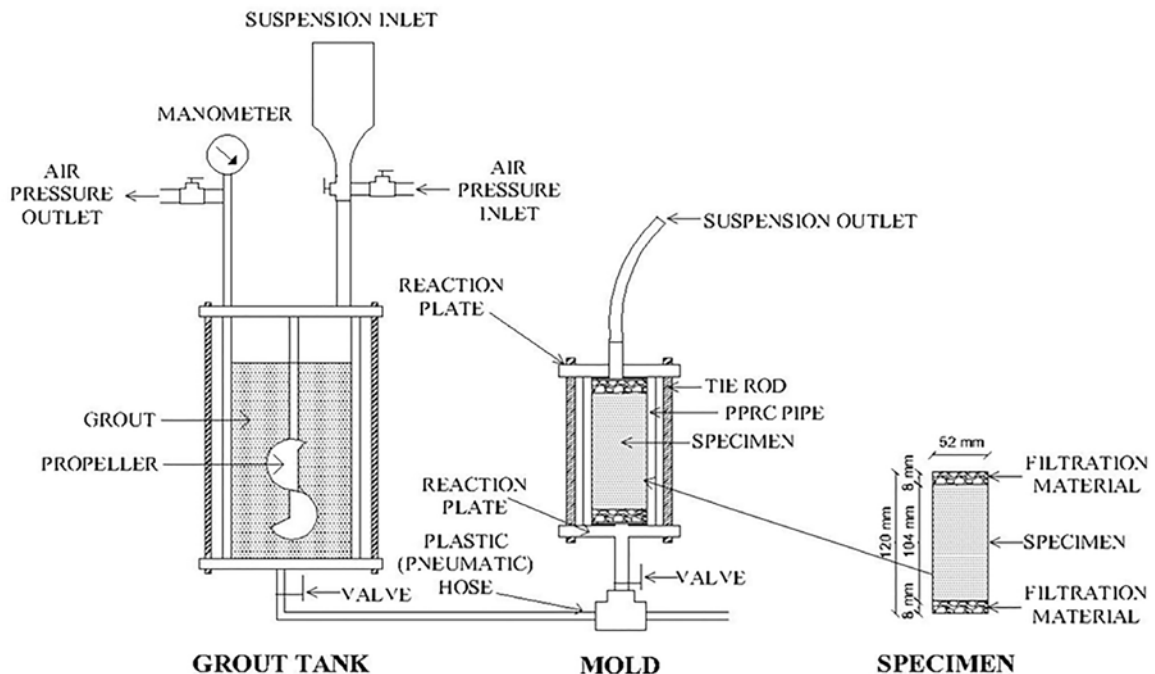


Figure 2. The details of grouting test apparatus [12].

elapsed time from grout mixing until no grout flowed out from a baker when tilted to 45° [13]. Grout gels were dependent on the components of the grout. On that account, the effect of silicate content on the gel time of grouts was studied and the findings were presented in Figure 3.

The changes of viscosities of grouts with time were quantified by Brookfield DV-III Ultra Rheometer in reference to ASTM D2196-15 [14] and the results were shown in Figure 4.

For the measurement and observation of the amount of syneresis of grout gels, the grout solutions were preserved in graduated plastic air-tight container. The syneresis and time relation was given in Figure 5. Silicate content effects on the syneresis of grouts were also presented in Figure 6.

Grout Penetration Test

The penetrability of glyoxal blended sodium silicate solutions into various graded sand specimens at 30%, 50% and 70% relative densities was investigated and the results were shown in Figure 7. The lowest grouting pressures for

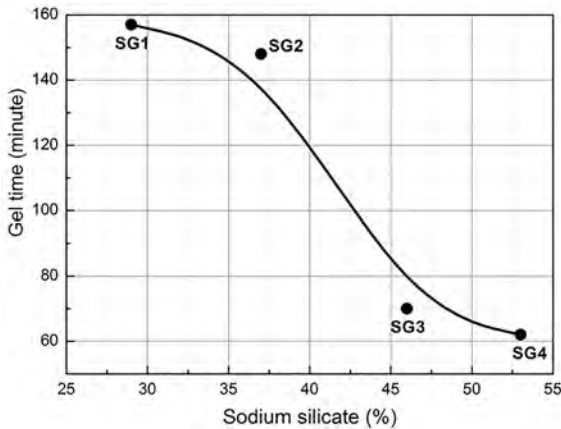


Figure 3. Gel time and Sodium silicate content relation (20°C).

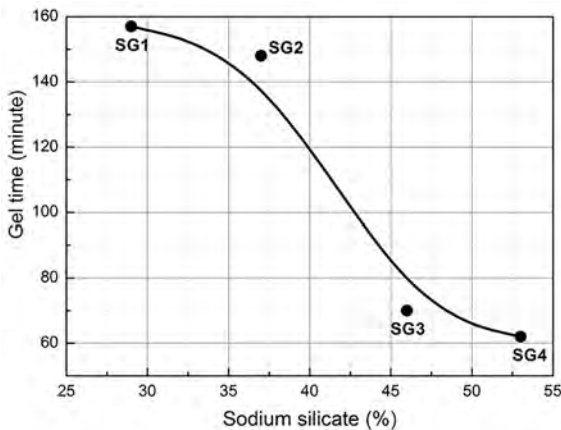


Figure 4. Sodium silicate content effect on the viscosity of grouts (20 °C).

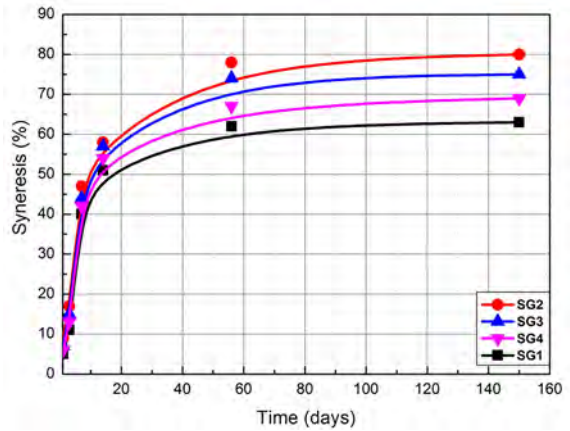


Figure 5. Syneresis of grout gels with time (20 °C).

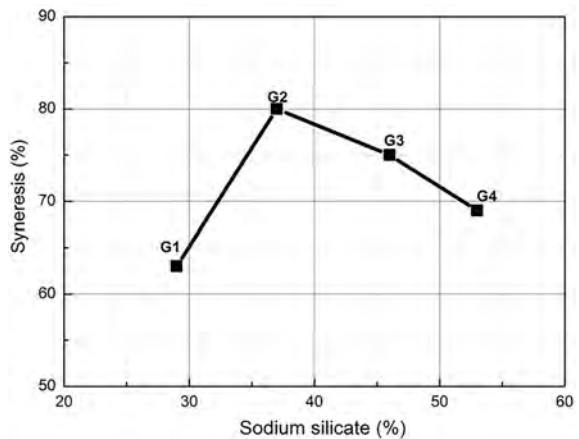


Figure 6. Sodium silicate content effect on the syneresis of grout gels for 720th day (20 °C).

the grouting of the sand specimens were also determined by trial and error and presented in Figure 7.

Permeability Tests

In the beginning, the constant head permeability tests were run on various graded ungrouted sand specimens at various relative densities in accordance with ASTM D2434-68 [15] and their permeability values were measured and given in Figure 8. In addition, the permeabilities of grouted sand specimens with different gradation and relative densities were investigated by conducting falling head permeability test under the gradient of 20 in reference to ASTM D5856-95 [16]. The influences of the curing period and fine sand content on the grouted sand specimen’s permeabilities were researched and the related results were presented in Figures 9 and 10.

RESULTS AND DISCUSSION

Gel Time Viscosity and Syneresis

The gel time of the grouts was based on the solution concentration. Figure 3 showed that increase in sodium silicate content decreased the gel time of grouts. The gel

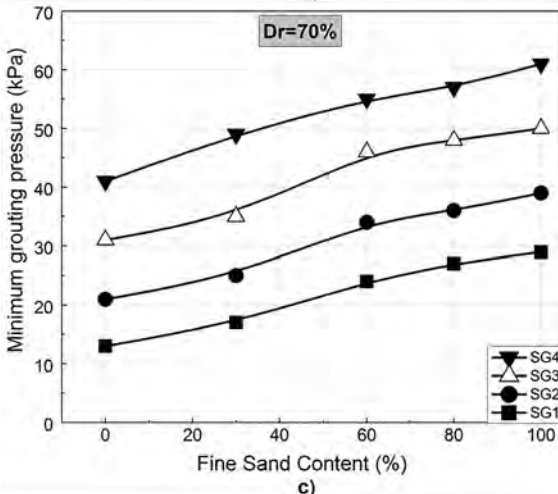
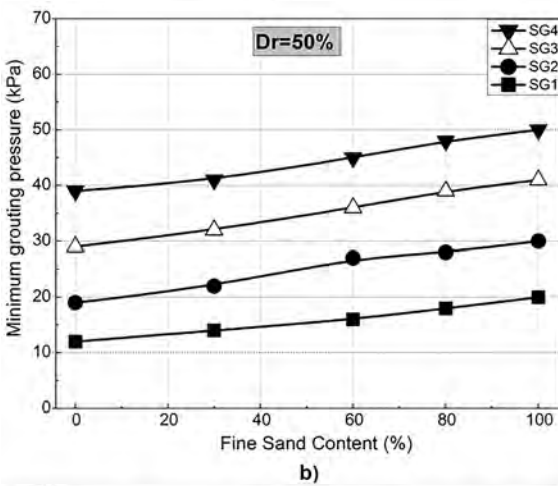
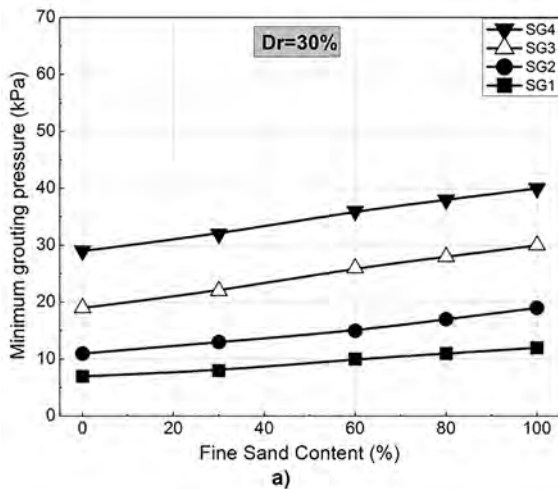


Figure 7. Grouting pressure variation with fine sand content.

time, at a room temperature of 20 °C, decreased from 157 to 62 minutes by changing the silicate content from 29 to 53 percent in return.

The outset viscosity was increased with the increase in silicate content. The outset viscosity for the grout of 29% silicate content and 4% reagent mixture was 1.95 cP and it

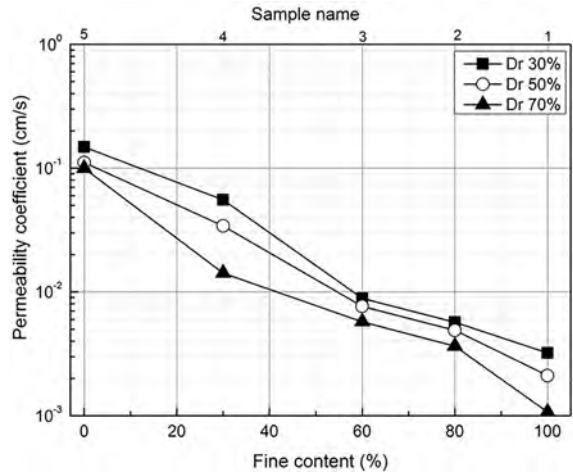


Figure 8. Permeability values of ungrouted sand samples.

was 4.89 cP for the grout of 53% silicate content and 11% mixture (Figure 4).

Syneresis is described as the leakage of liquid from the grout gel and expressed as a percentage of the initial grout volume [17]. The liquid leakage from the grout gels was sighted a period of 150 days. It considerably increased up to 56th day and continued at a decreasing rate after 56th day (Figure 5). Figure 6 showed that syneresis increased as the sodium silicate content increased up to 37% but then started decreasing as the sodium silicate content increased. The syneresis percentages of grout gels for 29%, 37%, 46% and 53% silicate contents were 63, 80, 75 and 69 respectively.

Penetrability

Sand samples compacted at 30, 50 and 70 percent relative densities were successfully grouted with all contents of sodium silicate solution. The injection pressures varied from 7 to 61 kPa (Figure 7). Increase in relative density, fine sand content and sodium silicate content increased grouting pressures.

Permeability

Sand specimens' permeabilities were decreased by two to five orders of magnitude after grouting. As the coefficient of permeabilities of ungrouted sand specimens ranged from 1.07×10^{-3} to 1.48×10^{-1} cm/s, the grouted ones varied from 3.85×10^{-6} to 1.29×10^{-5} cm/s on the 150th day after grouting (Figure 9 and 10). Bodocsi and Bowers, Krizek and Spino reported similar findings irrespective of the effects of relative density and syneresis [6,7].

Permeabilities of grouted specimens reduced with the increase of fine content of sand. The average permeability values of SG1 grouted 100% medium and 100% fine sand specimens at 30 percent relative density were 4.63×10^{-6} cm/s and 9.76×10^{-6} cm/s respectively at the end of 150th curing period (Figure 10).

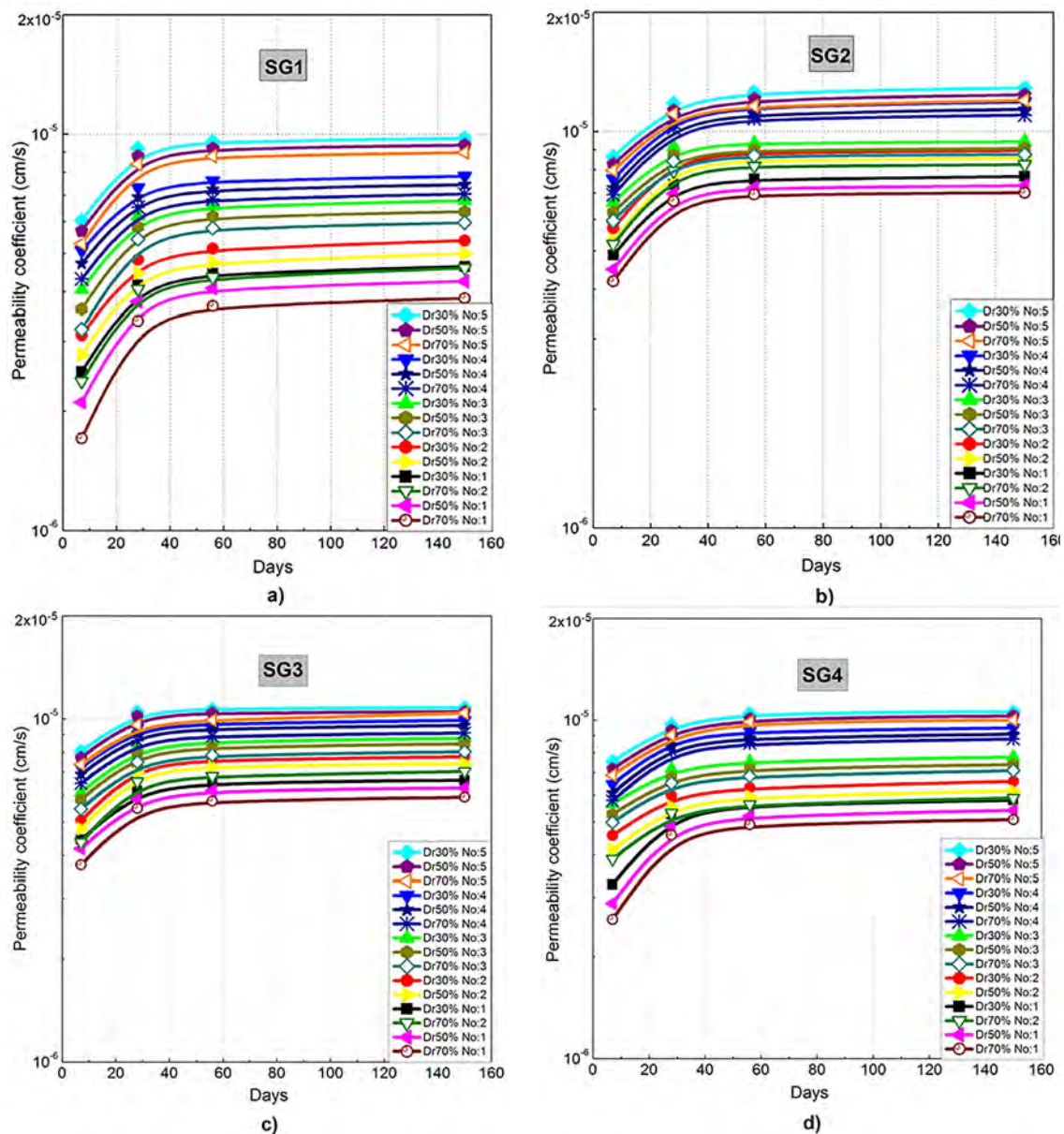


Figure 9. Permeability values of sodium silicate-glyoxal grouted sand specimens for different curing period.

Increase in relative density slightly decreased the permeabilities of grouted sand samples. The average permeabilities of SG1 grouted 100% medium sand specimens at 30%, 50% and 70% relative densities were 9.76×10^{-6} cm/s, 9.38×10^{-6} cm/s and 8.98×10^{-6} cm/s at the end of 150th day curing period respectively (Figure 10)

Up to 37 % of silicate content, permeability of injected sand specimens increased with the increase of silicate content and then decreased as the sodium silicate content increased. The permeability coefficients of grouted fine sand specimens at 30 percent relative density were 4.63×10^{-6} cm/s, 7.71×10^{-6} cm/s, 6.63×10^{-6} cm/s and 5.79×10^{-6} cm/s for 29%, 37%, 46% and 53% silicate contents by the end of 150th day respectively.

Increase in the permeabilities of injected sand samples was observed with time at a decreasing rate. The average permeability coefficients of SG1 grouted medium sand specimens at 30% relative density were 6.06×10^{-6} cm/s, 9.21×10^{-6} cm/s, 9.58×10^{-6} cm/s and 9.76×10^{-6} cm/s at the end of 7th, 28th, 56th and 150th day curing periods respectively. Increase in the permeability of sodium silicate grouted sand samples with time was due to syneresis of grout gel matrix of sand specimens.

CONCLUSION

Followings were the main conclusions drawn from this experimental study:

- The gel time of grouts were decreased with the increase in sodium silicate content.

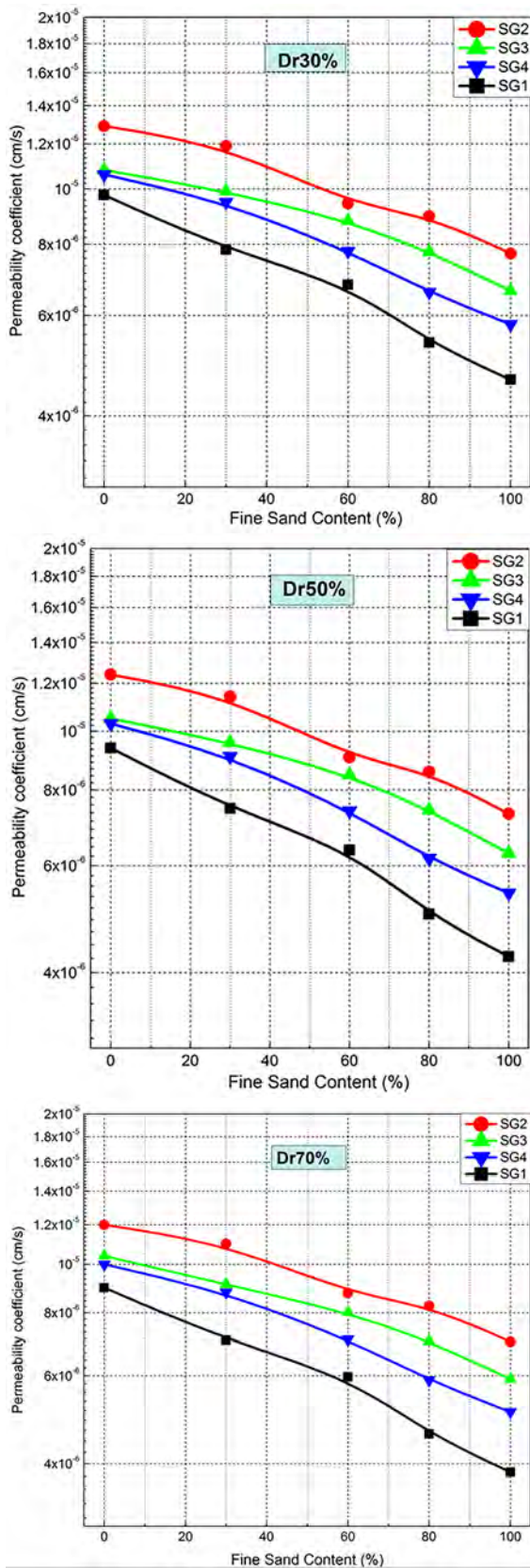


Figure 10. Variations of permeabilities of grouted sand specimens with fine sand content for 150th day.

- The onset viscosity was increased with the increase in silicate content.
- Syneresis of grouts increased as the silicate content increased up to 37% but after that started decreasing as the silicate content increased.
- Different graded sand specimens compacted at 30, 50 and 70 percent relative densities were successfully permeated with all contents of sodium silicate solutions.
- The permeability of different graded sand samples at various relative densities was reduced two to five orders of magnitude by grouting.
- Increase in fine content decreased the permeabilities of injected sand samples.
- Increase in relative density slightly decreased the permeabilities of grouted sand specimens.
- Up to 37% of silicate content, the hydraulic conductivity of injected sand samples increased. After that it decreased with the increase in silicate content.

ACKNOWLEDGEMENTS

The experiment design used in this study was created under the project number 06 / 2013-01 supported by the Scientific Research Project of Gazi University.

REFERENCES

1. Fransson A. Characterization of a fractured rock mass for a grouting filed test. *Tunneling and Underground Space Technology* 16 (2001) 331-339.
2. Cambefort H. The principles and applications of grouting. *Quarterly Journal of Engineering Geology* 10 (1977) 57-95.
3. Greenwood D.A., Thomson G.H. *Ground Stabilisation: Deep Compaction and Grouting*, Thomas Telford Publishing, UK, 1984.
4. Karol R.H. *Chemical Grouting and Soil Stabilization*, Marcel Dekker, New Brunswick, USA, 2003
5. EM 1110-3500. *Chemical Grouting*, US Army Corps of Engineers, Washington DC, 1995.
6. Bodocsi A., Bowers M.T. Permeability of Acrylate, Urethane, and Silicate Grouted Sands With Chemicals. *Journal of Geotechnical Engineering* 117 (1991) 1227-1244.
7. Krizek R., Spino M., Spatial and Directional Variations in Engineering Properties of an In Situ Silicate-Grouted Sand, in: Krizek R., Sharp K. (Eds.). *Proc., Advances in Grouting and Ground Modification Conf*, 5-8 August, Denver, Colorado, pp. 139-154, 2000.
8. ASTM D 854-02. Standard test method for specific gravity of soil solids by water pycnometer, *Annual Book of ASTM Standards*, West Conshohocken, PA, USA, 2002.
9. ASTM D 2487-11. Standard practice for classification of soils for engineering purposes (Unified Soil Classification System, *Annual Book of ASTM Standards*, West Conshohocken, PA, USA, 2011. 13
10. ASTM D 4253-00. Standard test method for maximum index density and unit weight of soils using a vibratory table,

- Annual Book of ASTM Standards, West Conshohocken, PA, USA, 2002
11. ASTM D 4254-00. Standard test method for minimum index density and unit weight of soils and calculation of relative density, Annual Book of ASTM Standards, West Conshohocken, PA, USA, 2002.
 12. Mollamahmutoglu M., Avcı E. Ultrafine Portland Cement Grouting Performance with or without Additives. *KSCE Journal of Civil Engineering* 19 (2014) 2041-2050.
 13. Gonzalez H., Vipulanandan C. Behavior of a Sodium Silicate Grouted Sand, in: Hurley T.M, Johnsen L.F. (Eds.). *Proc., Grouting and Grouting for Ground Improvement: Innovative Concepts and Applications Conf.*, 18-21 February. Denver, Colorado, pp. 1-10, 2007
 14. ASTM D 2196-15. Standard Test Methods for Rheological Properties of Non-Newtonian Materials by Rotational Viscometer, Annual Book of ASTM Standards, West Conshohocken, PA, USA, 2015.
 15. ASTM C 2434-68. Standard test method for permeability of granular soils (constant head). Annual Book of ASTM Standards, West Conshohocken, PA, USA, 2002.
 16. ASTM D 5856-95. Standard test method for measurement of hydraulic conductivity of porous material using a rigid-wall, compaction-mold permeameter. Annual Book of ASTM Standards. West Conshohocken, PA, USA, 2002.
 17. Mollamahmutoğlu M., Littlejohn G.S. A review of some of the properties of Geoseal MQ-5 and Silicate-Hardener 600B grouts. *Ground Engineering* (1995) 44-48.

Optimization of the Schiff-Base Reaction of Acetylacetone with Biogenic Amines

Bediha Akmese^{1*} and Adem Asan²

¹ Hitit University, Department of Chemistry, Corum, TURKEY

² Ondokuzmayis University, Department of Chemistry, Samsun, TURKEY

ABSTRACT

In this work, optimum conditions for the derivatization reaction of biogenic amines (histamine, tyramine, putrescine, tryptamine, phenylethylamine, cadaverine, spermidine and spermine) with acetylacetone have been determined. In this reaction, the amount of K₂HPO₄, reaction time, reagent amount, solvent choice and solvent amount were optimized. As a result of this study, optimum conditions were determined as amount of K₂HPO₄ 2 g, reaction time 20 min, amount of acetylacetone 1 mL, solvent methanol and amount of solvent 10 mL.

Article History:

Received: 2017/02/29

Accepted: 2017/04/10

Online: 2017/06/30

Correspondence to: Faruk Maraşlıoğlu,
Hitit University, Department of Chemistry,
Faculty of Arts and Science,
Corum, Turkey
Tel: +90 (364) 223-8000-3376
Fax: +90 (364) 223-8004
E-Mail: bedihaakmese@hitit.edu.tr

Keywords:

Biogenic amines; Acetylacetone; Derivatization; Schiff Base

INTRODUCTION

Amines are basic nitrogenous compounds formed by substituting alkyl or aryl groups of the one, two or three hydrogen atom in ammonia. Decarboxylation of amino acids is the most common synthesis route of foods; aromatic amines may exhibit food toxicity [1]. These amines by decarboxylation of amino acids of living organisms (bacteria) when the operating results produced are called biogenic [2]. In the presence of bacterial biogenic amine decarboxylase and suitable environmental conditions, biogenic amine formation permits bacterial growth and production of decarboxylase enzymes [3]. Biogenic amines are produced as a result of various metabolic activities of plants, animals and microorganisms. Biogenic amines containing aliphatic (putrescine, cadaverine, spermine, spermidine), aromatic (tyramine, phenylethylamine) and especially heterocyclic (histamine, tryptamine) structures are described as small molecule toxic compounds which can also be present in foods.

Biogenic amines are formed in large quantities of protein rich foods and fermented foods [4-5]. The formation of biogenic amines;

- The presence of free amino acids,
- The presence of microorganisms showing decarboxylase high enzyme activity in the medium and their number,
- Development of microorganisms
- The formation of decarboxylases depends on the presence of suitable environmental conditions such as pH and temperature [1].

It is very important to analyze and identify biogenic amines present in various foods due to their potential toxicity. Absorption intensities of the biogenic amines in the UV-Vis region are very low or not at all. Therefore, their absorption strengths need to be increased. These substances must be derivatized using an organic chelator and thus increasing the absorption intensities in the UV-Vis spectrometer becomes possible by making the resultant indirect determinations. Various derivatization reagents have been used in literature for the determination of these substances [6-22]. In this study, the use of acetylacetone reagent, previously used by Nishikawa [23] in the derivatization of primary amines, was investigated for the derivatization of

Table 1. Classification of biogenic amines

According to chemical structures	Aliphatic	Aromatic	Heterocyclic
	Putrescine Cadaverine Spermine Spermidine	Tyramine Phenylethylamine	Histamine Tryptamine
According to number of nitrogen	Monoamines	Diamines	Polyamines
	Tyramine Phenylethylamine	Histamine Putrescine Cadaverine	Spermine Spermidine

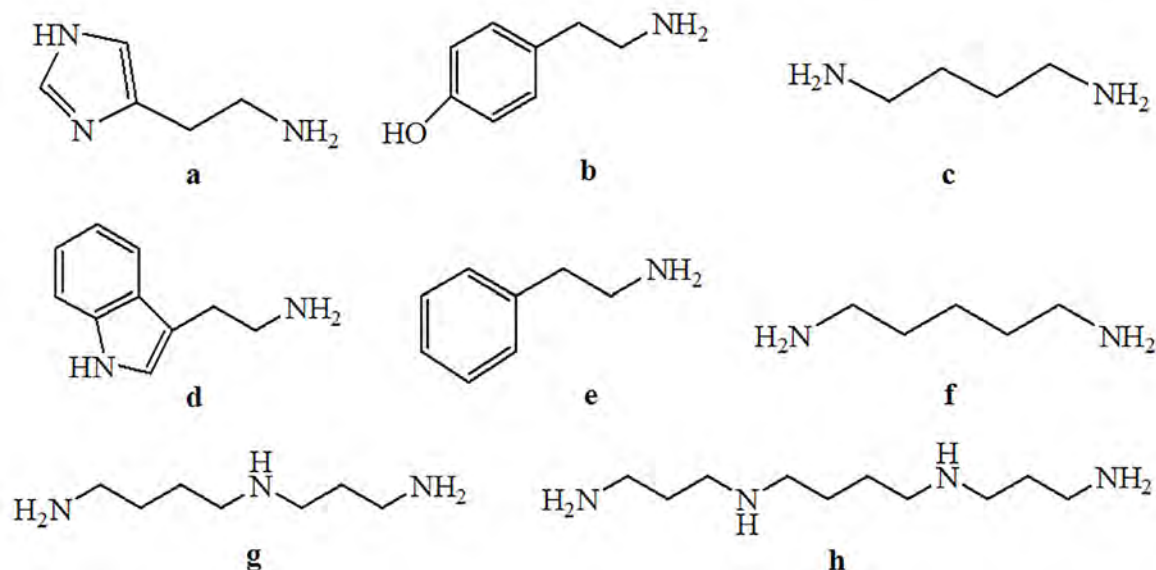


Figure 1. The chemical structure of biogenic amines (a: histamine, b: tyramine, c: putrescine, d: tryptamine, e: phenylethylamine, f: cadaverine, g: spermidine, h: spermine)

biogenic amines. The generic name for the derivatization reaction of biogenic amines with acetyl acetone is known as Schiff base formation reactions. In this study, optimum conditions for the derivatization reaction of the biogenic amines with acetylacetone have been determined.

The schiff bases can be represented by the general formula $RCH=NR'$, which is obtained from the condensation of aldehydes or ketones with primary amines and also referred to as “imine” or “azomethine” compounds due to its $C=N$ double bond as a characteristic feature in its structure [24]. R and R' is alkyl or aryl substituents. Schiff bases are also known as a good nitrogen donor ligand ($>C=N-$).



Figure 2. The formation reaction of Schiff base (R-R'-Alkyl or Aryl)

MATERIALS AND METHODS

Chemical and Reagents

Biogenic amine standards (histamine, tyramine, putrescine, tryptamine, phenylethylamine, cadaverine, spermidine, spermine), were obtained from Sigma–Aldrich. Acetylacetone was supplied by Merck. Dipotassium hydrogen phosphate (K_2HPO_4) was purchased from Merck. Acetone, acetonitrile, ethanol, methanol and tetrahydrofuran were obtained from Sigma-Aldrich (HPLC-grade).

Apparatus

The UV–Vis absorbance spectra were recorded at using a GENESYS™ 10S Thermo Scientific Perkin Elmer

spectrophotometer, equipped with a 1 cm path length cell, controlled by a personal computer. This equipment has a degasser system (WiseClean). Mettler Toledo MA 235 pH/ion analyzer with Hanna HI 1332 Ag/AgCl combined glass electrode was used for pH measurements.

Preparation of standard solutions of biogenic amines

Stock solutions of histamine, tyramine, putrescine, tryptamine, phenylethylamine, cadaverine, spermidine, spermine were prepared by dissolving each biogenic amine in 10 % (v/v) methanol/water. The diluted solutions were taken from this stock solution and diluted to the desired concentration in the same mixture. Stock solutions were kept +4 °C and stored in the dark. Water-methanol mixture was used for the further dilutions of the solutions of biogenic amines.

Derivatization Process

The final concentration of each biogenic amine solution was taken from stock solution as 1×10^{-4} M. To this, methanol, K_2HPO_4 and derivatization reagent acetylacetone were added in a certain amount and volume 100 mL completed. The mixture was allowed to stand in the dark and then their UV-Vis spectra were taken against the blank solution. Biogenic amines, the effect of all parameters of the reaction to optimize the derivatization reaction which is converted into schiff base using acetylacetone reagent were examined individually. For this purpose, parameters such as K_2HPO_4 amount, reaction time, acetylacetone amount, solvent effect and solvent amounts were investigated and optimum conditions were obtained for each.

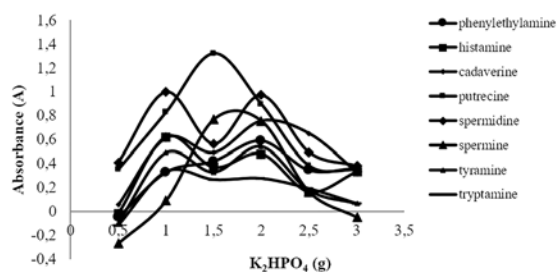


Figure 3. The effect of the amount of K_2HPO_4 on the derivatization reaction of biogenic amines with acetylacetone

RESULTS AND DISCUSSION

Effect of the Amount K_2HPO_4

The reaction of biogenic amines with acetylacetone takes place in mildly basic medium. For this purpose, K_2HPO_4 was added in different amounts and the changes in absorption were evaluated according to spectrophotometric measurement results. For this, an appropriate amount of each biogenic amine was added to a solution containing 10 mL methanol, different amounts of K_2HPO_4 (0.5; 1.0; 1.5; 2.0; 2.5 and 3.0 g) and 1 mL of acetylacetone. The mixture was then diluted to 100 mL with ultrapure water. The mixture was kept in dark for 40 min to complete the reaction. The absorption changes of different amounts of K_2HPO_4 obtained on the spectra are as shown in Figure 3.

The amount of K_2HPO_4 from which the highest absorptions were obtained was determined to be 1 g and 1 g K_2HPO_4 was used for all derivatization reaction with acetylacetone of biogenic amines throughout the study.

Effect of Time

To determine the extent to which the reaction of the derivatives of the biogenic amines with acetylacetone reactives was carried out, the solutions in which the derivatives were obtained at certain time intervals were left in the dark and the UV-Vis spectra were taken. Reaction time was optimized taking into account the absorption intensities in the spectra. An appropriate amount of each biogenic amine was added to a solution containing 10 mL methanol, 1 g K_2HPO_4 and 1 mL of acetylacetone. The mixture was then diluted to 100 mL

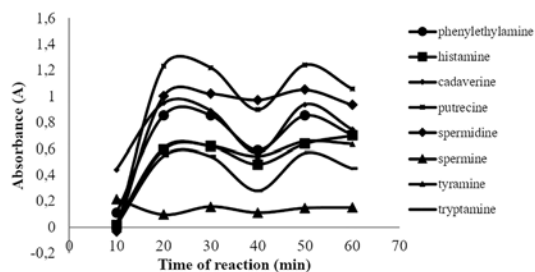


Figure 4. The effect of time on the derivatization reaction of biogenic amines with acetylacetone

with ultrapure water. Each solution was kept in the dark at 10, 20, 30, 40, 50 and 60 min intervals and UV-Vis spectrum were taken. The absorption changes obtained at different times in the spectrum are the same as in Figure 4.

The reaction time at which the highest absorptions were obtained was determined as 20 min. During the study, the solutions for the derivatization reaction of biogenic amines with acetylacetone were left in the dark for 20 min.

Effect of the Amount Acetylacetone

To optimize the amount of acetylacetone used as the reagent for the derivatization of biogenic amines, the optimum amount was determined by adding acetylacetone medium at various ratios. An appropriate amount of each biogenic amine was added to a solution containing 10 mL methanol, 1 g K_2HPO_4 and different amounts of acetylacetone (0.6; 0.8; 1.0; 1.2 and 1.4 mL). The mixture was then diluted to 100 mL with ultrapure water. The mixture was kept in dark for 20 min to complete the reaction. The absorption changes of different amounts of acetylacetone obtained on the spectra are as shown in Figure 5.

The amount of acetylacetone in which the highest absorption intensity was obtained was determined to be 1 mL and this value was used for the derivatization reaction throughout the study.

Effect of Different Solvents

The optimal solvent was determined using various solvents to reveal the solvent to be used in the derivatization reaction of the biogenic amines and the effect on the reaction. For this purpose, different solvent containing derivatization reactions were performed for each compound. An appropriate amount of each biogenic amine was added to a solution containing 10 mL solvent (methanol, ethanol, acetone, acetonitrile and tetrahydrofuran) 1 g K_2HPO_4 and 1 mL of acetylacetone. The mixture was then diluted to 100 mL with ultrapure water. The mixture was kept in dark for 20 min to complete the reaction. The absorption changes of

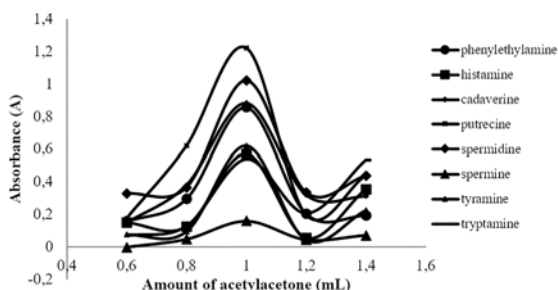


Figure 5. The effect of the amount of acetylacetone on the derivatization reaction of biogenic amines with acetylacetone

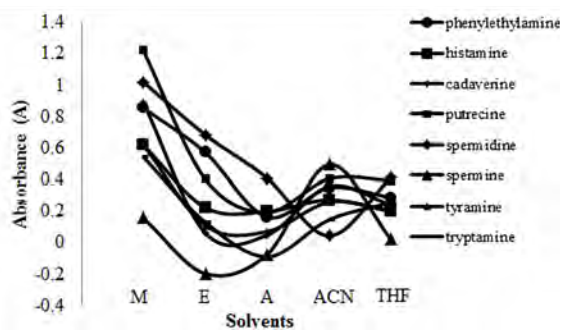


Figure 6. The effect of solvent on the derivatization reaction of biogenic amines with acetylacetone (M: methanol, E: ethanol, A: acetone, ACN: acetonitrile, THF: tetrahydrofuran)

different solvents obtained on the spectra are as shown in Figure 6.

It is seen that the solvent in which the highest absorptions are obtained is methanol. Therefore, the methanol-water mixture was used as this solvent during the derivatization of the biogenic amines with acetylacetone.

Effect of Solvent Volume

After determining that the most suitable solvent for the derivatization reaction of the biogenic amines with acetylacetone was methanol, the effect of this solvent volume on the absorption intensity was investigated. An appropriate amount of each biogenic amine was added to a solution containing different volumes of methanol (6, 8, 10, 12 and 14 mL), 1 g K_2HPO_4 and 1 mL of acetylacetone. The mixture was then diluted to 100 mL with ultrapure water. The mixture was kept in dark for 20 min to complete the reaction. The absorption changes of different volumes of methanol obtained on the spectra are as shown in Figure 7.

It is seen that the solvent in which the highest absorptions are obtained is 10 mL of methanol. For this reason, 10 mL of methanol was used during the derivatization of biogenic amines.

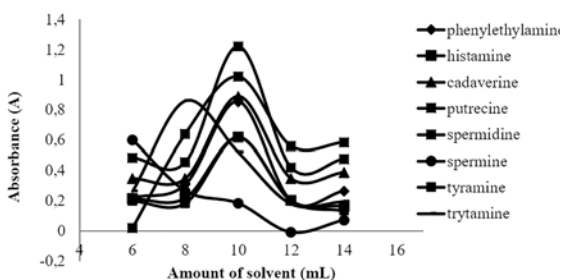


Figure 7. The effect of the volume of methanol on the derivatization reaction of biogenic amines with acetylacetone

CONCLUSION

In this study, the derivatization reaction of biogenic amines (phenylethylamine, histamine, cadaverine, putrecin, spermidine, spermine, tyramine and tryptamine) with acetylacetone reagent was optimized. The amount of K_2HPO_4 , the reaction time, the amount of acetylacetone, the solvent and the solvent amount were determined in the optimization studies. This reaction was carried out by adding 1 g of K_2HPO_4 , 10 mL of methanol, 1 mL of acetylacetone on the biogenic amine solution taken at a given concentration and diluting to 100 mL with a pure and standing for 20 minutes in the dark to complete the reaction. The end result is that the biogenic amines are converted to schiff bases.

ACKNOWLEDGEMENTS

The authors are grateful for the financial support of the scientific Research projects of Ondokuz Mayıs University (project no. PYO.FEN.1904.12.009).

REFERENCES

- Shalaby AR. Significance of biogenic amines to food safety and human health. *Food Research International* 29 (1996) 675–690.
- Preti R, Antonelli ML, Bernacchia R, Vinci G. Fast determination of biogenic amines in beverages by a core-Shell particle column. *Food Chemistry* 187 (2015) 555–562.
- ten Brink B, Damink C, Joosten HM, Huis in't Veld JH. Occurrence and formation of biologically active amines in Foods. *International Journal of Food Microbiology* 11 (1990) 73–84.
- Hernandez-Borges J, D'orazio G, Aturki Z, Fanali S. Nano-liquid chromatography analysis of dansylated biogenic amines in wines. *Journal of Chromatography A* 1147 (2007) 192–199.
- Saaïd M, Saad B, Hashim NH, Ali ASM, Saleh MI. Determination of biogenic amines in selected Malaysian food. *Food Chemistry* 113 (2009) 1356–1362.
- Anlı RE, Vural N, Yılmaz S, Vural YH. The determination of biogenic amines in Turkish red wines. *Journal of Food Composition and Analysis* 17 (2004) 53–62.
- Bauza T, Blaise A, Daumas F, Cabanis JC. Determination of biogenic amines and their precursor amino acids in wines of the Vallée du Rhône by high-performance liquid chromatography with precolumn derivatization and fluorimetric detection. *Journal of Chromatography A* 707 (1995) 373–379.
- Busto O, Miracle M, Guasch J, Borrull F. Determination of biogenic amines in wines by high-performance liquid chromatography with on-column fluorescence derivatization. *Journal of Chromatography A* 757 (1997) 311–318.

9. Casal S, Oliveira MBPP, Ferreira MA. Determination of biogenic amines in coffee by an optimized liquid chromatographic method. *Journal of Liquid Chromatography & Related Technologies* 25 (2002) 2535-2549.
10. Henriquez-Aedo K, Vega KM, Prieto-Rodríguez S, Aranda M. Evaluation of biogenic amines content in Chilean reserve varietal wines. *Food and Chemical Toxicology* 50 (2012) 2742-2750.
11. Loukou Z, Zotou A. Determination of biogenic amines as dansyl derivatives in alcoholic beverages by high-performance liquid chromatography with fluorimetric detection and characterization of the dansylated amines by liquid chromatography-atmospheric pressure chemical ionization mass spectrometry. *Journal of Chromatography A* 996 (2003) 103-113.
12. Marcobal A, Polo MC, Martín-Alvarez PJ, Moreno-Arribas MV. Biogenic amine content of red Spanish wines: comparison of a direct ELISA and an HPLC method for the determination of histamine in wines. *Food Research International* 38 (2005) 387-394.
13. Mo Dugo G, Vilasi F, La Torre GL, Pellicano TM. Reverse phase HPLC/DAD determination of biogenic amines as dansyl derivatives in experimental red wines. *Food Chemistry* 95 (2006) 672-676.
14. Papavergou EJ. Biogenic amine levels in dry fermented sausages produced and sold in Greece. *Procedia Food Science* 1(2011) 1126-1131.
15. Romero R, Sanchez-Vinas M, Gazquez D, Bagur MG. Characterization of selected Spanish Table Wine Samples according to their biogenic amine content from liquid chromatographic determination. *Journal of Agricultural and Food Chemistry* 50 (2002) 4713-4717.
16. Simat V, Dalgaard P. Use of small diameter column particles to enhance HPLC determination of histamine and other biogenic amines in seafood. *LWT - Food Science and Technology* 44 (2011) 399-406.
17. Smela D, Pechova P, Komprda T, Klejdus B, Kuban V. Liquid chromatographic determination of biogenic amines in a meat product during fermentation and long-term storage. *Czech Journal of Food Science* 21 (2003) 167-175.
18. Tameem AA, Saad B, Makahleh A, Salhin A, Saleh MI. A 4-hydroxy-N-[(E)-(2-hydroxyphenyl)methylidene] benzohydrazide-based sorbent material for the extraction HPLC determination of biogenic amines in food samples. *Talanta* 82 (2010) 1385-1391.
19. Tang T, Qian K, Shi T, Wang F, Li J, Cao Y, Hu Q. Monitoring the contents of biogenic amines in sufu by HPLC with SPE and pre-column derivatization. *Food Control* 22 (2011) 1203-1208.
20. Vidal-Carou MC, Lahoz-Portole's F, Bover-Cid S, Marine-Font A. Ion-pair high-performance liquid chromatographic determination of biogenic amines and polyamines in wine and other alcoholic beverages. *Journal of Chromatography A* 998 (2003) 235-241.
21. Yassoralipour A, Bakar J, Rahman RA, Bakar FA. Biogenic amines formation in barramundi (*Lates calcarifer*) fillets at 8 °C kept in modified atmosphere packaging with varied CO₂ concentration. *LWT - Food Science and Technology* 48 (2012) 142-146.
22. Yiğit M, Ersoy L. Determination of tyramine in cheese by LC-/UV. *Journal of Pharmaceutical and Biomedical Analysis* 31 (2003) 1223-1228.
23. Nishikawa Y. Liquid chromatographic determination of aliphatic diamines in water via derivatization with acetylacetone. *Journal of Chromatography A* 392 (1987) 349-353.
24. Sedighipour M, Kianfar AH, Mahmood WAK, Azarian MH. Epoxidation of alkenes by an oxidovanadium(IV) tetradentate Schiff base complex as an efficient catalyst with tert-butyl hydroperoxide. *Inorganica Chimica Acta* 457 (2017) 116-121.

NATIONAL & INTERNATIONAL SCIENTIFIC EVENTS

2017 International Conference on Sustainable Energy Engineering (ICSEE 2017)

Venue: The University of Western Australia
Location: Perth, Australia

BEGINS: Jun 12, 2017
Ends: Jun 14, 2017

Ecology and Safety 2017, 26th International Conference

Venue: Hotel Royal Castle
Location: Elenite, Burgas, Bulgaria

BEGINS: Jun 23, 2017
Ends: Jun 27, 2017

2017 2nd International Conference on Nanotechnology and Nanomaterials in Energy (ICNNE2017) - Ei Compendex, Scopus

Venue: INSA Lyon, France
Location: Lyon, France

BEGINS: July 07, 2017
Ends: July 09, 2017

2017 International Conference on Pure and Applied Mathematics (ICPAM2017)

Venue: TBA
Location: Prague, Czech Republic

BEGINS: July 22, 2017
Ends: July 25, 2017

ACM--2017 the First International Conference on Biometrics Science and Engineering (ICBSE 2017)-Ei Compendex, ISI and Scopus

Venue: Nanyang Executive Centre
Location: Singapore

BEGINS: Aug 04, 2017
Ends: Aug 06, 2017

2017 The 2nd International Conference on Advanced Functional Materials (ICAFM 2017)

Venue: TBA
Location: Los Angeles, United States of America

BEGINS: Aug 04, 2017
Ends: Aug 06, 2017

2017 International Conference on Robotics and Automation Sciences (ICRAS 2017)--IEEE, Ei Compendex and Scopus

Venue: TBA
Location: Hong Kong, China

BEGINS: Aug 26, 2017
Ends: Aug 29, 2017

22nd International Conference on Researches in Science & Technology (ICRST)

Venue: I. College London, S. Kensington Campus
Location: London, UK

BEGINS: Sept 13, 2017
Ends: Sept 14, 2017

8th International Conference on Legume Genetics and Genomics (ICLGG)

Venue: Hotel Azúr
Location: Siófok, Lake Balaton, Hungary

BEGINS: Sept 18, 2017
Ends: Sept 22, 2017

AVTECH '17 / V. International Automotive and Vehicle Technologies Conference

Venue: Nippon Hotel, Taksim
Location: İstanbul, Turkey

BEGINS: Oct 06, 2017
Ends: Oct 07, 2017

CHEMTECH '17 / V. International Chemical Engineering and Technologies Conference

Venue: Nippon Hotel, Taksim
Location: İstanbul, Turkey

BEGINS: Oct 06, 2017
Ends: Oct 07, 2017

2017 the 7th International Conference on Power and Energy Systems (ICPES 2017)

Venue: TBA
Location: Toronto, Canada

BEGINS: Nov 01, 2017
Ends: Nov 03, 2017



Abstracted & Indexed in:

TR Dizin | Mühendislik ve Temel Bilimler Veri Tabanı | CrossRef | Google Scholar | MIP Database | StuartxChange | ResearchBib | Scientific Indexing Services (SIS)

HITTITE